



**Self-excited Induction Generator**  
**– A Study Based on Nonlinear Dynamic Methods**

Dandan Ma

A thesis submitted for the degree of  
Doctor of Philosophy

May, 2012

School of Electrical and Electronic Engineering

Newcastle University

United Kingdom

# ABSTRACT

An induction generator offers advantages in terms of its low cost, simplicity, robust construction, nature protection against short circuits and ease of maintenance in today's renewable energy industry. However, the need for an external supply of reactive power (to produce a rotating magnetic flux wave) limits the application of an induction machine as a standalone generator. It is possible for an induction machine to operate as a Self-excited Induction Generator (SEIG) if capacitors are connected to the stator terminals in order to supply the necessary reactive power to achieve generating electrical energy in remote areas.

Poor voltage and frequency regulation is the main drawback of a SEIG as the system is highly dynamic under variable load conditions. The regulation of speed and voltage does not result in a satisfactory level although many studies have been focused on this topic in the past. Therefore, the aim of the thesis is to provide a better understanding of the behaviour of a smooth airgap, self-excited, squirrel cage induction generator as a nonlinear dynamic system when operating under a variety of load conditions, which would hopefully contribute to the development of a better regulated/controlled, viable SEIG system.

Allowing for the cross-saturation nonlinear effect, a mathematical Simulink,  $d-q$  axis model of the SEIG system utilising currents as state space variables is developed and verified by both the experimental results and numerical analysis. The SEIG computer model is constructed and tested using Matlab/Simulink R2010b throughout the thesis.

The self-autonomous system is shown to exhibit a transition from a stable periodic orbit to a quasi-periodic orbit (leading to likely chaotic motion) through a Neimark bifurcation, as a result of small changes in the values of system parameters (such as load resistance, load inductance, rotational speed and self-excitation capacitance). This characteristic dynamic behaviour of the SEIG

system is firstly identified in this work and is verified experimentally using a 1.1 *kW* laboratory test rig.

The stability of the periodic and quasi-periodic orbits exhibited by the SEIG system when feeding an inductive load (*RL*) is numerically analysed and the movement of the eigenvalues of the system's characteristic matrix when changing a system parameter is presented to verify the qualitative change in system behaviour from a stable period-one orbit to unstable quasi-periodicity. Eigenvalue technique is successfully applied to assess the stability of the period-one and quasi-periodic orbits of the SEIG when feeding variable load conditions.

This thesis is dedicated to  
my son Jethro Ziyao Van Suddese, my husband Samuel Van Suddese  
and  
my parents Fengqin Jiang and Xiaodi Ma.

# ACKNOWLEDGEMENTS

I would like to express my gratitude to my main supervisor Dr. Bashar Zahawi for his valuable guidance and endless support throughout the project. I especially appreciate his great help on the scholarship, financial support, experimental testing, thesis correction and for pointing me in the right direction during my work on the project. He was always available for help, advice and support despite his busy working schedule. I would like to thank my secondary supervisor Dr. Damian Giaouris for giving me the opportunity to pursue my dream of being a Doctor in Electrical Engineering and his great help on nonlinear dynamic analysis of the SEIG system. I am also grateful to Professor Sumitro Banarjee for his interest and help on the nonlinear dynamics part of the project. Last but not least, I would like to thank Dr. Volker Pickert for his help on the project.

I would like to thank the technical support staff in the Electronics and Mechanical workshop at the School for their help on building the safe bench testing equipment, special thanks to Stephen Mitchell and Jack Noble. I also would like to thank the administrative and computing support staff at the school. Special thanks to Gillian Webber and Ian Pitcher for their continuous support during the project period. Thanks are also given to the School of Electrical and Electronic Engineering at Newcastle University for granting me the scholarship which aided me to complete the whole project.

This thesis could not have been written without my family who gave me their sacrifice, patience and moral support during the period of the project, particularly, my husband, my son, my parents, my sister, my brother-in-law and their children. Special thanks to my parents for their continuous financial support and my husband for his selfless dedication throughout the study.

I am also grateful to a number of my friends and colleagues who participated directly or indirectly to the success of the project. They are: Dr. Shady Gadoue, Dr. Huifeng Chen, Dr. Georges El Murr, Dr. Kamyar Mehran, Dr. Mahera Musallam, Gavin Greene, Gavin Montgomery and Yijun Shen.

# TABLE OF CONTENTS

<b>CHAPTER 1</b>	<b>1</b>
<b>INTRODUCTION</b>	<b>1</b>
1.1 General Introduction	1
1.2 Contribution of the Thesis	2
1.3 Scope of the Thesis	3
1.4 Publication	4
<b>CHAPTER 2</b>	<b>5</b>
<b>THE SEIG SYSTEM REVIEW</b>	<b>5</b>
2.1 SEIG System Configuration	6
2.2 Overview of the Self-excited Induction Generators	7
2.2.1 Overview of the Development of the SEIG	7
2.2.2 The Self-excitation Phenomenon	11
2.2.3 SEIG System Performance	12
2.2.4 Operational Problems of the SEIG System	13
2.3 Modelling of the SEIG as a Nonlinear System	15
2.3.1 Nonlinear Induction Generator Modelling Based on the Cross-saturation Effect	15
2.3.2 Nonlinear Induction Generator Modelling Based on the Saturation of Leakage Inductance Effect	16
2.3.3 Nonlinear Induction Generator Modelling Based on the H-G Diagram	17
2.3.4 Nonlinear Induction Generator Modelling Based on the Skin Effect	18
2.4 Summary	19
<b>CHAPTER 3</b>	<b>20</b>
<b>NONLINEAR DYNAMIC SYSTEMS</b>	<b>20</b>

3.1 Nonlinear Dynamic Systems	20
3.1.1 Differential Equations	21
3.1.2 Difference Equations	21
3.2 Poincaré Maps	22
3.3 Limit Sets	24
3.3.1 Fixed Points	24
3.3.2 Periodic Solutions	24
3.3.3 Quasi-periodic Solutions	24
3.3.4 Chaotic Behaviour	25
3.4 Stability of Limit Sets	26
3.4.1 Stability of a Fixed Point	27
3.4.2 Stability of a Periodic Solution	28
3.4.3 Stability of a Quasi-periodic Solution	29
3.5 Bifurcation Diagrams	30
3.5.1 Smooth Bifurcations	30
3.5.2 Non-smooth Bifurcations	32
3.6 Summary	33
<b>CHAPTER 4</b>	<b>34</b>
<b>MATHEMATICAL MODELLING OF THE SEIG</b>	<b>34</b>
4.1 Standard Induction Machine Model Ignoring the Cross-saturation Effect	36
4.1.1 The 3-Phase AC Supply Block	37
4.1.2 The 3-Phase to d-q or d-q to 3-Phase Transformation Block	37
4.1.3 The Main Induction Machine Block	38
4.1.4 The Mechanical Dynamics System Block	41
4.2 Induction Machine Model Including the Cross-saturation Effect	42
4.2.1 Mathematical Representation of Cross-saturation	42

4.2.2	Torque Equations	45
4.3	Self-Excited Induction Generator Model	46
4.3.1	The Mathematical Descriptions	46
4.3.2	Simulation Results	50
4.4	Summary	54
	<b>CHAPTER 5</b>	<b>55</b>
	<b>EXPERIMENTAL INVESTIGATION</b>	<b>55</b>
5.1	Test Setup	56
5.1.1	System Overview	56
5.2	Magnetising Curve Test	58
5.3	SEIG No-load Tests	61
5.3.1	Test 1; $C = 45 \mu\text{F}$	61
5.3.2	Test 2; $C = 60 \mu\text{F}$	63
5.3.3	Test 3; $C = 90 \mu\text{F}$	64
5.4	SEIG Purely Resistive Load Tests	66
5.4.1	Test 4; $R = 60 \Omega$ ; $C = 45 \mu\text{F}$	66
5.4.2	Test 5; $R = 50 \Omega$ ; $C = 45 \mu\text{F}$	68
5.4.3	Test 6; $R = 40 \Omega$ ; $C = 45 \mu\text{F}$	70
5.4.4	Phase Plane and Harmonic Examination of the Period-one Linear Orbit	72
5.5	SEIG Inductive Load Tests	75
5.5.1	Test 7; $R = 90 \Omega$ ; $L = 1.7 \text{ mH}$ ; $C = 45 \mu\text{F}$ (Base Case)	75
5.5.2	Test 8; $R = 60 \Omega$ ; $L = 60 \text{ mH}$ ; $C = 45 \mu\text{F}$	77
5.5.3	Test 9; $R = 40 \Omega$ ; $L = 11 \text{ mH}$ ; $C = 45 \mu\text{F}$	79
5.5.4	Phase Plane and Harmonic Examination of the Nonlinear Orbit	81
5.6	Chaotic waveforms	84
5.7	Summary	87

<b>CHAPTER 6</b>	<b>88</b>
<b>NUMERICAL ANALYSIS OF THE SEIG NONLINEAR BEHAVIOUR</b>	<b>88</b>
6.1 Base Case – Period-One Orbit	89
6.2 SEIG Nonlinear Behaviour	90
6.2.1 Changing the Self-Excitation Capacitance C	90
6.2.2 Changing the Load Resistance R	96
6.2.3 Changing the Rotor Speed $\omega_r$	98
6.3 Stability Analysis	101
6.3.1 Analysis of the Period-One Orbit	102
6.3.2 Analysis of the Quasi-period Orbit	106
6.3.3 An Overview of the Movement of Eigenvalues when Changing a Control Parameter	109
6.4 Summary	112
<b>CHAPTER 7</b>	<b>113</b>
<b>CONCLUSIONS AND FUTURE WORK</b>	<b>113</b>
7.1 Conclusions	113
7.2 Future Work	116
<b>APPENDICES</b>	<b>117</b>
Appendix A	117
The Sub-blocks of the Standard Induction Machine Model	117
Appendix B	121
Modelling of Leakage Saturation Effects	121
Appendix C	128
The Electrical Equivalent Circuit Tests of the Induction Machine	128
Appendix D	133
Test Equipment	133
Appendix E	136

More Sampled State Variables and Jacobian Matrices

136

**REFERENCES**

**144**

# LIST OF FIGURES, TABLES AND ABBREVIATIONS

## FIGURES

Figure 2.1 Schematic diagram of a standalone self-excited induction generator. .....	6
Figure 3.1 Poincaré map of a periodic autonomous system. ....	22
Figure 3.2 Poincaré map of a periodic autonomous system with perturbation. ..	23
Figure 3.3 The limit set of the Poincaré map in the case of a degree 2 quasi- periodic orbit is an embedded circle. ....	25
Figure 3.4 The limit set of the Poincaré map for a chaotic system [69]. ....	25
Figure 3.5 Two perturbed trajectories; stable case (top) and unstable case (bottom). ....	28
Figure 3.6 Phase plane diagrams for a degree 2 quasi-periodic system; the fixed point at (0,0) is stable (left), the fixed point at (0,0) is unstable (right) [67]. ....	29
Figure 3.7 A typical characteristics of a pitchfork bifurcation, $r$ is the bifurcation parameter and $x$ is the system output. ....	30
Figure 3.8 A typical characteristics of a saddle-node bifurcation, $r$ is the bifurcation parameter and $x$ is the system output. ....	31
Figure 3.9 A period doubling bifurcation [71] .....	31
Figure 3.10 A Neimark bifurcation, $\mu$ is bifurcation parameter and $x$ is the system output [67]. ....	32
Figure 4.1 The standard induction machine Simulink model overview with multiple inputs and outputs. ....	36
Figure 4.2 Saturated magnetising inductance $L_m$ and dynamic inductance $L$ [11]. .....	43
Figure 4.3 The SEIG $d-q$ equivalent circuit. ....	46

Figure 4.4 Stator direct axis equivalent circuit with self-excitation capacitors without load; $i_{sD}$ is the stator direct current. ....	47
Figure 4.5 Stator direct axis equivalent circuit with self-excitation capacitors and resistive load $R$ ; $i_{sD}$ , $i_{cD}$ and $i_{Ld}$ are the stator, capacitor and load direct currents, respectively. ....	48
Figure 4.6 Stator direct axis equivalent circuit with self-excitation capacitors and inductive load ( $RL$ ); $i_{sD}$ , $i_{cD}$ and $i_{Ld}$ are the stator, capacitor and load direct currents, respectively. ....	49
Figure 4.7 Stator direct axis equivalent circuit with various load types. ....	50
Figure 4.8 Stator line-to-line voltage builds up at no-load. ....	51
Figure 4.9 Magnetising current during initial self-excitation at no-load. ....	52
Figure 4.10 Computed stator line-to-line voltage (top) and load current (bottom) when applying a $27 \Omega$ load at 1 s. ....	52
Figure 4.11 Magnetising current when applying a $27 \Omega$ load at 1 s. ....	53
Figure 5.1 Outline of the SEIG test rig. ....	56
Figure 5.2 The 1.1 kW IM magnetising characteristics. ....	58
Figure 5.3 Magnetising inductance versus magnetising current. ....	59
Figure 5.4 $ i_m dL_m/d i_m $ versus magnetising current. ....	59
Figure 5.5 Dynamic inductance versus magnetising current. ....	60
Figure 5.6 Test 1 – Measured stator line current waveforms at no-load with $C = 45 \mu F$ per phase – Period-one waveforms. ....	62
Figure 5.7 Test 1 – Simulated stator line current waveforms at no-load with $C = 45 \mu F$ per phase – Period-one waveforms. ....	62
Figure 5.8 Test 2 – Measured stator line current waveforms at no-load with $C = 60 \mu F$ per phase – Period-one waveforms. ....	63
Figure 5.9 Test 2 – Simulated stator line current waveforms at no-load with $C = 60 \mu F$ per phase – Period-one waveforms. ....	63

Figure 5.10 Test 3 – Measured stator line current waveforms at no-load with $C = 90 \mu F$ per phase – Period-one waveforms.....	65
Figure 5.11 Test 3 – Simulated stator line current waveforms at no-load with $C = 90 \mu F$ per phase – Period-one waveforms.....	65
Figure 5.12 Test 4 – Measured stator line current waveforms with $R = 60 \Omega$ and $C = 45 \mu F$ per phase – Period-one waveforms.....	67
Figure 5.13 Test 4 – Simulated stator line current waveforms with $R = 60 \Omega$ and $C = 45 \mu F$ per phase – Period-one waveforms.....	67
Figure 5.14 Test 5 – Measured stator line current waveforms with $R = 50 \Omega$ and $C = 45 \mu F$ per phase – Period-one waveforms.....	69
Figure 5.15 Test 5 – Simulated stator line current waveforms with $R = 50 \Omega$ and $C = 45 \mu F$ per phase – Period-one waveforms.....	69
Figure 5.16 Test 6 – Measured stator line current waveforms with $R = 40 \Omega$ and $C = 45 \mu F$ per phase – Period-one waveforms.....	71
Figure 5.17 Test 6 – Simulated stator line current waveforms with $R = 40 \Omega$ and $C = 45 \mu F$ per phase – Period-one waveforms.....	71
Figure 5.18 Stator line current $i_c$ versus $i_b$ phase plane diagram – Period-one. .....	73
Figure 5.19 Sampled states of stator line current $i_{cn}$ versus $i_{bn}$ Poincaré section – Period-one.....	73
Figure 5.20 SEIG current FFT with resistive load ( $R = 50 \Omega$ ); The frequency and amplitude of the dominating signal are approximately $60 Hz$ and $5.1 A$ .....	74
Figure 5.21 Test 7 – Measured stator line current waveform with $R = 90 \Omega$ , $L = 1.7 mH$ and $C = 45 \mu F$ per phase – Period-one waveform.....	76
Figure 5.22 Test 7 – Simulated stator line current waveforms with $R = 90 \Omega$ , $L = 1.7 mH$ and $C = 45 \mu F$ per phase – Period-one waveform.....	76
Figure 5.23 Test 8 – Measured stator line current waveform with $R = 60 \Omega$ , $L = 60 mH$ and $C = 45 \mu F$ per phase – Distorted waveform.....	78

Figure 5.24 Test 8 – Simulated stator line current waveform with $R = 60 \Omega$ , $L = 60 \text{ mH}$ and $C = 45 \mu\text{F}$ per phase – Distorted waveform.....	78
Figure 5.25 Test 9 – Measured stator line current waveform with $L = 11 \text{ mH}$ , $R = 40 \Omega$ and $C = 45 \mu\text{F}$ per phase – Distorted waveform. ....	80
Figure 5.26 Test 9 – Simulated stator line current waveform with $L = 11 \text{ mH}$ , $R = 40 \Omega$ and $C = 45 \mu\text{F}$ per phase – Distorted waveform. ....	80
Figure 5.27 Stator line current $i_c$ versus $i_b$ phase plane diagram. ....	82
Figure 5.28 Sampled states of stator line current $i_{cn}$ versus $i_{bn}$ Poincaré map.	82
Figure 5.29 SEIG current FFT with an inductive load ( $R = 40 \Omega, L = 11 \text{ mH}$ ); The frequency and amplitude of the 1 <sup>st</sup> dominating signal are approximately $69 \text{ Hz}$ and $5 \text{ A}$ . ....	83
Figure 5.30 Stator three line current waveforms $R = 60 \Omega$ , $L = 70 \text{ mH}$ and $C = 45 \mu\text{F}$ per phase and the rotor shaft speed at $4101 \text{ rpm}$ – Chaotic behaviour.....	84
Figure 5.31 Stator three line current waveforms $R = 90 \Omega$ , $L = 90 \text{ mH}$ and $C = 45 \mu\text{F}$ per phase and the rotor shaft speed at $4126 \text{ rpm}$ – Chaotic behaviour.....	85
Figure 5.32 Stator three line current waveforms $R = 60 \Omega$ , $L = 73 \text{ mH}$ and $C = 45 \mu\text{F}$ per phase and the rotor shaft speed at $4177 \text{ rpm}$ – Chaotic behaviour.....	85
Figure 5.33 Stator three line current waveforms with $R = 60 \Omega$ , $L = 80 \text{ mH}$ and $C = 45 \mu\text{F}$ per phase and the rotor shaft speed at $4206 \text{ rpm}$ – Chaotic behaviour.....	86
Figure 5.34 Stator three line current waveforms with $R = 55 \Omega$ , $L = 91 \text{ mH}$ and $C = 45 \mu\text{F}$ per phase and the rotor shaft speed at $4356 \text{ rpm}$ – Chaotic behaviour.....	86
Figure 6.1 Stator line current waveform for $C = 135 \mu\text{F}$ , $R = 30 \Omega$ and $\omega_r =$ $314 \text{ rad/s}$ . ....	89
Figure 6.2 Phase plane diagram for $C = 135 \mu\text{F}$ , $R = 30 \Omega$ and $\omega_r = 314 \text{ rad/s}$ . .....	89

Figure 6.3 Bifurcation diagram with $C$ as the bifurcation parameter. ....	91
Figure 6.4 Bifurcation diagram with $C$ as the bifurcation parameter (zoom in). ..	91
Figure 6.5 Stator line current waveform for $C = 152 \mu F$ – Quasi-periodic response.....	92
Figure 6.6 Phase plane diagram for $C = 152 \mu F$ – Quasi-periodic response. ....	92
Figure 6.7 Stator line current waveform for $C = 156 \mu F$ – Quasi-periodic response.....	93
Figure 6.8 Phase plane diagrams for $C = 156 \mu F$ (with 5000 data points) - Quasi-periodic response.....	94
Figure 6.9 Dense orbit in the torus ( $i_{sQ}$ versus $i_{sD}$ with 20,000 data points).....	94
Figure 6.10 Poincaré sections for $C = 156 \mu F$ (sample at $i_{sD} = 0$ ).....	95
Figure 6.11 Bifurcation diagram with $R$ as the bifurcation parameter. ....	96
Figure 6.12 Stator line current waveform for $R = 28 \Omega$ – Quasi-periodic response.....	97
Figure 6.13 Phase plane diagram for $R = 28 \Omega$ – Quasi-periodic response. ....	97
Figure 6.14 Stator line current waveform for $R = 27 \Omega$ – Chaotic response. ....	97
Figure 6.15 Phase plane diagram for $R = 27 \Omega$ – Chaotic response. ....	98
Figure 6.16 Bifurcation diagram with $\omega_r$ as the bifurcation parameter. ....	98
Figure 6.17 Stator line current waveform for $\omega_r = 334.5 \text{ rad/s}$ – Quasi-periodic response.....	99
Figure 6.18 Phase plane diagram for $\omega_r = 334.5 \text{ rad/s}$ – Quasi-periodic response.....	99
Figure 6.19 Stator line current waveform for $\omega_r = 335.1 \text{ rad/s}$ – Quasi-periodic response.....	100
Figure 6.20 Phase plane diagram for $\omega_r = 335.1 \text{ rad/s}$ – Quasi-periodic response.....	100
Figure 6.21 Period-one Poincaré section; Base case without disturbance. ....	102
Figure 6.22 Period-one phase plane diagram; Base case with disturbance. ..	103

Figure 6.23 Period-one Poincaré section; Base case with disturbance. ....	103
Figure 6.24 Quasi-period phase plane diagram; $C = 156 \mu F$ with disturbance. .....	106
Figure 6.25 Quasi-period Poincaré section; $C = 156 \mu F$ with disturbance. ....	106
Figure 6.26 Eigenvalue map for changing capacitance. ....	109
Figure 6.27 Eigenvalue map for changing load resistance. ....	110
Figure 6.28 Eigenvalue map for changing rotor speed. ....	111

## TABLES

Table 3.1 Limit sets presented on ODEs and Poincaré maps.....	26
Table 5.1 List of tests carried out.....	57
Table 6.1 Sampled $i_{sQ}$ , $i_{rd}$ and $i_{rq}$ state variables when $i_{sD} = 0$ .....	104
Table 6.2 The Jacobian matrix, eigenvalue and magnitude of the complex conjugates derived from the sampled state variables under period-one orbit condition.....	105
Table 6.3 Sampled $i_{sQ}$ , $i_{rd}$ and $i_{rq}$ state variables when $i_{sD} = 0$ .....	107
Table 6.4 The Jacobian matrix, eigenvalue and magnitude of the complex conjugates derived from the sampled state variables under quasi-periodic orbit condition.....	108

## ABBREVIATIONS

AC	alternating current
DC	direct current
<i>d-q</i>	direct-quadrature
EC	equivalent circuit
ELC	electronic load controller
EMF	Electromotive Force
EU	European Union
FFT	Fast Fourier Transform
SEIG	Self-excited Induction Generator
IG	induction generator
IM	induction machine
IVP	initial value problem
ODE	ordinary differential equation
PWM	Pulse Width Modulation
RRF	rotor reference frame
SCIG	squirrel cage induction generator
SRF	stator reference frame

# CHAPTER 1

## INTRODUCTION

### 1.1 GENERAL INTRODUCTION

Apart from their general use as motors, three-phase induction machines (IMs) are also used as generators in electric power systems. The induction generator offers advantages for hydro and wind applications in terms of cost and simplicity and it plays an important part in the renewable energy industry today [1, 2, 3, 4].

However, the induction generator has its limitations; it generally needs an external power source to provide its excitation. This means that it is difficult to employ in remote areas where there is no electrical power supply network.

The possibility of using a Self-excited Induction Generator (SEIG) where a three-phase capacitor bank is connected across the stator terminals to supply the reactive power requirement of a load and generator was discovered by Basset and Potter in the 1930s [5]. When such an induction machine is driven by an external mechanical power source, the residual magnetism in the rotor produces an Electromotive Force (EMF) in the stator windings. This EMF is applied to the capacitor bank causing current flow in the stator winding and establishing a magnetising flux in the machine [6, 7]. An induction machine connected and excited in this manner is capable of acting as a standalone generator supplying real and reactive power to a load. In this mode of operation, the capacitor bank supplies the reactive power requirement of the load and generator and the real power demand of the terminal load is supplied by the prime mover.

However, the main drawback of the SEIG system is that the voltage and frequency produced by the system is highly dynamic under variable load conditions. Although many studies have been focused on regulating the voltage and frequency of the SEIG system under variable loads, the regulation of speed and voltage does not result in a satisfactory level of performance due to the nonlinear behaviour of the machine [8, 9, 10].

In an attempt to better understand the above problem, this thesis is focused on studying the steady-state nonlinear behaviour of the SEIG system when feeding an inductive load ( $RL$ ). Computer simulations, laboratory experimental tests and numerical analysis reveal a variety of highly nonlinear behaviours of the SEIG which have not been reported previously.

## 1.2 CONTRIBUTION OF THE THESIS

Induction machine cross-saturation nonlinear effect has been studied in the past two to three decades [6, 11, 12, 13]. However, none of these studies presents a complete analysis of the various types of nonlinear behaviours exhibited by the SEIG when feeding variable loads.

This thesis presents:

- The first complete study of the nonlinear dynamic behaviour of the SEIG using a nonlinear model of the machine to simulate the system.
- The first study in which numerical nonlinear analysis tools are applied to investigate the operating characteristics of the SEIG as a nonlinear dynamic system.
- The first examination of the periodic, quasi-periodic and chaotic behaviour of the SEIG when supplying a variable inductive load ( $RL$ ).
- The results of the SEIG Simulink model are not only compared with experimental test results, but also verified by the nonlinear numerical analysis tools.

The aim of the thesis is to provide a better understanding of the behaviour of the SEIG that would hopefully contribute to the development of a better regulated/controlled, viable SEIG system.

### 1.3 SCOPE OF THE THESIS

This research thesis contains seven main chapters.

The First Chapter provides the reader with a brief introduction of the work, the contribution of the thesis and the outline of the thesis.

The Second Chapter presents a brief literature review of the SEIG system and an overview of established nonlinear computer models for induction machines.

The Third Chapter gives an introduction to nonlinear dynamic systems, types of nonlinearities, nonlinear analysis tools and stability analysis methods.

The Fourth Chapter presents the Simulink model used to investigate the behaviour of the SEIG system when feeding variable loads. A linear conventional IG model is introduced to the reader first as a foundation for the development of the nonlinear model of the SEIG system. Magnetic cross-saturation effects are then incorporated into the induction machine model to produce a current based nonlinear IG model. The dynamic model of the system is completed by incorporating a capacitor bank connected to the stator terminals into the model which is needed to provide reactive power to both the generator and the load. The initial self-excitation process of the SEIG obtained from the nonlinear model is compared with those obtained from a well-known publication [14]. The behaviour of the SEIG model is then examined when feeding a purely resistive load connected to the stator terminals.

A number of laboratory tests are presented in the Fifth Chapter. An SEIG test rig (using a 1.1 kW induction machine) is tested when feeding variable loads under controlled laboratory conditions. The results from these experimental tests are analysed and used to demonstrate the performance of the SEIG system. Laboratory results are compared with simulation waveforms showing very good agreement and confirming the validity of the model.

Based on the simulation results obtained from the nonlinear model of the SEIG system, the Sixth Chapter presents a study of the dynamic performance of the system by employing modern nonlinear numerical analysis tools. The performance characteristics of the system (e.g. stability and frequency regulation) when supplying an inductive load ( $RL$ ) are studied by considering the

effects of the following three parameters: 1) changing the power factor of the load; 2) changing the rotor speed and 3) changing the value of the self-excitation capacitance. Finally, the SEIG performance is analysed using nonlinear numerical analysis tools and computer simulations to establish the nonlinear characteristics of the system.

The Seventh Chapter presents the conclusions and discussions of the thesis and suggestions for future work.

#### **1.4 PUBLICATION**

D. D. Ma, B. Zahawi, D. Giaouris, S. Banerjee and V. Pickert, "Nonlinear Behaviour of Self-excited Induction Generator Feeding an Inductive Load," *PEDES International Conference on Power Electronics, Drives and Energy Systems, New Delhi, India*, pp. 1-5, December 12-15, 2006.

## CHAPTER 2

### THE SEIG SYSTEM REVIEW

The ever increasing demand for energy, the depletion of conventional energy resources and the degradation of environmental conditions throughout the world have led governments/scientists/researchers to explore renewable or nonconventional energy sources (e.g. wind, hydro, solar, bio-energy and micro-generation) in recent two to three decades. Renewable energy is the key to our low carbon energy future. In early 2008, European Union (EU) Commission aimed to achieve a 2020 target of deriving 20% of the EU's energy consumption from renewable sources, while the UK government proposed to achieving 15% renewable target by 2020 [15].

The use of an induction machine as a generator is becoming more and more popular for renewable energy applications [4, 12, 16, 17]. Squirrel cage induction generators with excitation capacitors (known as SEIGs) are popular in isolated nonconventional energy systems [3, 4, 18].

As discussed in the previous chapter, the main limitation of the SEIG system is the poor voltage and frequency regulation when supplying variable loads connected to the stator terminals. However, the development of static power converters has facilitated the control of the output voltage and frequency of the induction generator. This chapter presents a literature review of the development, the self-excitation phenomena, the performance and the operational problems of the SEIG system. This is followed by an historical overview of computer modelling techniques of the SEIG based on cross-saturation effect, the saturation of leakage inductance, the machine H-G diagram and the skin effect.

## 2.1 SEIG SYSTEM CONFIGURATION

The SEIG system is composed of four main items: the prime mover, the induction machine, the load and the self-excitation capacitor bank. The general layout of the SEIG system is shown in Figure 2.1.

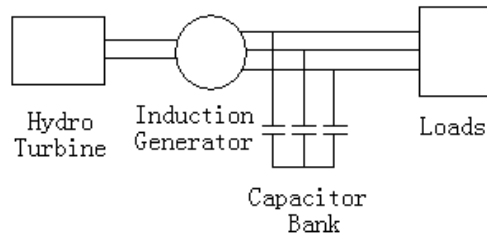


Figure 2.1 Schematic diagram of a standalone self-excited induction generator.

The hydro/wind turbine is assumed to operate with constant input power transferred to the induction generator. The real power required by the load is supplied by the induction generator by extracting power from the prime mover (turbine). When the speed of the turbine is not regulated, both the speed and shaft torque vary with variations in the power demanded by the loads. The self-excitation capacitors connected at the stator terminals of the induction machine must produce sufficient reactive power to supply the needs of the load and the induction generator.

A squirrel cage induction generator (SCIG) is more attractive than a conventional synchronous generator in this type of application because of its low unit cost, absence of DC excitation source, brushless cage rotor construction and lower maintenance requirement [18, 19]. A suitably sized three-phase capacitor bank connected at the generator terminals is used as variable lagging VAr source to meet the excitation demand of the cage machine and the load. The machine operated in this mode is known as a *Self-excited Induction Generator* (SEIG) [12]. However, the main drawback of the standalone SEIG is its poor voltage and frequency regulations under variable loads. A change in the load impedance directly affects the excitation of the machine because the reactive power of the excitation capacitors is shared by both the machine and the load. Therefore, the generating voltage drops when

the impedance of the load is increased resulting in poor voltage regulation. Poor frequency regulation occurs (an increase in the slip of the induction machine) when the load is increased.

## **2.2 OVERVIEW OF THE SELF-EXCITED INDUCTION GENERATORS**

Owing to increased emphasis on renewable resources (such as small hydro, wind, solar, tidal and wave) and their variable speed nature, the performance of synchronous generators can be greatly affected. Hence, SEIGs have emerged as suitable candidates for isolated power sources to convert power at the shaft of wind/hydro turbines into electrical energy [4, 20, 21].

### **2.2.1 OVERVIEW OF THE DEVELOPMENT OF THE SEIG**

Basset and Potter first discovered the possibility of using an induction machine as a SEIG during the 1930s. An induction machine operates as a generator if an appropriate supply of inductive VARs is available to provide the machine's excitation at a certain rotational speed. Self-excitation can be achieved by the connection of suitable capacitors at the machine's stator terminals. The lagging VARs supplied by the capacitors is consumed by the machine's excitation, leakage reactance and the reactance of the inductive load.

Although the SEIG scheme was discovered more than eighty years ago, a large number of research papers are only increasingly focused on the investigation and applications of SEIGs in the recent two/three decades [4, 18]. This is due to the improving voltage and frequency control techniques and the worldwide vast attention on the development of renewable energy sources over the past thirty years.

In 1982, Murthy et al. developed a mathematical model for obtaining the steady-state performance of a SEIG by using the equivalent circuit (EC) of the induction machine [22]. The Newton-Raphson method was used to obtain the operating frequency and the magnetising reactance from the nonlinear equations of the system. A year later, Quazene et al. developed a nodal equation to solve for the operating frequency and then the magnetising reactance by using a nodal admittance technique [23].

Tandon et al. presented an alternative approach to the steady-state performance analysis of a stand-alone SEIG using balanced terminal capacitors in 1984 [24]. The predicted steady-state performance of the SEIG under different load conditions by operational ECs matched well with corresponding experimental results.

In 1993, a mathematical model for the EC of a SEIG was used to solve the nonlinear equation for the operating frequency by an iterative technique by Rajakaruna and Bonert [25]. Two years later, Chan proposed an iterative technique to solve for the value of the operating frequency by considering a small increment in the operating frequency (an initial value of the operating frequency was assumed) [26].

In order to capture more wind energy under variable wind speed conditions, a pole changing method of SEIGs was investigated in [27, 28]. The requirements for the excitation capacitor, machine flux density, maximum electromagnetic torque, output power and stator terminal voltage under different pole configurations were discussed by Chatterjee and Khan [28]. It was observed that the stator current was smaller, capacitor requirement was less (around 44%) and power output was about 2.5 times larger in a four-pole than the corresponding results from a six-pole configuration. Hence, the conclusion led to the four-pole configuration generated better utilisation of the SEIG rating than the six-pole configuration.

In 1997, Wang et al. predicted the minimum and maximum values of capacitance required for the self-excitation of the SEIG by an eigenvalue based approach [29].

An analysis of the steady-state performance of SEIGs driven by both regulated and unregulated turbines was presented in [30, 31]. The steady-state performance of a standalone SEIG with a transformer connected to its terminal was analysed in [32]. The function of the transformer was to step up the stator terminal voltage or to supply a different voltage to the load. At relatively high rotational speeds, the saturated transformer was able to absorb reactive power and regulate the terminal voltage. However, such a transformer introduced an additional nonlinearity into the system, which complicates the analysis process.

A general analysis of a three-phase SEIG with asymmetrical connected loads and excitation capacitors by adopting the symmetrical components method was presented in 2001 [33].

In the past few decades, other papers have been focused on the analysis of the transient voltage built up of SEIGs [34, 35, 36].

By taken into account the magnetic saturation nonlinear effect, the influence of the terminal capacitors on the transient behaviour of an induction machine was studied by Smith et al. in 1968 [37]. The tests showed that it was not advisable to reconnect a capacitor excited induction generator to the busbar, unless the interruption is of short period. The results also indicated that the saturation of the main flux path does not affect the transient behaviour of the machine without self-excited capacitors.

The self-excitation voltage built up process in a standalone SEIG was analysed by Wang et al. in 1999 [38]. They examined the SEIG under unbalanced excitation capacitor conditions (by the sudden switching of one excitation capacitor or two excitation capacitors). The results showed that the SEIG could maintain the self-excitation process and generate the other two phase voltage when one phase capacitor was switched off. However, the SEIG voltage collapses when two phase capacitors were cut off.

A year later, Wang et al. presented a comparison study of different shunt capacitor configurations of an isolated SEIG feeding an induction motor load [39]. Their analysis showed that the short-shunt connection provided better voltage regulation, whereas the long-shunt connection might cause unwanted oscillations. The eigenvalue technique was employed to examine the unstable operating conditions of the SEIG system.

The dynamic behaviour of the SEIG was experimentally investigated by Levy in 1997 [40]. However, under variable speed conditions with a fixed capacitor bank connected to the stator terminals, testing led to voltage collapsing and the demagnetisation of the machine.

The transient performance of a three-phase SEIG under balanced and unbalanced fault conditions was studied in [41]. The effects of main and cross flux saturation under load perturbation, three-phase or line-to-line short circuit,

switching off one or two capacitor(s), opening of single or two phase load conditions were considered.

Due to small hydro and wind generating systems having constraints on the size of individual machines, several induction generators were connected in parallel by Farret et al. in order to achieve full performances on site [42]. The transient behaviour of the parallel connected SEIGs could not be easily modelled by conventional models because of its fast transient nature. Therefore, the previous work related to transient analysis of SEIGs did not clearly correspond to experimental observations. An innovative and automatic numerical solution of the steady-state and transient analysis of any number of SEIGs operating in parallel was presented in [42]. The nonlinear relationship between airgap voltage and magnetising current was described by a fourth order polynomial curve fit. It was possible to have a mathematical description of the machine models, the self-excitation capacitor bank and the load. The data generated from the experimental testing confirmed the accuracy of the proposed mathematical model.

Many of these articles have been focused on analysing the steady-state and transient performance of SEIGs from the design and operational point of view. This thesis, on the other hand, is focused on studying and analysing the steady-state, nonlinear behaviour of the SEIG system as a nonlinear dynamic system. The presence of the capacitor bank together with the saturated magnetic circuit of the induction generator produces a nonlinear dynamic system with the possibility of chaos. Qualitative changes in the system dynamics (for example a change in system frequency) are called Bifurcations [43]. The behaviour of a nonlinear dynamic system can change dramatically with a small change in system parameters. SEIG nonlinear phenomenon such as quasi-periodicity, chaotic behaviours and bifurcations are studied and analysed in this thesis.

### **2.2.2 THE SELF-EXCITATION PHENOMENON**

The self-excitation phenomenon of an induction machine is still under considerable attention although it is known for more than a half century [44, 45, 46]. When a standalone induction machine is driven by a mechanical prime mover, the residual magnetism in the rotor of the machine induces an EMF in the stator windings at a frequency proportional to the rotor speed. This EMF is applied to the capacitors connected to the stator terminals and causes reactive current to flow in the stator windings. Hence a magnetising flux in the machine is established. The final value of the stator voltage is limited by the magnetic saturation within the machine. The induction machine is then capable of operating as a generator in isolated locations without a grid supply.

Once the machine is self-excited and loaded, the magnitude of the steady-state voltage generated by the SEIG is determined by the nonlinearity of the magnetising curves, the value of the self-excitation capacitance, speed, machine parameters and terminal loads. As the load and speed of the SEIG changes, the demand for lagging VARs to maintain a constant AC voltage across the machine terminals also changes [47]. Arrillaga and Watson predicted the effect of a resistive load on the frequency of the generator where a new operating point was obtained by shifting the saturation curve and capacitive load in the terminal voltage-current characteristics [48]. The effect of an inductive load was also studied and experimentally verified in [47, 48].

### 2.2.3 SEIG SYSTEM PERFORMANCE

The performance characteristics of the SEIG system depend mainly on the following:

- The parameters of the induction machine  
The machine operating voltage, rated power, power factor, rotor speed and operating temperature and the induction machine parameters directly affect the performance of the SEIG system.
- The Self-excitation process  
The connection of a capacitor bank across the induction machine stator terminals is necessary in the case of standalone operation of the system. The capacitor connection scheme (delta or star) and the use of fixed or controlled self-excitation capacitors have a direct impact on the performance of a SEIG system.
- Load parameters  
The power factor, starting/maximum torque and current, generated harmonics and load type also affect the performance of the SEIG system directly.
- Type of prime mover  
Whether the primary source is hydro, wind biomass or combinations, the performance of the SEIG system is affected.

### 2.2.4 OPERATIONAL PROBLEMS OF THE SEIG SYSTEM

The main operational problem of the SEIG system is its poor voltage and frequency regulation under varying load conditions [49, 50, 51]. A change in the load impedance directly affects the machine excitation. This is because the reactive power of the excitation capacitors is shared by both the induction machine and the load impedance. Therefore, the generator's voltage drops when the load impedance is increased resulting in poor voltage regulation. On the other hand, the slip of the induction generator increases with increasing load, resulting in a load dependant frequency, even if the speed of the prime mover remains constant.

Many studies have been conducted in the past to regulate the voltage and frequency of a SEIG system operating with variable loads [9, 49, 52, 53]. A high cost speed governor is generally used as a conventional SEIG controller.

A strategy of controlling voltage and frequency of a SEIG system was presented by Suarez et al. in 1999 [49]. Sliding mode controller was proposed showing controlled dynamic response and behaviour of the system upon changes in generator parameters and load. However, an accurate transient model of representing instantaneous phase angle between stator voltage and external inductor current at switching instant is highly recommended in order to achieve optimal control.

Regulating voltage and frequency of a SEIG under varying load conditions by an electronic load controller (ELC) was examined by Singh et al. in 2006 [52]. The ELC consists of a chop circuit and a rectifier which produces harmonics during operation. AC current harmonics generated by ELC during operation and their impact on the performance of the SEIG were studied in [52].

In 2008, Youssef et al. presented a method of voltage and frequency regulation of an induction generator under islanding mode [53]. A constant voltage and constant frequency PWM converter was used by eliminating the need of an auxiliary switch in the DC side, which in turn reduced cost and high frequency current components. The results of the proposed method showed the same response as the technique of including the DC side switch. The control

technique was proved to work well under sudden changes in load and rotational speed.

In most of these studies, the control of the terminal voltage is generally performed by controlling a variable reactive power source and frequency regulation is achieved by regulating the speed of the prime mover by utilising a mechanical speed governor. However, the regulation of speed and voltage does not result in a satisfactory level of performance due to the highly dynamic changes in slip of the machine and the difficulties in building a smooth variable reactive power source at low costs.

In order to contribute to a solution of the above operational problems, this thesis presents an investigation of the steady-state nonlinear behaviour of the SEIG system when feeding variable inductive loads (*RLs*). The analysis of this highly dynamic nonlinear system reveals a variety of unique behaviours which have not been previously reported.

## **2.3 MODELLING OF THE SEIG AS A NONLINEAR SYSTEM**

After the self-excitation process in a SEIG is initiated, the final value of the stator voltage is limited by magnetic saturation in the machine. The induction machine exhibits nonlinear characteristics under saturated condition. Once the machine is loaded, the magnitude of the voltage generated is determined by the nonlinearity of the magnetising characteristics, the value of capacitance, speed, machine parameters and terminal load. Many studies have been carried out in the past to model the self-excited induction machine system. It is important to model the nonlinearity of the induction machine in order to fully understand the behaviours of this highly dynamic system.

### **2.3.1 NONLINEAR INDUCTION GENERATOR MODELLING BASED ON THE CROSS-SATURATION EFFECT**

Several papers have been published in the past detailing the transient equations of smooth airgap induction machines with a focus on the cross-saturation nonlinear effect [11, 54, 55, 56, 57]. It is generally believed that a change in the quadrature axis magnetising current will cause a change of flux linkage in the direct axis windings and vice versa. Under core saturation conditions, the airgap flux density distribution over one half of the pole-pitch is decreased by a greater amount than the increase under the other half of the pole-pitch [54]. The mathematics in these papers was focused on the modelling of the mutual inductance as a nonlinear function of current. This nonlinear modelling approach works well under normal operating conditions.

Levi investigated the impact of cross-saturation on the accuracy of different types of saturated induction machine models [57]. Two transient induction machine models (one with induction generator self-excitation and the other with motor starting with increased voltage) were analysed in the paper. Poor results were generated from the models where the cross-saturation effect was neglected. However, the nonlinear models are more complicated, requiring time derivative of the inverse of the inductance matrix when considering the cross-saturation effect.

### **2.3.2 NONLINEAR INDUCTION GENERATOR MODELLING BASED ON THE SATURATION OF LEAKAGE INDUCTANCE EFFECT**

Several researchers/scientists were interested in modelling induction machines with a focus on the saturation of leakage inductance nonlinear effect [56, 58, 59]. An interesting paper written by Lipo et al. analysed the induction machine by considering the saturating leakage reactance, a completely different concept to that of the cross-saturation [58]. Large starting currents flowing in the machine during acceleration can cause large values of slot leakage flux in both stator and rotor. This often leads to the saturation of the teeth of the machine. A key step in this approach is to separate stator and rotor leakage inductance into slot (teeth) and end winding (core) portions. The teeth are considered to be saturated (nonlinear inductance) while the core is considered to be unsaturated (constant inductance). The analysis of the induction generator based on saturation of leakage inductance effect is focused on teeth saturation whereas the cross-saturation nonlinear model considers core saturation. Hence, it was concluded that the nonlinear approach of modelling induction generators based on saturation of leakage inductance is usually applied to high power industrial motor drives under large inrush current conditions [58].

### 2.3.3 NONLINEAR INDUCTION GENERATOR MODELLING BASED ON THE H-G DIAGRAM

The H-G diagram is another effective nonlinear technique for modelling induction machines [60, 61, 62]. The diagram represents one of the most recent approaches to induction motor modelling to include temperature and saturation effects. The diagram uses only three parameters (such as slip frequency, stator inductance and total leakage coefficient) instantaneously determined by plotting a circle (H-G diagram) to describe the saturation in the machine. G and H represent the real and imaginary part of the induction machine stator winding input impedance [60].

A nonlinear model proposed by Benbouzid et al. for a 0.75 kW induction machine based on H-G diagram showed good results at the starting phase of the induction motor or when sufficient load is applied to the machine [61]. It was initially believed that the H-G diagram approach could produce the same dynamics of the nonlinear system as the cross-saturation method. The torque and speed transients obtained from the H-G diagram method were in good agreement with those obtained from the cross-saturation model. However, the steady-state results generated from the H-G diagram were not as accurate as those obtained from the cross-saturation model unless sufficient load was applied to the stator terminals.

### 2.3.4 NONLINEAR INDUCTION GENERATOR MODELLING BASED ON THE SKIN EFFECT

Another nonlinear modelling method was presented through the consideration of the skin effect phenomenon in [63, 64, 65]. This approach is focused on creating a nonlinear mathematical function of frequency for the system. Skin effect occurs when the leakage flux causes the current to crowd towards the top of the bar adjacent to the airgap where bar conductors are contained in slots. This nonlinear effect has a direct impact on the dynamic behaviour of the induction machine. Due to skin effect, the effective cross section of the rotor conductor is reduced, which causes a decrease in the leakage inductance and in turn increases the amplitude of stator current. Moreover, the copper loss becomes greater by an increased rotor resistance. Hence, the analytical formula of modelling the skin effect to relate rotor resistance and inductance as a function of its rotor bar dimensions and frequency can be solved by adapting Maxwell's equation. Experimental results for a 7.5 hp induction machine verified the accuracy of the proposed nonlinear SEIG model with the consideration of skin nonlinear effect in the case of no-load condition [63].

Another model presented by Okoro for a 7.5 kW wind turbine driven squirrel cage induction generator with the consideration of skin effect showed that the calculated inrush currents and the machine accelerating time were more accurate than those obtained from conventional/linear models. However, the accuracy level could be further improved by considering the saturation nonlinear effect [65].

The most widely used induction machine transient state model is the  $d$ - $q$  (direct-quadrature) axis frame of reference representation. The  $d$ - $q$  axis model provides a convenient way for variable solutions of dynamic systems. In this thesis the  $d$ - $q$  axis model will be utilised along with the representation of the cross-saturation nonlinear effect to emulate the SEIG system due to its accuracy and robustness.

## 2.4 SUMMARY

An overview of the self-excitation phenomenon and the historic development of the SEIG was presented in this chapter. The performance characteristics and operational problems of SEIG systems together with a review of different approaches to the nonlinear modelling of induction machines were also given.

The prime mover, the induction machine, the load and the self-excitation capacitors are the four main items comprising the SEIG system.

A brief overview of the steady-state and transient analysis of the SEIG system as presented in the literature was carried out in this chapter. Most researchers/scientists have been focused on analysing the steady-state and transient performance of SEIGs from the design and operational point of view. However, this thesis is focused on studying and analysing the steady-state nonlinear behaviour of the SEIG system as a nonlinear dynamic system.

The parameters of the induction machine, the self-excitation process, the load parameters and type of primary mover are the main factors affecting the behaviour of the SEIG system.

Poor voltage and frequency regulation are two major drawbacks of the SEIG system under variable load conditions. This thesis presented an investigation of this highly dynamic nonlinear system revealing a variety of unique behaviours in order to contribute to the understanding of the above operational problems.

Various nonlinear modelling techniques of induction machines, such as based on cross-saturation effect, saturation on leakage inductance effect, H-G diagram and skin effect were considered in this chapter. The cross-saturation nonlinear effect technique was shown to have numerous advantages (e.g. most accurate and robust) over the other computer modelling techniques mentioned above.

The  $d$ - $q$  axis state space mathematical model of the SEIG system feeding a variable load, implemented in Matlab/Simulink (version: R2010b), with consideration of the cross-saturation effect was used in this investigation and the results verified experimentally.

# CHAPTER 3

## NONLINEAR DYNAMIC SYSTEMS

This chapter presents a brief and general mathematical background and the analytical tools required to investigate the SEIG system as a nonlinear dynamic system.

### 3.1 NONLINEAR DYNAMIC SYSTEMS

A dynamic system is an object, or a set of objects, that has the ability to change its state with respect to time, possibly under external excitations. In other words, any system whose status changes with time is a *dynamic system*. In mathematical language, a dynamic system can be expressed in terms of  $X, T$  and  $\varphi^t$  where  $X$  is a *state space* including all possible states of a system (state space is also known as phase space),  $T$  is a time set, and  $\varphi^t$  is a family of evolution operators [66].

It is generally known that there are two types of dynamic system equations: differential equations and difference equations (also known as iterated maps or Poincaré maps). *Differential equations* describe the evolution of systems in continuous-time, whereas *iterated maps* analyse the evolution of systems in discrete-time domain. Difference equations can be useful in reducing the order of a dynamic system [66]. In fact, the Poincaré map technique is adopted in this thesis to study the dynamics of the SEIG system.

### 3.1.1 DIFFERENTIAL EQUATIONS

An ordinary differential equation (ODE) of a continuous-time, autonomous dynamic system together with its initial condition is defined as an *initial value problem* (IVP)

$$\dot{\mathbf{x}} = f(\mathbf{x}), \quad \mathbf{x}(t_0) = \mathbf{x}_0 \quad (3.1)$$

where  $\dot{\mathbf{x}} = d\mathbf{x}/dt$ ,  $\mathbf{x}(t) \in \mathbb{R}^n$  is the state of the system at time  $t$ ,  $\mathbb{R}^n$  is called the set of all real vectors with  $n$  entries or the  $n$ -dimensional Euclidean space,  $f$  is referred to as the vector field and  $\mathbf{x}(t_0) = \mathbf{x}_0$  is the initial condition of the dynamic system. The solution or flow of the IVP (3.1) is often written as  $\boldsymbol{\varphi}_t(\mathbf{x})$ .

An *autonomous system* is defined as the system equations do not have any external applied time varying input or other time variations by not containing any time dependant term on the right hand side of (3.1) [67]. Therefore, the initial time is normally taken as  $t_0 = 0$ .

An IVP of a continuous-time, non-autonomous dynamic system is defined as

$$\dot{\mathbf{x}} = f(\mathbf{x}, t), \quad \mathbf{x}(t_0) = \mathbf{x}_0 \quad (3.2)$$

A system with external inputs or forcing functions or time variations is called a *non-autonomous system* [68]. For a non-autonomous system (3.2), the right-hand side  $f(\mathbf{x}, t)$  of the equation depends explicitly on time and the initial time  $t_0$  is not usually set to 0.

This thesis is focused on autonomous systems as a SEIG system is a time independent system.

### 3.1.2 DIFFERENCE EQUATIONS

A discrete-time dynamic system is defined by the following difference equation

$$\mathbf{x}(k+1) = f(\mathbf{x}(k)), \quad k = 0, 1, 2 \dots \quad (3.3)$$

where  $\mathbf{x}(k) \in \mathbb{R}^n$  is the state vector and  $f$  maps the state  $\mathbf{x}(k)$  to the next state  $\mathbf{x}(k+1)$ .

Discrete-time systems are useful for studying continuous-time systems like the SEIG by reducing the order of the system equations. The use of discrete equations also avoids the need to solve complicated differential equations.

### 3.2 POINCARÉ MAPS

The Poincaré map technique is a powerful tool in studying continuous-time dynamic systems. Using this technique, an  $n^{\text{th}}$  order continuous-time system is replaced with an  $(n - 1)^{\text{th}}$  order discrete-time system. In other words, a *Poincaré map* is a classical technique that transforms a continuous-time system to a reduced order discrete-time system. The steady-state behaviour (limit set) of a Poincaré map corresponds to steady-state behaviour of the underlying flow of a continuous-time system bridging the gap between continuous and discrete-time systems [69].

Consider a general  $n$ -dimensional autonomous system  $\dot{x} = f(x)$  with initial condition  $x(t_0) = x_0$  and a periodic orbit  $x_p$  (Figure 3.1 ). The dimension of the state space is  $n$  and  $S_{n-1}$  is a  $(n - 1)$  dimensional surface not parallel to the trajectory. Point  $x^*$  (the fixed point) is the intersection between the limit cycle and surface  $S_{n-1}$ . A new coordination system  $V$  on  $S_{n-1}$  is defined to reduce the order of the original system.

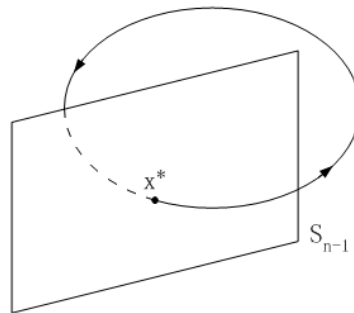


Figure 3.1 Poincaré map of a periodic autonomous system.

Figure 3.2 shows a small perturbation  $\Delta x$  added onto the trajectory such that

$$\mathbf{x}(t) = \mathbf{x}_p(t) + \Delta \mathbf{x}(t).$$

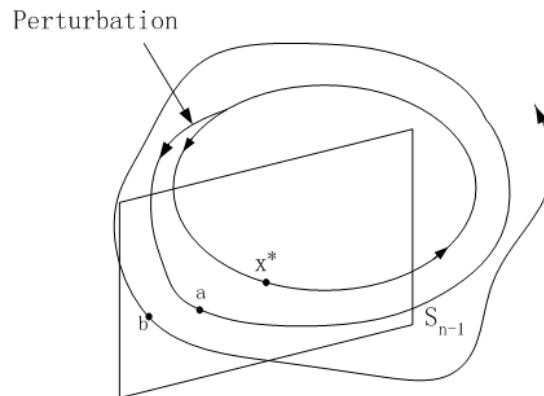


Figure 3.2 Poincaré map of a periodic autonomous system with perturbation.

The intersections can be described by the points:  $a \rightarrow b$ . Therefore, to go from point  $a$  to point  $b$ , there shall be a map  $\mathbf{V}_b = P(\mathbf{V}_a)$  (continuous function) or described in more general terms  $\mathbf{V}_{k+1} = P(\mathbf{V}_k)$  (discontinuous function).  $P$  is the relation/formula between vector  $\mathbf{V}_a$  and  $\mathbf{V}_b$ . This map is referred to as the Poincaré map. However, it is sometimes difficult to find an explicit formula for such a map.

If the disturbance approaches the original limit cycle, the orbit is said to be stable. If however, the disturbance converges to another steady-state, the limit cycle is said to be unstable.

### 3.3 LIMIT SETS

There are four types of limit sets of continuous-time and discrete-time dynamic systems. Moving from the simplest to the most complex these are: equilibrium points, periodic solutions, quasi-periodic solutions and chaos.

The following steady-state behaviour is described from both continuous-time and discrete-time dynamic system points of view.

#### 3.3.1 FIXED POINTS

A *fixed point* of a continuous-time autonomous dynamic system (equation (3.1)) marked as  $x^*$  is defined by  $f(x^*) = 0$  and  $x^* = \varphi_t(x^*)$  for all  $t$  [69].

A fixed point is sometimes called an equilibrium, rest or stationary point.

The limit set of an equilibrium point is simply the equilibrium point itself.

#### 3.3.2 PERIODIC SOLUTIONS

If, for system (3.1), a relation  $x(t+T) = x(t)$  exists for all  $t$  where  $T$  is a constant  $> 0$ , the function  $x(t)$  is called *periodic* and  $T$  is its period. If the neighbourhood of a periodic solution has no other periodic solution, this closed curve in the phase plane is called a *limit cycle*.

The limit set of a limit cycle is the closed trajectory traced over for one period. Whereas the limit set corresponding to a limit cycle on a Poincaré map is a fixed point  $x^*$  (shown in Figure 3.1 ).

#### 3.3.3 QUASI-PERIODIC SOLUTIONS

When two or more frequencies appear in an autonomous system and if the ratio of frequencies is not a ratio of integers, the signal is *quasi-periodic*. The number of fundamental frequencies is called the degree of quasi-periodicity.

A degree 2 quasi-periodic trajectory lies on a torus in the phase space. Although the trajectory does not pass through every point on the torus surface, it repeatedly comes arbitrarily close to every point on the torus. The trajectory winds around on the torus surface endlessly, never intersecting or quite closing on itself. Thus, the limit set of a degree 2 quasi-period solution is torus shaped.

The steady-state of a degree 2 quasi-periodic orbit shown on a Poincaré map is an embedded circle as displayed in Figure 3.3.

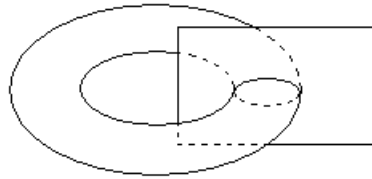


Figure 3.3 The limit set of the Poincaré map in the case of a degree 2 quasi-periodic orbit is an embedded circle.

### 3.3.4 CHAOTIC BEHAVIOUR

There is no widely accepted definition for chaos. It is generally agreed that chaotic behaviour is not an equilibrium point, not periodic and not quasi-periodic. It is however a bounded steady-state behaviour [69]. The chaotic orbit is so sensitive to initial conditions that the outcome after time  $t$  is totally unpredictable despite the fact that the system itself could be completely described by very simple mathematical equations with no external influences.

The limit sets of chaotic motion are not simple points, circles or tori, they are complicated strange attractors.

The limit set on a Poincaré map for chaotic motion is not a simple geometrical object but a fine structure. An example of such strange attractor is shown in Figure 3.4.

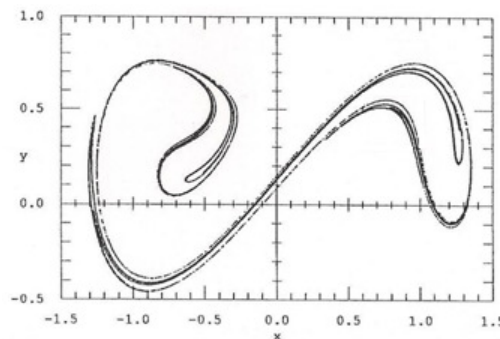


Figure 3.4 The limit set of the Poincaré map for a chaotic system [69].

Table 3.1 summarises the above mentioned steady-state behaviours for dynamic systems.

Table 3.1 Limit sets presented on ODEs and Poincaré maps.

Limit sets	ODEs	Poincaré maps
Fixed point	Fixed point	n/a
Periodic solution	Closed cycle traced over for one period	Fixed point
Quasi-periodic solution	Torus shape	Embedded circle
Chaotic	Complicated strange attractors	Fine structure

### 3.4 STABILITY OF LIMIT SETS

The study of the stability of limit sets is of great importance in analysing the behaviour of a nonlinear dynamic system.

One popular approach to determine the stability of a limit set is by placing a small perturbation to the original nonlinear system. The fixed point is stable if the solution converges back to the original fixed point and is unstable otherwise.

As the Poincaré map technique is utilised in analysing the stability of the SEIG nonlinear system (Chapter Six), the following discussions are focused on discrete-time dynamic systems.

### 3.4.1 STABILITY OF A FIXED POINT

Consider the following discrete-time dynamic system

$$\mathbf{x}_{n+1} = f(\mathbf{x}_n) = \mathbf{A}\mathbf{x}_n \quad (3.4)$$

Firstly, in order to find the fixed point of the system (3.4), the following formula needs to be observed

$$\mathbf{x}_{n+1} = \mathbf{x}_n = \mathbf{x}^* \quad (3.5)$$

Secondly, the Jacobian matrix  $\mathbf{A}$  can be obtained by linearising the system locally in a neighbourhood of the fixed point  $\mathbf{x}^*$ . A *Jacobian matrix* contains all first-order partial derivatives of a vector-valued function [67].

The local linearisation of the system at the fixed point  $\mathbf{x}^*$  in state space is given by

$$\begin{pmatrix} x_2 \\ x_3 \\ \vdots \\ x_{n+1} \end{pmatrix} = \begin{pmatrix} \frac{\partial f_1}{\partial x_1} & \frac{\partial f_1}{\partial x_2} & \dots & \frac{\partial f_1}{\partial x_n} \\ \frac{\partial f_2}{\partial x_1} & \frac{\partial f_2}{\partial x_2} & \dots & \frac{\partial f_2}{\partial x_n} \\ \vdots & \vdots & \ddots & \vdots \\ \frac{\partial f_n}{\partial x_1} & \frac{\partial f_n}{\partial x_2} & \dots & \frac{\partial f_n}{\partial x_n} \end{pmatrix}_{\mathbf{x}^*} \times \begin{pmatrix} x_1 \\ x_2 \\ \vdots \\ x_n \end{pmatrix} \quad (3.6)$$

where the Jacobian matrix  $\mathbf{A}$  (evaluated at  $\mathbf{x}^*$ ) is given by

$$\mathbf{A} = \begin{pmatrix} \frac{\partial f_1}{\partial x_1} & \frac{\partial f_1}{\partial x_2} & \dots & \frac{\partial f_1}{\partial x_n} \\ \frac{\partial f_2}{\partial x_1} & \frac{\partial f_2}{\partial x_2} & \dots & \frac{\partial f_2}{\partial x_n} \\ \vdots & \vdots & \ddots & \vdots \\ \frac{\partial f_n}{\partial x_1} & \frac{\partial f_n}{\partial x_2} & \dots & \frac{\partial f_n}{\partial x_n} \end{pmatrix}_{\mathbf{x}^*} \quad (3.7)$$

The eigenvalues of the Jacobian (3.7) can now be calculated, indicating the stability of the fixed point  $\mathbf{x}^*$ .

In a discrete-time system, a fixed point is stable if all the eigenvalues of the Jacobian matrix have magnitude(s) less than unity. Equally, a fixed point is stable only if all the real parts of the eigenvalues are negative in a continuous-time dynamic system.

### 3.4.2 STABILITY OF A PERIODIC SOLUTION

As discussed in Section 3.3.2, the limit set of a periodic solution on a Poincaré map is a fixed point. The stability of a periodic solution can therefore, be investigated by introducing the Poincaré map technique and calculating the eigenvalues of the Jacobian matrix corresponding to the resulting fixed point.

From a graphical point of view, if the perturbed trajectory approaches the fixed point, the fixed point is stable. Whereas, the fixed point is unstable if the perturbed trajectory is moving away from the fixed point.

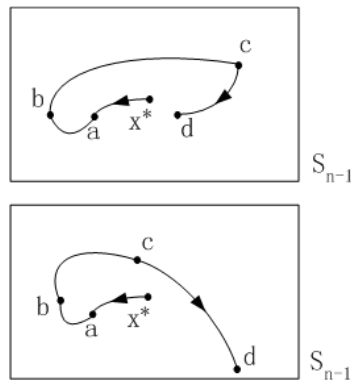


Figure 3.5 Two perturbed trajectories; stable case (top) and unstable case (bottom).

The top graph of Figure 3.5 shows that point  $d$  is getting closer to the fixed point  $x^*$ . Therefore, it has stable orbits. Whereas the bottom graph leads to unstableness as  $d$  is moving away from  $x^*$ .

Further discussions associated with the stability of the periodic solution for the SEIG system are presented in Chapter Six.

### 3.4.3 STABILITY OF A QUASI-PERIODIC SOLUTION

The stability of a quasi-periodic trajectory is also investigated by introducing the Poincaré map technique and evaluating the eigenvalues of the corresponding Jacobian matrix.

As discussed in Section 3.3.3, the limit set of a quasi-periodic waveform on a Poincaré map is an embedded circle. The fixed point can be found at the middle of the closed loop. Therefore, the problem can be reduced to the stability of the fixed point from the corresponding Poincaré section.

From a graphical point of view (Figure 3.6), if the iterates spiral into the fixed point, this fixed point is stable. However, if the iterates spiral out to the closed circle on the Poincaré section, the fixed point is unstable [67]. Figure 3.6 shows an example of both the stable and unstable cases for a degree 2 quasi-periodic system.

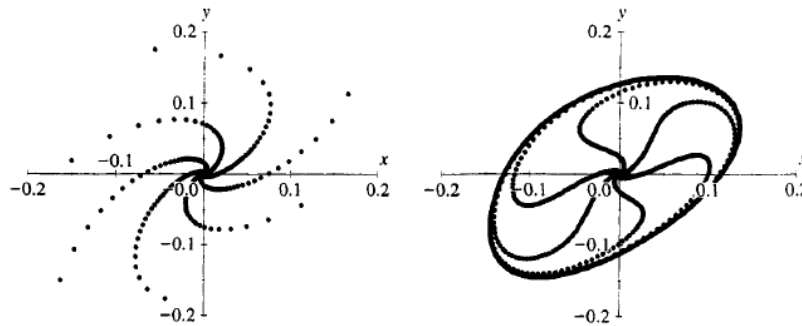


Figure 3.6 Phase plane diagrams for a degree 2 quasi-periodic system; the fixed point at  $(0,0)$  is stable (left), the fixed point at  $(0,0)$  is unstable (right) [67].

Further discussions associated to the stability of a fixed point on the quasi-periodic solution for the SEIG system are presented in Chapter Six.

### 3.5 BIFURCATION DIAGRAMS

A qualitative change that occurs in the dynamics of a system when changing one of its parameters is called a *bifurcation* [67]. A *bifurcation diagram* is a plot that shows the sampled steady-state behaviour of a system over a range of parameter values.

Electrical machines are generally designed to work at certain operating conditions that give specific output characteristics. However, in the presence of significant nonlinearities, the operating mode can be changed qualitatively when input voltage or load changes. Therefore, the study of bifurcation diagrams can be of great importance in such systems.

Two main types of bifurcations take place in nonlinear dynamic systems: smooth and non-smooth bifurcations. The former is characterised by a change in stability status, whereas the latter is characterised by a change in operation as a result of a disturbance of the operating topological sequence [67].

In general, electrical machines exhibit smooth bifurcations. Therefore, only smooth bifurcations are considered in this thesis.

#### 3.5.1 SMOOTH BIFURCATIONS

Smooth bifurcations are broadly classified into four types: pitchfork, saddle-node, period-doubling and Hopf bifurcations.

A pitchfork bifurcation has the characteristic of symmetry [70]. The stable fixed point of a typical pitchfork bifurcation splits into a pair of stable fixed points, whereas the original fixed point becomes unstable (Figure 3.7).

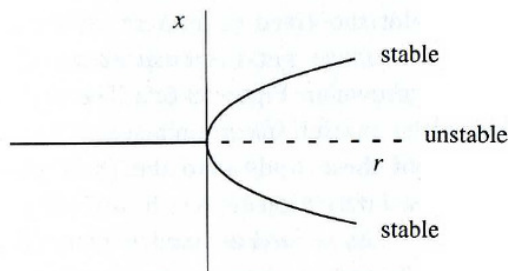


Figure 3.7 A typical characteristics of a pitchfork bifurcation,  $r$  is the bifurcation parameter and  $x$  is the system output.

The saddle-node bifurcation has the basic characteristic of the creation and destruction of fixed points [70]; i.e. the original fixed point disappears and a pair of new fixed points are born (one is stable and the other unstable, Figure 3.8). In discrete-time systems, the saddle-node bifurcation is also known as a fold bifurcation.

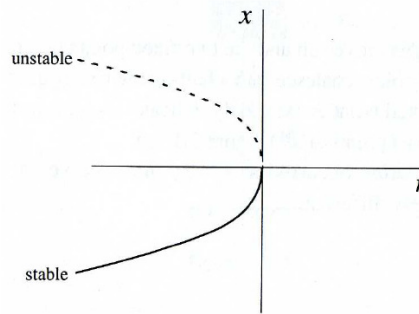


Figure 3.8 A typical characteristics of a saddle-node bifurcation,  $r$  is the bifurcation parameter and  $x$  is the system output.

The phenomenon of a period-one ( $n$ ) orbit transferring to period two ( $n \times 2$ ) solution is known as a *period doubling* bifurcation (Figure 3.9) [67]. In discrete-time systems, the corresponding bifurcation diagram flips between two points, hence the name *flip bifurcation*.

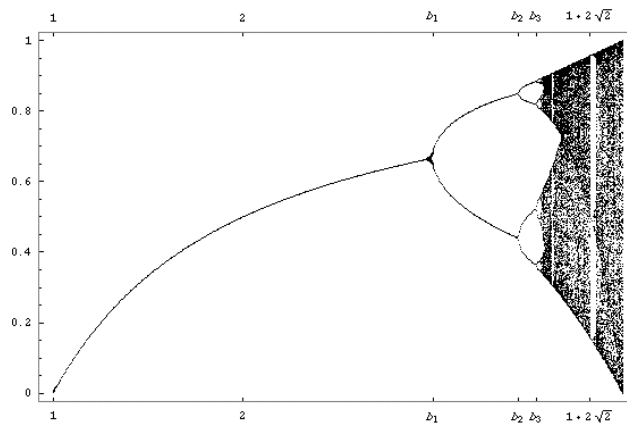


Figure 3.9 A period doubling bifurcation [71]

In continuous systems, if a Poincaré map shows a stable fixed point before the bifurcation which turns into a closed loop after the bifurcation, a Hopf bifurcation is implied. In discrete-time systems, this is called a Neimark bifurcation (Figure 3.10). A *Neimark bifurcation* marks a transition from a period-one orbit to a

quasi-periodic orbit [67]. Mathematically, a limit cycle is born when a pair of complex conjugate eigenvalues passes through the imaginary axis [69]. In this thesis, the concept of the Neimark bifurcation is utilised to analyse the behaviour of the SEIG system.

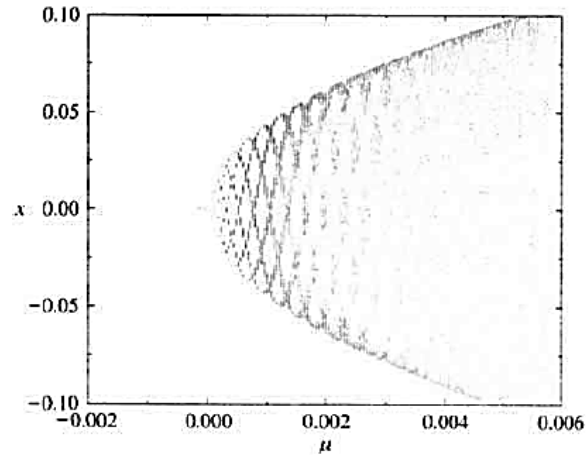


Figure 3.10 A Neimark bifurcation,  $\mu$  is bifurcation parameter and  $x$  is the system output [67].

### 3.5.2 NON-SMOOTH BIFURCATIONS

Non-smooth bifurcations (also called discontinuous bifurcations) imply a change in system topology and can be classified as border collision, border-crossing, grazing and  $C$ -bifurcations. Non-smooth bifurcations are widely applied in the analysis of power electronic switching systems and their stability.

### 3.6 SUMMARY

This chapter provided a brief introduction to nonlinear dynamic systems, Poincaré maps, bifurcation diagrams, limit sets and their stability characteristics. This serves as a general mathematical background required to analyse and study the dynamic behaviour of the SEIG when a variety of load types are connected to its stator terminals.

Differential and difference equations were defined to distinguish the continuous-time and discrete-time dynamic systems.

The Poincaré map technique was presented as a powerful tool to be used to analyse the dynamic behaviour of the SEIG system when feeding variable loads.

Four types of limit sets: Fixed point, periodic solution, quasi-periodic solution and chaos, together with their stability characteristics were presented in this chapter.

Pitchfork, saddle-node, period-doubling and Hopf bifurcations are the four main types of smooth bifurcations and exhibited by electrical machines in general. The SEIG system exhibits a Neimark smooth bifurcation which will be analysed in detail in Chapter Six.

## CHAPTER 4

# MATHEMATICAL MODELLING OF THE SEIG

Numerous methods for the modelling of IMs using Matlab/Simulink software have been investigated by researchers/scientists over the past few decades [54, 58, 60, 65, 72, 73].

The modelling of an IM as a linear electromagnetic device is a conventional method which has been widely used in general applications [74]. The creation of a robust linear transient model is a fundamental process in the construction of a nonlinear SEIG model. Hence, the standard linear induction generator model is introduced in this chapter. This model is composed of four main Simulink blocks: the Stator/Rotor 3-Phase AC Supply blocks, the 3-Phase to  $d$ - $q$  /  $d$ - $q$  to 3-Phase blocks, the Induction Machine block and the Mechanical Dynamics block.

The rest of the chapter is focused on the development of a nonlinear SEIG model using the standard model as a foundation.

The mutual inductances of an IM are generally considered to be constants in a conventional linear model. However, to allow for the effect of saturation (cross-saturation effect), it is necessary to include magnetic nonlinearities into the induction machine model.

The nonlinear model of the machine utilises state space analysis methods to study the dynamic behaviour of the SEIG system. The variable states of the system can be the machine's stator/rotor instantaneous currents or fluxes [14, 54, 58]. Due to the ease of simulation, the machine model using instantaneous currents as state space variables is used in this thesis. This is because the changing inductances of a running machine can be easily implemented in the Simulink SEIG model as variable functions of current.

The three-phase grid power supply of the IM nonlinear model is then replaced by an appropriate three-phase capacitor bank connected across the stator terminals to complete the SEIG system modelling.

An IM generally works with values of magnetic flux density near the saturation level. Hence, the overall system is highly nonlinear and time varying. The dynamic analysis of the system is further complicated by the use of the capacitor bank which provides the reactive power to the generator.

In Chapter Five, the simulation results obtained from the Simulink model developed in this chapter will be compared with the corresponding experimental results. In Chapter Six, the dynamic behaviour of the SEIG feeding an inductive load ( $RL$ ) will be numerically investigated and analysed in detail also using the model developed in this chapter.

## 4.1 STANDARD INDUCTION MACHINE MODEL IGNORING THE CROSS-SATURATION EFFECT

The standard model described in this thesis utilises the state space method, also known as the time domain approach, which provides a convenient, compact and robust way to model and analyse systems with multiple inputs and outputs [75]. This state space model is expressed with respect to the *stator reference frame* (SRF), i.e. its coordinate system is stationary with respect to the stator and does not rotate [76].

Figure 4.1 shows the general layout of the Simulink induction machine model. There are four main parts making up the model: the Stator/Rotor 3-Phase Supply blocks, the 3-Phase to  $d$ - $q$  /  $d$ - $q$  to 3-Phase blocks, the Induction Machine block and the Mechanical Dynamics block.

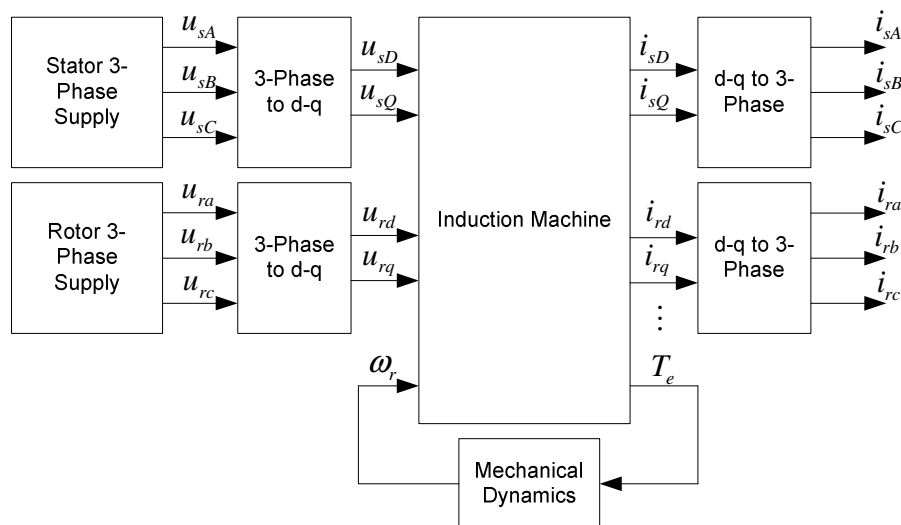


Figure 4.1 The standard induction machine Simulink model overview with multiple inputs and outputs.

The main component of the model is the Induction Machine block in which stator/rotor  $d$ - $q$  axis voltages and rotor shaft speed  $u_{sD}$ ,  $u_{sQ}$ ,  $u_{rd}$ ,  $u_{rq}$  and  $\omega_r$ , respectively, are the multiple inputs, and stator/rotor  $d$ - $q$  axis currents and electrical torque  $i_{sD}$ ,  $i_{sQ}$ ,  $i_{rd}$ ,  $i_{rq}$  and  $T_e$ , respectively, are the multiple outputs of the block.

Due to the unique structure of a cage induction machine, there are no voltages applied to the rotor side. Therefore, the rotor voltage  $u_{rd}$  and  $u_{rq}$  are equated to zero.

#### 4.1.1 THE 3-PHASE AC SUPPLY BLOCK

The internal view of the Stator/Rotor 3-Phase Supply block with three balanced single phase sine waves of amplitude  $\sqrt{2} V_{rms}$  (V) and frequency  $f$  (Hz) as the supply power source to the machine is shown in Appendix A.

#### 4.1.2 THE 3-PHASE TO $d$ - $q$ OR $d$ - $q$ TO 3-PHASE TRANSFORMATION BLOCK

The  $d$ - $q$  axis reference frame representation of the transient state model of the induction machine is used throughout this study. The following mathematical descriptions are applied

$$\begin{cases} u_{sD} = \frac{2}{3}u_{sA} - \frac{1}{3}u_{sB} - \frac{1}{3}u_{sC} \\ u_{sQ} = \frac{1}{\sqrt{3}}u_{sB} - \frac{1}{\sqrt{3}}u_{sC} \end{cases} \quad (4.1)$$

where  $u_{sA}$ ,  $u_{sB}$  and  $u_{sC}$  are the three-phase AC voltage supplies to the stator terminals,  $u_{sD}$  and  $u_{sQ}$  are  $d$ - $q$  axis voltages.

Since the three-phase supply sine wave voltages are given by

$$\begin{cases} u_{sA} = \sqrt{2} V \sin(2\pi ft) \\ u_{sB} = \sqrt{2} V \sin(2\pi ft - \frac{2}{3}\pi) \\ u_{sC} = \sqrt{2} V \sin(2\pi ft + \frac{2}{3}\pi) \end{cases} \quad (4.2)$$

Substituting equation (4.2) into (4.1), the following equations are derived

$$\begin{cases} u_{sD} = \sqrt{2} V \sin(2\pi ft) \\ u_{sQ} = -\sqrt{2} V \cos(2\pi ft) \end{cases} \quad (4.3)$$

The final derived equation (4.3) shows that  $u_{sD}$  and  $u_{sQ}$  are sine and inverse cosine waves with same peak voltage and frequency.

A reverse calculation is applied to transform the output signals from  $d$ - $q$  axis to three-phase ABC presentation. The 3-phase/ $d$ - $q$  transformation is shown in graphical form in Appendix A.

### 4.1.3 THE MAIN INDUCTION MACHINE BLOCK

The stator voltage equations of an induction machine are given by

$$\begin{cases} u_{sA} = R_s i_{sA} + \frac{d\psi_{sA}}{dt} \\ u_{sB} = R_s i_{sB} + \frac{d\psi_{sB}}{dt} \\ u_{sC} = R_s i_{sC} + \frac{d\psi_{sC}}{dt} \end{cases} \quad (4.4)$$

where  $u_{sA}$ ,  $u_{sB}$ ,  $u_{sC}$ ,  $i_{sA}$ ,  $i_{sB}$ ,  $i_{sC}$  and  $\psi_{sA}$ ,  $\psi_{sB}$ ,  $\psi_{sC}$  are the three-phase stator voltages, currents and fluxes, respectively, and  $R_s$  is the stator resistance.

The space vector representation of the three-phase voltages can be derived as given below

$$u_s = \frac{2}{3}(u_{sA} + au_{sB} + a^2u_{sC}) \quad (4.5)$$

where  $u_s$  is stator voltage space vector representing the three-phase supply voltages and  $a$  is equal to  $e^{j\frac{2\pi}{3}}$ . By substitution

$$\frac{2}{3}(u_{sA} + au_{sB} + a^2u_{sC}) = \frac{2}{3}\left((R_s i_{sA} + \frac{d\psi_{sA}}{dt}) + a(R_s i_{sB} + \frac{d\psi_{sB}}{dt}) + a^2(R_s i_{sC} + \frac{d\psi_{sC}}{dt})\right) \quad (4.6)$$

Hence

$$u_s = \frac{2}{3}R_s(i_{sA} + ai_{sB} + a^2i_{sC}) + \frac{2}{3}\left(\frac{d\psi_{sA}}{dt} + a\frac{d\psi_{sB}}{dt} + a^2\frac{d\psi_{sC}}{dt}\right) \quad (4.7)$$

The stator current space vector  $i_s$  is given by

$$i_s = \frac{2}{3}(i_{sA} + ai_{sB} + a^2i_{sC}) \quad (4.8)$$

And

$$\frac{d\psi_s}{dt} = \frac{2}{3} \left( \frac{d\psi_{sA}}{dt} + a \frac{d\psi_{sB}}{dt} + a^2 \frac{d\psi_{sC}}{dt} \right) \quad (4.9)$$

where  $\psi_s$  is the stator flux space vector representing the three-phase stator flux waveforms.

By substituting (4.8) and (4.9) into (4.7), the stator voltage space vector equation is obtained

$$u_s = R_s i_s + \frac{d\psi_s}{dt} \quad (4.10)$$

Similarly, the rotor voltage space vector equation is

$$u_r = R_r i_r + \frac{d\psi_r}{dt} \quad (4.11)$$

The rotor voltage equation can be expressed with respect to the SRF as

$$u_r \cdot e^{j\theta} = R_r i_r \cdot e^{j\theta} + \frac{d(\psi_r \cdot e^{j\theta})}{dt} = R_r i_r \cdot e^{j\theta} + e^{j\theta} \frac{d\psi_r}{dt} - j\omega_r \psi_r \cdot e^{j\theta} \quad (4.12)$$

where  $\theta$  is the angle between the SRF and RRF.

Therefore, the rotor voltage computed in the SRF is given by

$$u_r = R_r i_r + \frac{d\psi_r}{dt} - j\omega_r \psi_r \quad (4.13)$$

The stator and rotor voltage equations with respect to the SRF can now be obtained. equation (4.10) and (4.13) can be expressed in terms of  $d$ - $q$  axis quantities as

$$\begin{cases} u_{sD} + ju_{sQ} = R_s (i_{sD} + ji_{sQ}) + \frac{d(\psi_{sD} + j\psi_{sQ})}{dt} \\ u_{rD} + ju_{rQ} = R_r (i_{rD} + ji_{rQ}) + \frac{d(\psi_{rD} + j\psi_{rQ})}{dt} - j\omega_r (\psi_{rD} + j\psi_{rQ}) \end{cases} \quad (4.14)$$

where the fluxes  $\psi_{sD}$ ,  $\psi_{sQ}$ ,  $\psi_{rd}$  and  $\psi_{rq}$  are given by

$$\begin{cases} \psi_{sD} = L_s i_{sD} + L_m i_{rd} \\ \psi_{sQ} = L_s i_{sQ} + L_m i_{rq} \\ \psi_{rd} = L_r i_{rd} + L_m i_{sD} \\ \psi_{rq} = L_r i_{rq} + L_m i_{sQ} \end{cases} \quad (4.15)$$

Equation (4.15) can now be substituted into (4.14) to give

$$\begin{cases} u_{sD} + j u_{sQ} = R_s i_{sD} + L_s \frac{di_{sD}}{dt} + L_m \frac{di_{rd}}{dt} + j(R_s i_{sQ} + L_s \frac{di_{sQ}}{dt} + L_m \frac{di_{rq}}{dt}) \\ u_{rd} + j u_{rq} = R_r i_{rd} + L_r \frac{di_{rd}}{dt} + L_m \frac{di_{sD}}{dt} + \omega_r (L_r i_{rq} + L_m i_{sQ}) + j(R_r i_{rq} + L_r \frac{di_{rq}}{dt} + L_m \frac{di_{sQ}}{dt} - \omega_r (L_r i_{rd} + L_m i_{sD})) \end{cases} \quad (4.16)$$

The above equations can be rewritten into the following form to give the general induction machine  $d$ - $q$  axis equations

$$\begin{cases} u_{sD} = R_s i_{sD} + L_s \frac{di_{sD}}{dt} + L_m \frac{di_{rd}}{dt} \\ u_{sQ} = R_s i_{sQ} + L_s \frac{di_{sQ}}{dt} + L_m \frac{di_{rq}}{dt} \\ u_{rd} = R_r i_{rd} + L_r \frac{di_{rd}}{dt} + L_m \frac{di_{sD}}{dt} + \omega_r (L_r i_{rq} + L_m i_{sQ}) \\ u_{rq} = R_r i_{rq} + L_r \frac{di_{rq}}{dt} + L_m \frac{di_{sQ}}{dt} - \omega_r (L_r i_{rd} + L_m i_{sD}) \end{cases} \quad (4.17)$$

This equation can be written in matrix form as

$$\begin{bmatrix} u_{sD} \\ u_{sQ} \\ u_{rd} \\ u_{rq} \end{bmatrix} = \begin{bmatrix} R_s + L_s p & 0 & L_m p & 0 \\ 0 & R_s + L_s p & 0 & L_m p \\ L_m p & \omega_r L_m & R_r + L_r p & \omega_r L_r \\ -\omega_r L_m & L_m p & -\omega_r L_r & R_r + L_r p \end{bmatrix} \begin{bmatrix} i_{sD} \\ i_{sQ} \\ i_{rd} \\ i_{rq} \end{bmatrix} \quad (4.18)$$

where the symbol  $p$  is used to denote differentiation with respect to time.

The above machine mathematical descriptions are presented as four subsystems of the main Simulink 'Induction Machine' block in Appendix A.

#### 4.1.4 THE MECHANICAL DYNAMICS SYSTEM BLOCK

The electrical torque expression can be expressed as

$$T_e = \psi_{rq} i_{rd} - \psi_{rd} i_{rq} \quad (4.19)$$

For a 3-phase,  $P$ -pole machine, the electrical torque with respect to the SRF is given by

$$T_e = \frac{3}{2} \frac{P}{2} (\psi_{rq} i_{rd} - \psi_{rd} i_{rq}) \quad (4.20)$$

The electrical torque Simulink block ' $T_e$ ' is shown in Appendix A.

The total mechanical torque developed at the rotor shaft is mathematically described as

$$T = T_e - T_{Load} - T_{Friction} = J \frac{d\omega_r}{dt} \quad (4.21)$$

where  $T_e$  is the electrical torque generated by the machine,  $T_{Load}$  is the load torque,  $T_{Friction}$  is the torque produced by friction,  $J$  is the moment of inertia and  $\omega_r$  is the rotor speed.

The Simulink presentation of the mechanical dynamics system is shown Appendix A.

## 4.2 INDUCTION MACHINE MODEL INCLUDING THE CROSS-SATURATION EFFECT

An analysis of the IM system including a representation of magnetic nonlinearities (the cross-saturation phenomena) is presented in this section. The cross-saturation effect in an induction machine has been studied by a number of researchers in the past few decades [11, 54, 55]. It refers to two machine windings with their magnetic axes in space quadrature exhibiting specific magnetic interactions, due to saturation of the main flux paths [11].

The mathematical descriptions of a saturated IM with consideration of the cross-saturation effect are given in the following subsections.

### 4.2.1 MATHEMATICAL REPRESENTATION OF CROSS-SATURATION

The IM model developed above has four states (the stator and rotor  $d$ - $q$  axis currents) and is linear time varying and rotor speed dependent. The general matrix equation of an IM expressed in the SRF is given by (4.18), which can be rewritten in vector form as

$$\mathbf{U} = \mathbf{R}\mathbf{I} + \mathbf{L}_1 \frac{d\mathbf{I}}{dt} + \omega_r \mathbf{L}_2 \quad (4.22)$$

where  $\mathbf{U}$  and  $\mathbf{I}$  are the vectors representing the stator and rotor voltages and currents, respectively,  $\mathbf{R}$  is the resistance matrix,  $\omega_r$  is the rotor speed and  $\mathbf{L}_1, \mathbf{L}_2$  are inductance matrices given by

$$\mathbf{U} = [u_{sD} \ u_{sQ} \ u_{rD} \ u_{rQ}]^T, \quad \mathbf{I} = [i_{sD} \ i_{sQ} \ i_{rD} \ i_{rQ}]^T, \quad \mathbf{R} = \text{diag}(R_s, R_s, R_r, R_r),$$

$$\mathbf{L}_1 = \begin{bmatrix} L_s & 0 & L_m & 0 \\ 0 & L_s & 0 & L_m \\ L_m & 0 & L_r & 0 \\ 0 & L_m & 0 & L_r \end{bmatrix}, \quad \mathbf{L}_2 = \begin{bmatrix} 0 & 0 & 0 & 0 \\ 0 & 0 & 0 & 0 \\ 0 & L_m & 0 & L_r \\ -L_m & 0 & -L_r & 0 \end{bmatrix}$$

To model the nonlinearity of the dynamic system, the elements of the inductance matrix  $\mathbf{L}_1$  has to change to become functions of the magnetising current instead of being constants. Cross-saturation is allowed for by introducing new elements into the inductance matrix  $\mathbf{L}_1$  of the non-saturated

machine model, namely the saturated magnetising inductance and its derivative. The linear matrix  $\mathbf{L}_1$  is then transformed into the following nonlinear matrix ( $\mathbf{L}_3$ )

$$\mathbf{L}_3 = \begin{bmatrix} L_{sd} & L_{dq} & L_{md} & L_{dq} \\ L_{dq} & L_{sq} & L_{dq} & L_{mq} \\ L_{md} & L_{dq} & L_{rd} & L_{dq} \\ L_{dq} & L_{mq} & L_{dq} & L_{rq} \end{bmatrix}$$

**Note:** Only the effect of the main flux saturation is incorporated in the analysis.

The machine equation combination with consideration to the cross-saturation effect can then be written in the form ( $\mathbf{U} = \mathbf{R}\mathbf{I} + \mathbf{L}_3 \frac{d\mathbf{I}}{dt} + \omega_r \mathbf{L}_2$ ) [11]

$$\begin{bmatrix} u_{sD} \\ u_{sQ} \\ u_{rd} \\ u_{rq} \end{bmatrix} = \begin{bmatrix} R_s & 0 & 0 & 0 \\ 0 & R_s & 0 & 0 \\ 0 & 0 & R_r & 0 \\ 0 & 0 & 0 & R_r \end{bmatrix} \begin{bmatrix} i_{sD} \\ i_{sQ} \\ i_{rd} \\ i_{rq} \end{bmatrix} + \begin{bmatrix} L_{sd} & L_{dq} & L_{md} & L_{dq} \\ L_{dq} & L_{sq} & L_{dq} & L_{mq} \\ L_{md} & L_{dq} & L_{rd} & L_{dq} \\ L_{dq} & L_{mq} & L_{dq} & L_{rq} \end{bmatrix} \begin{bmatrix} \dot{i}_{sD} \\ \dot{i}_{sQ} \\ \dot{i}_{rd} \\ \dot{i}_{rq} \end{bmatrix} + \omega_r \begin{bmatrix} 0 & 0 & 0 & 0 \\ 0 & 0 & 0 & 0 \\ 0 & L_m & 0 & L_r \\ -L_m & 0 & -L_r & 0 \end{bmatrix} \begin{bmatrix} i_{sD} \\ i_{sQ} \\ i_{rd} \\ i_{rq} \end{bmatrix} \quad (4.23)$$

where  $L_m$  denotes the saturated inductance (magnetising inductance) given by

$$L_m = \frac{|\bar{\psi}_m|}{|\bar{i}_m|} \quad \text{and} \quad L \text{ is the dynamic inductance given by } L = d|\bar{\psi}_m|/d|\bar{i}_m|.$$

Values of the magnetising and the dynamic inductance for a 1.5 kW machine are shown in Figure 4.2 as functions of current [11].

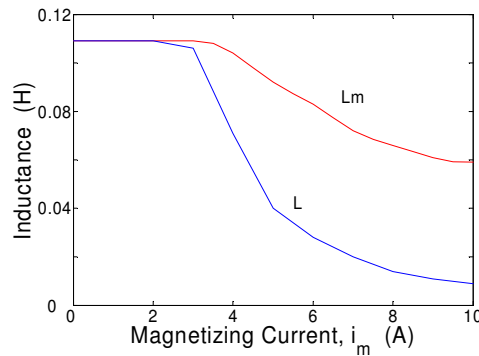


Figure 4.2 Saturated magnetising inductance  $L_m$  and dynamic inductance  $L$  [11].

The cross-saturation coupling between all axes in space quadrature is represented by  $L_{dq}$  (the cross-saturation inductance) given by

$$L_{dq} = \frac{i_{md}i_{mq}}{i_m} \times \frac{dL_m}{d|i_m|} \quad (4.24)$$

The derivative of the mutual flux  $d|\bar{\psi}_m|$  is given by

$$d|\bar{\psi}_m| = dL_m \times |i_m| + d|i_m| \times L_m \quad (4.25)$$

The above equation can be rewritten as

$$\frac{d|\bar{\psi}_m|}{d|i_m|} - \frac{d|i_m| \times L_m}{d|i_m|} = \frac{dL_m \times |i_m|}{d|i_m|} \quad (4.26)$$

The Dynamic inductance is given by  $L = \frac{d|\bar{\psi}_m|}{d|i_m|}$ , therefore

$$|i_m| \frac{dL_m}{d|i_m|} = \frac{d|\bar{\psi}_m|}{d|i_m|} - L_m = L - L_m \quad (4.27)$$

This equation can be rewritten as

$$\frac{dL_m}{d|i_m|} = \frac{L - L_m}{|i_m|} \quad (4.28)$$

Substituting (4.28) into (4.24), yields the following equation

$$L_{dq} = \frac{i_{md}i_{mq}}{i_m} \times \frac{L - L_m}{|i_m|} \quad (4.29)$$

The direct and quadrature axis magnetising currents are given by

$$i_{md} = i_{sD} + i_{rd}; \quad i_{mq} = i_{sQ} + i_{rq} \quad (4.30)$$

The total magnetising current  $i_m$  is given by

$$i_m = (i_{md}^2 + i_{mq}^2)^{\frac{1}{2}} \quad (4.31)$$

The direct and quadrature axis saturated inductances are calculated as

$$L_{md} = L_m + \frac{i_{md}}{i_{mq}} L_{dq}; \quad L_{mq} = L_m + \frac{i_{mq}}{i_{md}} L_{dq} \quad (4.32)$$

When the system is operating under linear magnetic condition with no saturation of the flux paths, the machine's cross-saturation inductance is

$$L_{dq} = 0, \quad L_{md} = L_{mq} = L_m \quad \text{and}$$

$$L_{sd} = L_{sl} + L_{md}; \quad L_{sq} = L_{sl} + L_{mq} \quad (4.33)$$

$$L_{rd} = L_{rl} + L_{md}; \quad L_{rq} = L_{rl} + L_{mq} \quad (4.34)$$

where,  $L_{sl}$  and  $L_{rl}$  are the unsaturated stator and rotor leakage inductances (assumed to be constant).

Because of saturation,  $L_{sd} = L_{sq}$ ;  $L_{rd} = L_{rq}$  and the rotor inductance is

$$L_r = L_{rl} + L_m \quad (4.35)$$

#### 4.2.2 TORQUE EQUATIONS

The rotor flux linkages (4.15) are given by

$$\psi_{rq} = L_r i_{rq} + L_m i_{sQ}; \quad \psi_{rd} = L_r i_{rd} + L_m i_{sD} \quad (4.36)$$

The above equations can be utilised to re-write the torque equation (4.20) as

$$\begin{aligned} T_e &= \frac{3p}{4} (L_r i_{rq} i_{rd} + L_m i_{sQ} i_{rd} - L_r i_{rd} i_{rq} - L_m i_{sD} i_{rq}) \\ &= \frac{3p}{4} L_m (i_{sQ} i_{rd} - i_{sD} i_{rq}) \end{aligned} \quad (4.37)$$

Apart from the effects of the main flux saturation of an IM is discussed within this chapter, the effects of the saturation of the leakage flux paths are also presented to the reader in Appendix B. These are important under certain operating conditions such as when large inrush currents occur, but are not included in the main analysis of the SEIG steady-state response [58].

### 4.3 SELF-EXCITED INDUCTION GENERATOR MODEL

The SEIG operates just like any other induction machine, except for the fact that its stator terminals are connected (in parallel) to a three-phase self-excitation capacitor bank in the absence of the normal three-phase supply voltages. These machines are ideal for electricity generation in standalone variable speed hydraulic turbine or wind turbine applications, where there is no available grid connection.

It is possible to create and build a SEIG Simulink model based on the nonlinear model created in the previous section.

#### 4.3.1 THE MATHEMATICAL DESCRIPTIONS

The grid supply in the previous induction machine model is now replaced with three-phase capacitors connected in parallel with the stator windings as shown in Figure 4.3, where,  $i_{sD}i_{sQ}$  and  $i_{rd}i_{rq}$  refer to the stator and rotor  $d$ - $q$  axis currents, respectively. The state space nonlinear equations forming the basis of the nonlinear model of the machine are modified as follows to represent the SEIG.

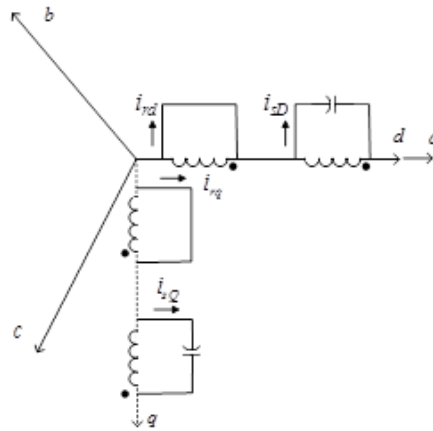


Figure 4.3 The SEIG  $d$ - $q$  equivalent circuit.

The equivalent circuit of Figure 4.3 clearly shows that the rotor side state space equations are not changed, whereas the stator voltage equations need to be changed to represent the dynamics of the capacitor bank connected to the stator terminals.

Equation (4.23) can be rewritten as [12]

$$\begin{bmatrix} u_{CD} \\ u_{CQ} \\ 0 \\ 0 \end{bmatrix} = \begin{bmatrix} R_s & 0 & 0 & 0 \\ 0 & R_s & 0 & 0 \\ 0 & 0 & R_r & 0 \\ 0 & 0 & 0 & R_r \end{bmatrix} \begin{bmatrix} i_{sD} \\ i_{sQ} \\ i_{rd} \\ i_{rq} \end{bmatrix} + \begin{bmatrix} L_{sd} & L_{dq} & L_{md} & L_{dq} \\ L_{dq} & L_{sq} & L_{dq} & L_{mq} \\ L_{md} & L_{dq} & L_{rd} & L_{dq} \\ L_{dq} & L_{mq} & L_{dq} & L_{rq} \end{bmatrix} \begin{bmatrix} \dot{i}_{sD} \\ \dot{i}_{sQ} \\ \dot{i}_{rd} \\ \dot{i}_{rq} \end{bmatrix} + \omega_r \begin{bmatrix} 0 & 0 & 0 & 0 \\ 0 & 0 & 0 & 0 \\ 0 & L_m & 0 & L_r \\ -L_m & 0 & -L_r & 0 \end{bmatrix} \begin{bmatrix} i_{sD} \\ i_{sQ} \\ i_{rd} \\ i_{rq} \end{bmatrix} \quad (4.38)$$

The above equation shows that the cross-saturation part (on the right hand side of the equation) has not been changed, whereas the  $d$ - $q$  axis stator voltages (on the left hand side of the equation) have been changed to allow for the connection of the capacitor bank.

The capacitor bank voltages  $u_{CD}$  and  $u_{CQ}$  will be different depend on the type of load the SEIG is feeding. Three types of load conditions are considered in this analysis: no-load, a purely resistive load ( $R$ ) and an inductive load ( $RL$ ) as detailed in the following subsections.

#### a) State Equations of the SEIG under No-load Conditions

The stator direct axis equivalent circuit with no-load is shown in Figure 4.4.

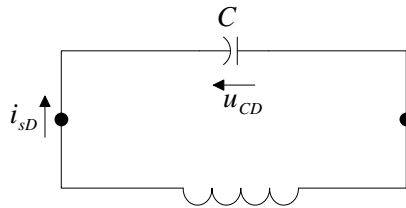


Figure 4.4 Stator direct axis equivalent circuit with self-excitation capacitors without load;  $i_{sD}$  is the stator direct current.

The capacitors direct axis voltage equation is

$$u_{CD} = -u_{sD} = -\frac{1}{C} \int i_{sD} dt \quad (4.39)$$

And the capacitors quadrature voltage equation is

$$u_{CQ} = -u_{sQ} = -\frac{1}{C} \int i_{sQ} dt \quad (4.40)$$

b) State Equations of the SEIG Operating with a Resistive Load

The direct axis equivalent circuit representing the connection of the capacitor bank and the resistive load is presented in Figure 4.5.

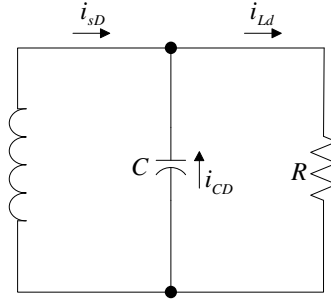


Figure 4.5 Stator direct axis equivalent circuit with self-excitation capacitors and resistive load  $R$ ;  $i_{sD}$ ,  $i_{CD}$  and  $i_{Ld}$  are the stator, capacitor and load direct currents, respectively.

Figure 4.5 is represented by the following mathematical equations

$$u_{CD} = -u_{Ld} = -i_{Ld}R \quad (4.41)$$

The capacitor direct current is given by

$$i_{CD} = -C \frac{du_{Ld}}{dt} = -RC \frac{di_{Ld}}{dt} \quad (4.42)$$

$$i_{sD} = -i_{CD} + i_{Ld} = RC \frac{di_{Ld}}{dt} + i_{Ld} \quad (4.43)$$

Using the same methodology, the equation for  $u_{CQ}$ ,  $i_{sQ}$  can also be solved and computed.

$$u_{CQ} = -u_{Lq} = -i_{Lq}R \quad (4.44)$$

$$i_{sQ} = RC \frac{di_{Lq}}{dt} + i_{Lq} \quad (4.45)$$

### c) State Equations of the SEIG Operating with an Inductive Load

The direct axis equivalent circuit of the SEIG with an inductive load ( $RL$ ) connected to the stator terminals is shown in Figure 4.6.

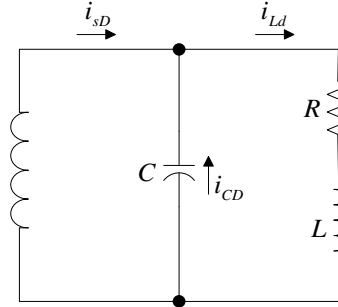


Figure 4.6 Stator direct axis equivalent circuit with self-excitation capacitors and inductive load ( $RL$ );  $i_{sD}$ ,  $i_{CD}$  and  $i_{Ld}$  are the stator, capacitor and load direct currents, respectively.

The equations for the above equivalent circuit are as follows

$$u_{CD} = -u_{Ld} = -Ri_{Ld} - L \frac{di_{Ld}}{dt} \quad (4.46)$$

$$i_{CD} = -C \frac{du_{Ld}}{dt} = -RC \frac{di_{Ld}}{dt} - LC \frac{d^2 i_{Ld}}{dt^2} \quad (4.47)$$

$$i_{sD} = -i_{CD} + i_{Ld} \quad (4.48)$$

$$i_{sD} = RC \frac{di_{Ld}}{dt} + LC \frac{d^2 i_{Ld}}{dt^2} + i_{Ld} \quad (4.49)$$

Therefore, the quadrature voltage and current equations are

$$u_{CQ} = -u_{Lq} = -Ri_{Lq} - L \frac{di_{Lq}}{dt} \quad (4.50)$$

$$i_{sQ} = RC \frac{di_{Lq}}{dt} + LC \frac{d^2 i_{Lq}}{dt^2} + i_{Lq} \quad (4.51)$$

### 4.3.2 SIMULATION RESULTS

The mathematical descriptions of the SEIG system under variable load conditions have been studied in the previous section. The voltage equations of the SEIG model can now be solved and the simulation results are to be presented in detail in this section.

The parameters of a  $1.5\text{ kW}$ ,  $50\text{ Hz}$ , 4-pole,  $220/380\text{ V}$  and  $7/4\text{ A}$  cage induction machine with a three-phase self-excitation capacitor bank ( $135\text{ }\mu\text{F}$  per phase) are used in this section to test the SEIG model and verify its accuracy. The machine equivalent circuit parameters (referred to the stator) are as follows: stator and rotor resistances are  $0.6\text{ }\Omega$  and  $0.83\text{ }\Omega$ , respectively, and the stator and rotor leakage reactances are both equal to  $1.8\text{ }\Omega$ . The machine magnetising reactance is directly obtained from Figure 4.2. The prime mover of the generator is presented by a DC machine rotating at a constant speed of  $1500\text{ rev/min}$ . The parameters are obtained from a well-known publication, to allow for easy comparison and hence the verification of the simulation results [14].

The following  $d$ -axis equivalent circuit is used to model the effects of the various loads applied to the IG stator terminals, (a similar equivalent circuit is used for  $q$ -axis quantities).

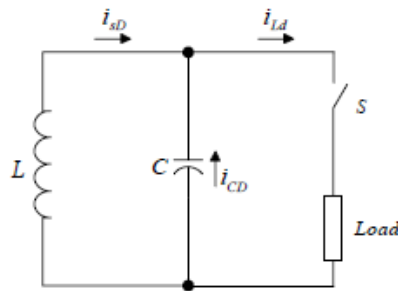


Figure 4.7 Stator direct axis equivalent circuit with various load types.

*a) The Initial Self-excitation Process of the Induction Machine; No-load*

As the machine is working under no-load, the switch S in Figure 4.7 remains open and the  $d$ - $q$  capacitor's voltages are as shown in Equations (4.39) and (4.40). Initial conditions for the capacitor bank voltage and rotor flux must be set to appropriately low values to ensure the success of the self-start process. The general self-excitation process of the generator during the initial voltage build-up stage is observed in Figure 4.8 and Figure 4.9. The stator phase voltage starts building up slowly and reaches a steady-state value while the magnetisation current starts from zero rising to a stable steady-state value. A stable output voltage could only be obtained once the machine's core is saturated. Another physical explanation of the starting process of the SEIG is that the residual magnetism presented in the core (the rotor) induces a small voltage across the stator windings and self-excitation capacitors once the rotor is driven by the prime mover. This produces a delayed current which in turn produces an increased voltage and consequently an increased capacitor current. This phenomenon goes on until saturation of the magnetic flux paths. The simulation results shown in Figure 4.8 agree well with experimental results presented in [14].

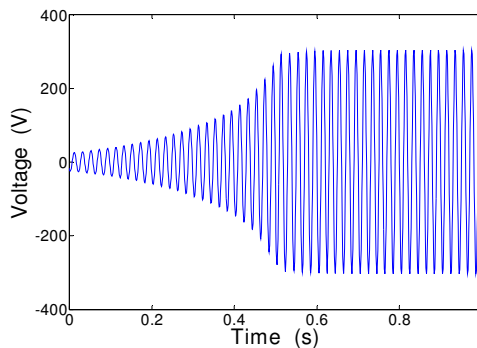


Figure 4.8 Stator line-to-line voltage builds up at no-load.

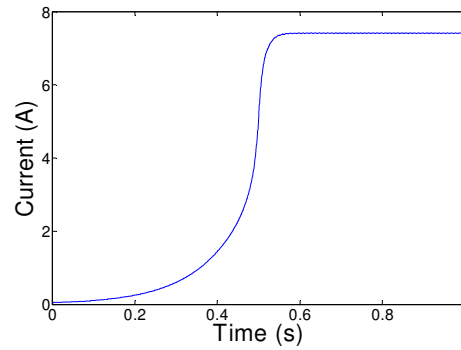


Figure 4.9 Magnetising current during initial self-excitation at no-load.

*b) The SEIG Operating with a Resistive Load*

Here the SEIG is initially running under no-load condition as previously discussed and a resistive load of  $27 \Omega$  per phase is applied to the stator terminals at 1 s. It is clear from Figure 4.10 that there is a drop in output voltage when the resistive load is applied at 1 s, as the system has to supply power to the extra load.

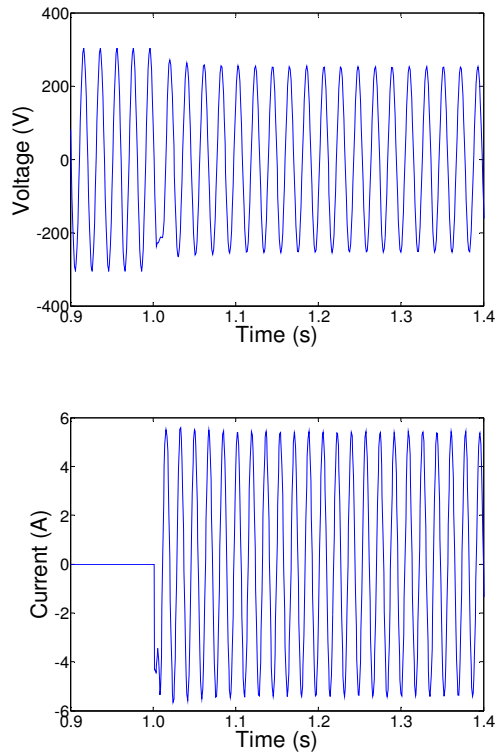


Figure 4.10 Computed stator line-to-line voltage (top) and load current (bottom) when applying a  $27 \Omega$  load at 1 s.

It is shown from the above voltage and current waveforms that (regardless of the voltage drop) the solution curve in state space is a closed period-one orbit. In practical applications, a second capacitor bank connected in series with the resistive load may be used to decrease the resulting voltage drop. However, from the dynamic point of view, the behaviour of the system remains qualitatively the same (i.e. the system exhibits a similar stable period-one orbit). Therefore, this configuration is not studied further in this thesis. The voltage and current waveforms also agree very well with experimental results shown in [14].

The characteristic of the magnetising current is plotted in Figure 4.11. Clearly, the application of the  $27\ \Omega$  load greatly reduces the magnetising current and hence the magnetising flux of the machine. This reduction in flux is the reason for the drop in the SEIG stator terminal voltage.

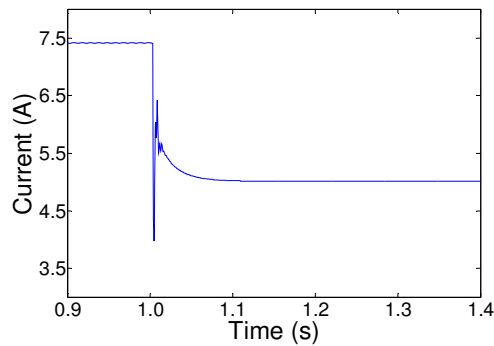


Figure 4.11 Magnetising current when applying a  $27\ \Omega$  load at 1 s.

#### **4.4 SUMMARY**

The computer modelling of the induction generator as a linear electromagnetic device was introduced in this chapter. This standard machine model is the foundation for further study and investigation of the nonlinear behaviour of the SEIG system.

A model of the machine with consideration of the cross-saturation nonlinear effect was then derived by modifying the standard machine model [11]. A current based implementation of the state space model of the machine (with currents as state space variables) was used in this thesis because of its ease of simulation in Simulink. The SEIG nonlinear model was finally created by taking into account the stator and rotor voltages when operating as a standalone device feeding different types of load with the self-excitation capacitor connection in parallel with the stator terminals. The model was verified by comparison with experimental results presented in a well-known publication [14].

The SEIG exhibits period-one linear waveforms when operating at no-load and when feeding a purely resistive load, as shown in the simulation results generated from the proposed nonlinear model. The waveforms also show how the magnetising current and flux drop when a resistive load is connected to the stator terminals which in turn causes a drop in the stator terminal voltage.

# CHAPTER 5

## EXPERIMENTAL INVESTIGATION

A number of experimental tests are presented in this chapter using a laboratory 1.1 kW, 220~240 V, 4.4 A, 50 Hz, 2-pole induction machine operating as a SEIG under a variety of load conditions. The purpose of these tests is firstly to validate the numerical SEIG model developed earlier in Chapter Four and secondly to demonstrate the nonlinear behaviour of the system when feeding a variable inductive load, moving from a stable period-one linear orbit to a nonlinear orbit as a system parameter is varied.

The parameters of the equivalent circuit of the induction machine are as follows: Stator reactance  $X_{sta} = j7.425 \Omega$ , stator resistance  $R_{sta} = 6.65 \Omega$ , rotor reactance  $X_{rot} = j7.425 \Omega$ , rotor resistance  $R_{rot} = 7.64 \Omega$ , magnetising reactance  $X_m = j171.54 \Omega$  and core resistance  $R_c = 25.88 \Omega$ . Details of no-load and blocked rotor tests carried out to determine the induction machine parameters are shown in Appendix C.

The prime mover in the test apparatus is a 1.5 kW DC machine controlled by a Mentor digital DC drive. In all tests, the DC machine is used to rotate the induction machine at 3000 rpm before the three-phase self-excitation capacitor bank is connected to the stator terminals of the machine. The load is then switched on after the self-excitation process has been completed. The results from these tests are logged and used to demonstrate the performance characteristics of the SEIG. The laboratory results are compared to simulation results for each test to validate the SEIG Simulink numerical model.

In this chapter, the SEIG experimental setup is described and the stator current waveforms captured from each test are compared with those generated from the Simulink model. Tests are performed for the SEIG operating under no-load conditions and also when feeding a purely resistive load ( $R$ ) and an inductive

load ( $RL$ ) conditions. Examples of linear and nonlinear orbits are shown in this chapter.

## 5.1 TEST SETUP

The devices used in these tests are listed in detail in Appendix D. An overview of the system is given in Figure 5.1. The tests carried out to study the dynamic behaviour of the SEIG under the different load conditions are listed in Table 5.1. The equipment was mounted on a bench to form the SEIG test rig. Rotational devices (e.g. the rotor shaft, the DC rotor and the AC rotor) and any high voltage equipment were housed within suitable metal enclosures for safety purposes.

### 5.1.1 SYSTEM OVERVIEW

An overview of the SEIG test rig is given in Figure 5.1. The motor drive controls the speed of the DC motor which provides the mechanical input to the IG. The generator is the key component of the rig. It converts the mechanical input power at the rotating shaft to three-phase electrical power at the stator terminals. A self-excitation capacitor bank ( $C$ ) provides the reactive power to both the machine and the load during and after the self-excitation process. A variable load (purely resistive  $R$  or inductive  $RL$ ) is connected to the stator terminals in parallel with the self-excitation capacitors.

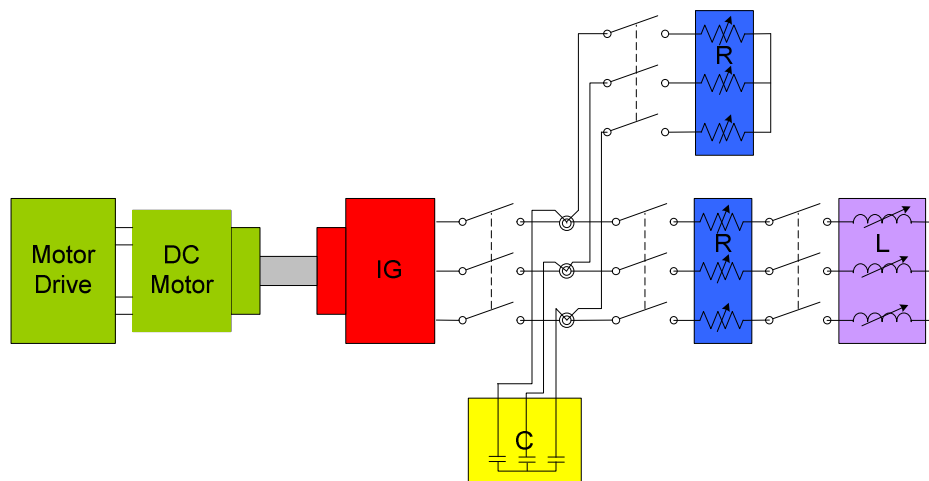


Figure 5.1 Outline of the SEIG test rig.

The tests carried out by the author are listed in Table 5.1. The tests are classified into four groups: magnetising curve test, self-excitation (no-load) tests, resistive load ( $R$ ) tests and inductive load ( $RL$ ) tests. The values of the resistive load, inductive load and the self-excitation capacitance for each test are also listed in Table 5.1.

Table 5.1 List of tests carried out.

Test Group	Test No.	Load Resistance ( $\Omega/phase$ )	Load Inductance ( $mH/phase$ )	Self-excitation capacitance ( $\mu F/phase$ )
Magnetising curve (Section 5.2)	n/a	n/a	n/a	n/a
Initial self-excitation process (No-load tests, Section 5.3)	Test 1	n/a	n/a	45
	Test 2	n/a	n/a	60
	Test 3	n/a	n/a	90
Purely resistive load ( $R$ ) (Section 5.4)	Test 4	60	n/a	45
	Test 5	50	n/a	45
	Test 6	40	n/a	45
Inductive load ( $RL$ ) (Section 5.5)	Test 7	90	1.7	45
	Test 8	60	60	45
	Test 9	40	11	45

## 5.2 MAGNETISING CURVE TEST

When the machine runs at its synchronous speed, the rotor and load parameters of the equivalent circuit can be ignored as the slip is zero. Therefore, the magnetising curve of the machine (measured at 50 Hz) can be obtained by varying the supply voltage and measuring the stator current. The recorded magnetising current when varying the supply voltage is shown in Figure 5.2.

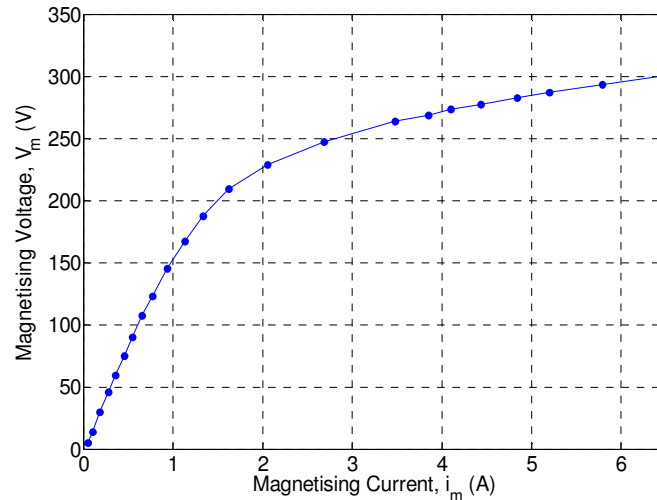


Figure 5.2 The 1.1 kW IM magnetising characteristics.

The measured points on the saturation curve were used to generate a continuous curve (shown in Figure 5.2) with a Spline Function curve-fitting method from Matlab. The saturation curve is represented by the line voltage as a function of the line current (voltage and current are shown in rms values). This figure was obtained by comparing the measured voltage and current waveforms at a number of points.

In order to obtain a more accurate representation of the instantaneous relationship between current and flux, measured rms values were first converted to peak values. This is achieved by multiplying the measured rms voltages and currents by  $\sqrt{2}$  in the linear region of the magnetising curve. In the saturation region where the current waveforms are no longer sinusoidal, measured voltages are multiplied by  $\sqrt{2}$  and measured currents by 2 [77].

The above saturation curve is used to compute the magnetising inductance

$$L_m = \frac{|\bar{\Psi}_m|}{|\bar{i}_m|} = \sqrt{\frac{V_m^2/i_m^2 - R_c^2}{2\pi f}} \quad (\text{where } R_c \text{ is the core resistance})$$

and the dynamic inductance  $L = \frac{d|\bar{\Psi}_m|}{d|\bar{i}_m|}$ . In Figure 5.3 and Figure 5.4, the inductance  $L_m$  and the

quantity  $|\bar{i}_m| \left( \frac{dL_m}{d|\bar{i}_m|} \right)$  are plotted against the current  $|\bar{i}_m|$ . As discussed in Chapter

Four, the following equation can be solved  $|\bar{i}_m| \left( \frac{dL_m}{d|\bar{i}_m|} \right) = \frac{d|\bar{\Psi}_m|}{d|\bar{i}_m|} - L_m = L - L_m$  to obtain the dynamic inductance curve shown in Figure 5.5 [11].

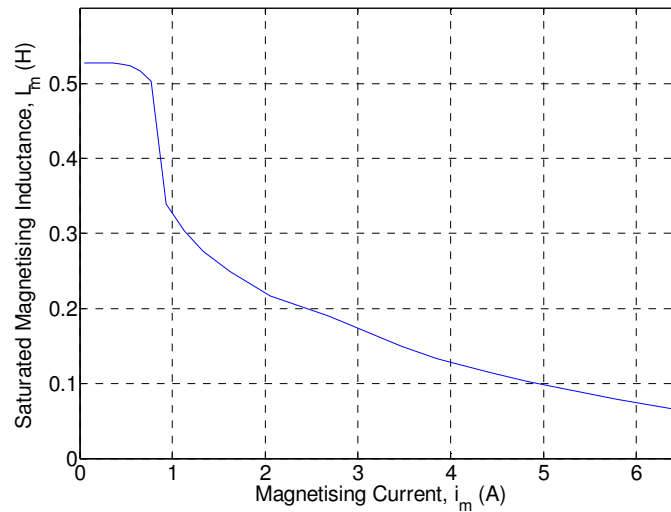


Figure 5.3 Magnetising inductance versus magnetising current.

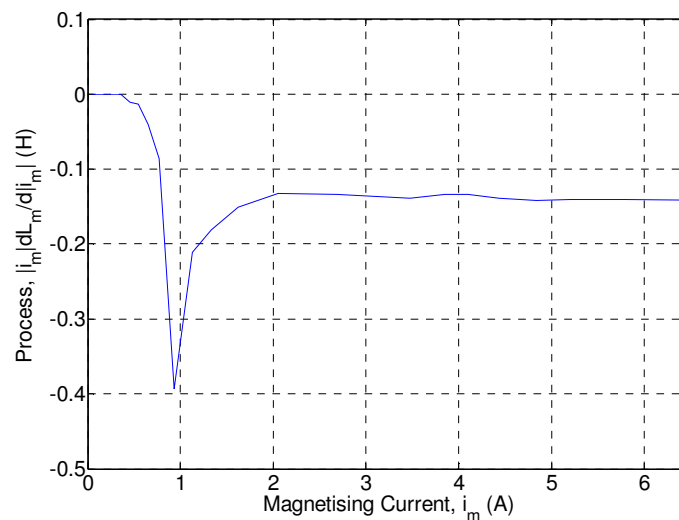


Figure 5.4  $|i_m| \frac{dL_m}{d|i_m|}$  versus magnetising current.

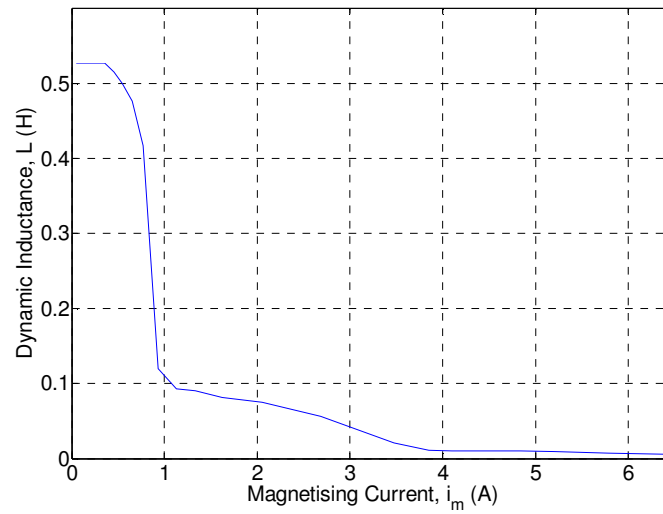


Figure 5.5 Dynamic inductance versus magnetising current.

The above magnetising curves are crucial for modelling the nonlinear behaviour of the SEIG. The magnetising and the dynamic inductance curves are utilised in the nonlinear simulation model of the SEIG with a method of look-up table from Matlab.

### 5.3 SEIG NO-LOAD TESTS

The SEIG is firstly examined under no-load condition when different values of self-excitation capacitors are applied to the stator terminals. The results recorded from the tests are compared with the results generated from the SEIG Simulink model under the same conditions.

#### 5.3.1 TEST 1; $C = 45 \mu F$

The induction generator's shaft is initially rotated at a steady speed of 3000 *rpm* before the three-phase, star connected self-excitation capacitor bank ( $45 \mu F$  per phase) is applied to the stator terminals. The speed of rotation is then altered until a steady-state rms stator voltage of 240 *V* (rated voltage) was obtained. The tachometer recorded a rotor steady-state shaft speed of 3180 *rpm* at this point. Experimental and simulated stator steady-state line current waveforms are shown in Figure 5.6 and Figure 5.7, respectively. Both waveforms present a stable period-one orbit with a frequency of 53.8 *Hz*.

The test results show that the induction generator is successfully self-started when a three-phase capacitor bank ( $45 \mu F$  per phase) are connected to the stator terminals. A measured stable current of 2.2 *A* (Figure 5.6) matches well with the rms value of the waveform (2.25 *A*) shown in Figure 5.7.

Small differences exist between the three current waveforms shown in Figure 5.6, this may be caused by imbalance in three-phase self-excitation capacitors, induction machine or power supply.

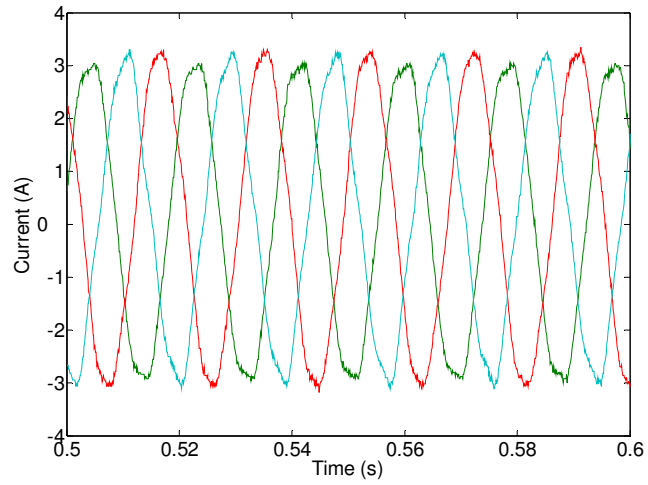


Figure 5.6 Test 1 – Measured stator line current waveforms at no-load with  $C = 45 \mu F$  per phase – Period-one waveforms.

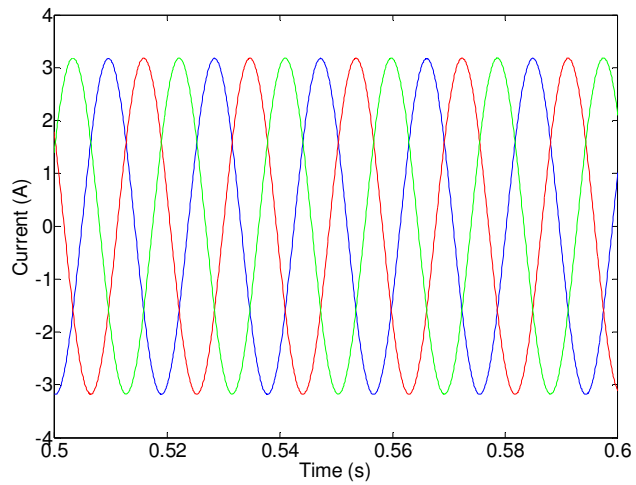


Figure 5.7 Test 1 – Simulated stator line current waveforms at no-load with  $C = 45 \mu F$  per phase – Period-one waveforms.

### 5.3.2 TEST 2; $C = 60 \mu F$

With a self-excitation capacitor bank of  $60 \mu F$  per phase connected across the stator terminals, the recorded rotor steady-state shaft speed of  $2994 \text{ rpm}$  after the self-excitation process when the stator voltage reaches rated value at  $240 \text{ V}$ . The measured and simulated steady-state stator current waveforms are shown in Figure 5.8 and Figure 5.9, respectively. Both waveforms are period-one orbits with a frequency and rms current at round  $49.6 \text{ Hz}$  and  $2.5 \text{ A}$ .

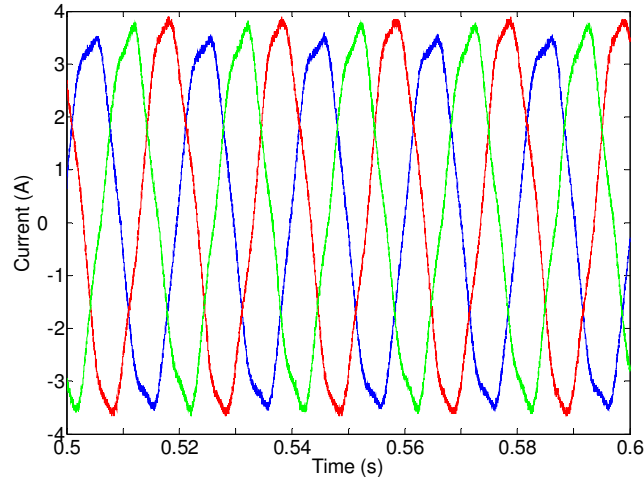


Figure 5.8 Test 2 – Measured stator line current waveforms at no-load with  $C = 60 \mu F$  per phase – Period-one waveforms.

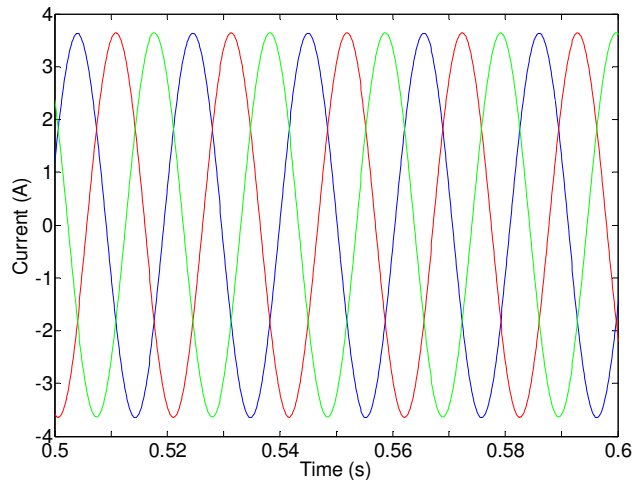


Figure 5.9 Test 2 – Simulated stator line current waveforms at no-load with  $C = 60 \mu F$  per phase – Period-one waveforms.

### 5.3.3 TEST 3; $C = 90 \mu F$

The induction generator is rotated at 3000 *rpm* by the DC motor as the prime mover, and the self-excitation capacitor bank ( $90 \mu F$  per phase star connected) is connected to the stator terminals, the tachometer recorded rotor steady-state shaft speed is equal to 2771 *rpm* after the self-excitation process when the stator voltage reaches 240 *V*. The measured and simulated steady-state stator current waveforms are shown in Figure 5.10 and Figure 5.11, respectively. Both waveforms again display a stable period-one orbit with a frequency of around 45.9 *Hz*. The rms current in both cases is around 3.5 *A*.

It is noted from Tests 1-3 that the magnitude of the stator currents is increased as the values of the self-excitation capacitor bank are increased. This is because at higher values of  $C$ , the slope of the load line representing the reactance of the self-excitation capacitors ( $1/\omega C$ ) is reduced intercepting the magnetising curve (as shown in Figure 5.2) at a higher value of current.

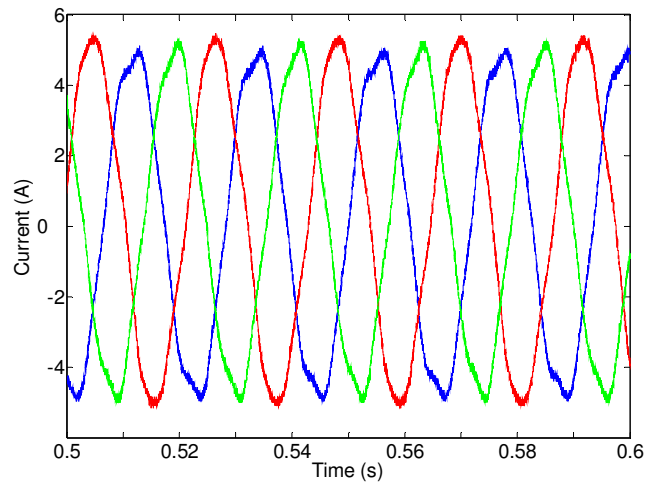


Figure 5.10 Test 3 – Measured stator line current waveforms at no-load with  $C = 90 \mu F$  per phase – Period-one waveforms.

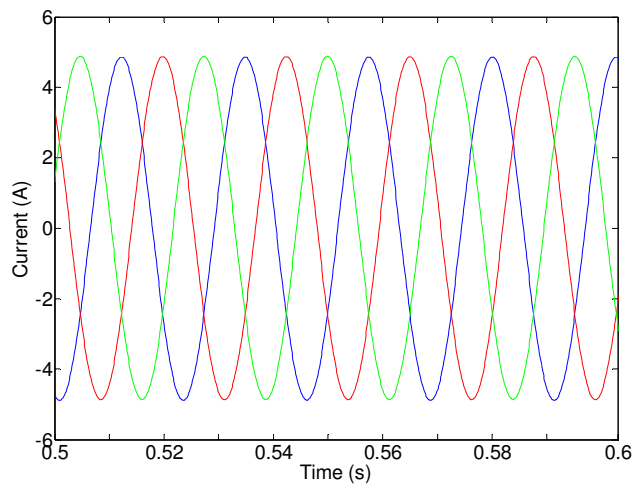


Figure 5.11 Test 3 – Simulated stator line current waveforms at no-load with  $C = 90 \mu F$  per phase – Period-one waveforms.

## 5.4 SEIG PURELY RESISTIVE LOAD TESTS

A variable resistive load is connected across the SEIG stator terminals in parallel with the  $45 \mu F$  self-excitation capacitor bank after the initial self-excitation process in this group of three tests. Measured test results are again compared with the results from the Simulink model of the SEIG.

### 5.4.1 TEST 4; $R = 60 \Omega$ ; $C = 45 \mu F$

In this test, the SEIG stator terminals are connected to a three-phase resistive load of  $60 \Omega$  per phase after the self-excitation process had been completed. The tachometer recorded a rotor steady-state shaft speed of  $3665 \text{ rpm}$  when the stator voltage reaches its rated  $240 \text{ V}$  value. The corresponding measured and simulated steady-state stator current waveforms are shown in Figure 5.12 and Figure 5.13. Both waveforms are period-one orbits with a frequency of around  $58.1 \text{ Hz}$ . The rms value of both measured and simulated currents is around  $3.2 \text{ A}$ .

It is noticed that the three current waveforms shown in Figure 5.12 are more balanced than those recorded from no-load tests, this maybe because of the connection of the three-phase resistive load presenting a more balanced operating condition to the SEIG.

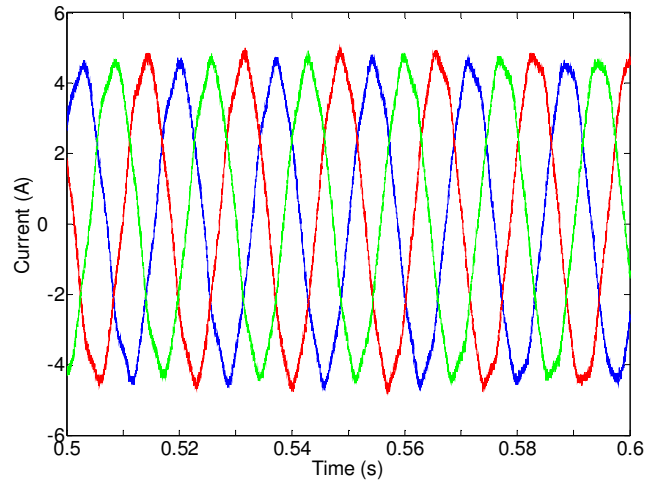


Figure 5.12 Test 4 – Measured stator line current waveforms with  $R = 60 \Omega$  and  $C = 45 \mu F$  per phase – Period-one waveforms.

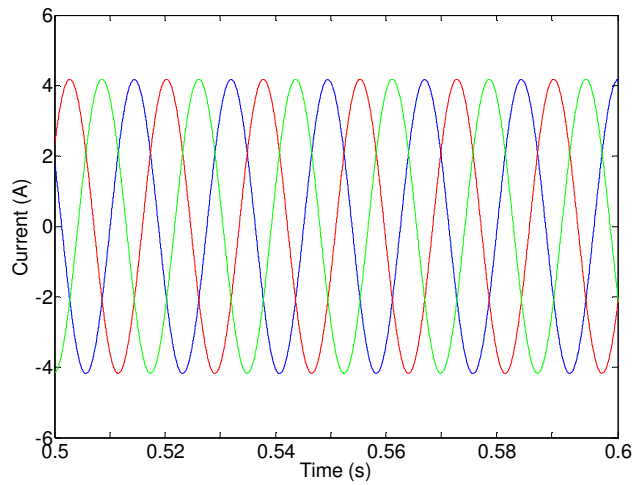


Figure 5.13 Test 4 – Simulated stator line current waveforms with  $R = 60 \Omega$  and  $C = 45 \mu F$  per phase – Period-one waveforms.

**5.4.2 TEST 5;  $R = 50 \Omega$ ;  $C = 45 \mu F$** 

The SEIG is next tested with decreasing the load resistance to  $50 \Omega$  per phase connected after the self-excitation process had been completed. The tachometer recorded a rotor steady-state shaft speed of  $3814 \text{ rpm}$  when the stator voltage reaches its rated value of  $240 \text{ V}$ . The measured and simulated steady-state stator current waveforms are shown in Figure 5.14 and Figure 5.15, respectively. It is noted that both waveforms are period-one orbits with a frequency and rms current of around  $60 \text{ Hz}$  and  $3.6 \text{ A}$ , respectively.

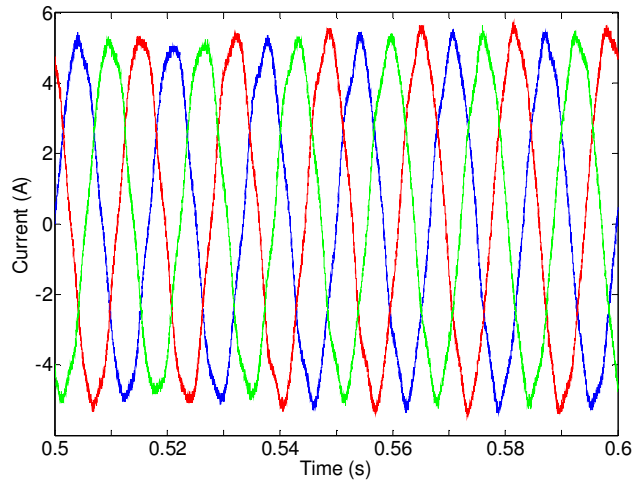


Figure 5.14 Test 5 – Measured stator line current waveforms with  $R = 50 \Omega$  and  $C = 45 \mu F$  per phase – Period-one waveforms.

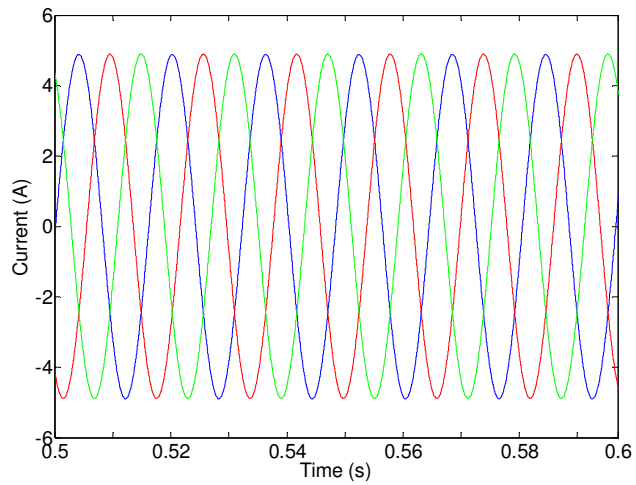


Figure 5.15 Test 5 – Simulated stator line current waveforms with  $R = 50 \Omega$  and  $C = 45 \mu F$  per phase – Period-one waveforms.

### 5.4.3 TEST 6; $R = 40 \Omega$ ; $C = 45 \mu F$

Finally, a three-phase resistive load of  $40 \Omega$  per phase is connected to the SEIG stator terminals after the self-excitation process had been completed. The tachometer recorded a rotor steady-state shaft speed of  $4057 \text{ rpm}$  when the stator voltage reached its rated value of  $240 \text{ V}$ . The measured and simulated steady-state stator current waveforms are shown in Figure 5.16 and Figure 5.17, respectively. The waveforms generated from the experimental test confirm the accuracy of the proposed Simulink model under the same operational conditions. Both are period-one orbits with a frequency and rms current of around  $64 \text{ Hz}$  and  $4.3 \text{ A}$ , respectively.

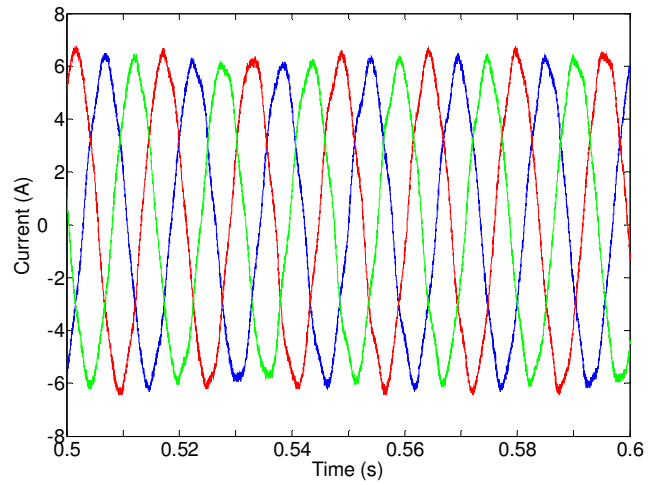


Figure 5.16 Test 6 – Measured stator line current waveforms with  $R = 40 \Omega$  and  $C = 45 \mu F$  per phase – Period-one waveforms.

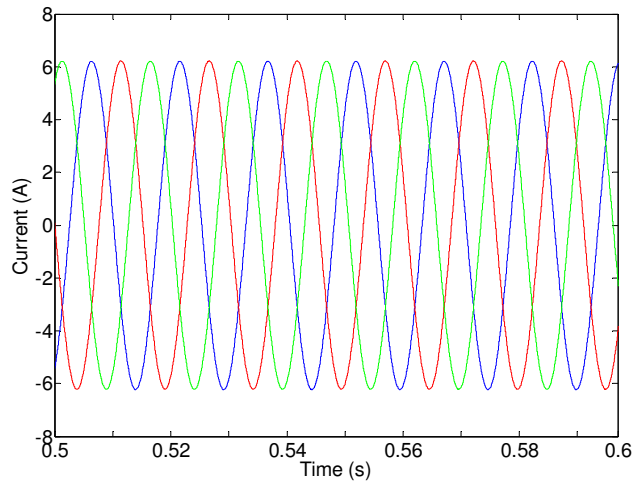


Figure 5.17 Test 6 – Simulated stator line current waveforms with  $R = 40 \Omega$  and  $C = 45 \mu F$  per phase – Period-one waveforms.

#### 5.4.4 PHASE PLANE AND HARMONIC EXAMINATION OF THE PERIOD-ONE LINEAR ORBIT

The stator current waveforms of the SEIG when feeding a resistive load (period-one orbit) are examined by both phase plane and harmonic spectrum presentations in this section.

Taking the case of the  $50\ \Omega$  resistive load and  $45\ \mu F$  self-excitation capacitance (Test 5) as an example of a period-one operating point, the corresponding phase plane diagram of stator line currents  $i_c$  versus  $i_b$  is shown in Figure 5.18. The corresponding Poincaré section of the sampled states of these two line currents when  $i_a$  is zero (rising edge) is plotted in Figure 5.19. Clearly, the phase plane diagram is a closed circle and the Poincaré section is almost a single dot demonstrating the characteristic of stable period-one orbit of the measured stator current waveforms under this operating condition.

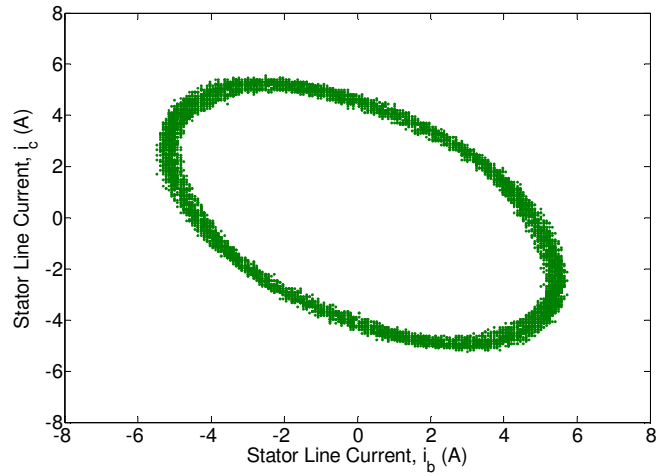


Figure 5.18 Stator line current  $i_c$  versus  $i_b$  phase plane diagram – Period-one.

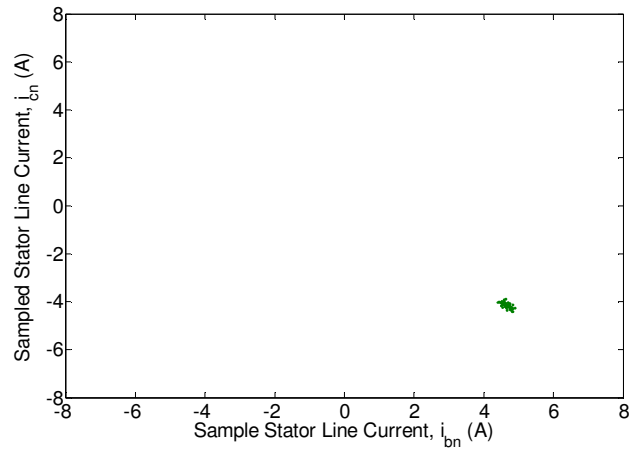


Figure 5.19 Sampled states of stator line current  $i_{cn}$  versus  $i_{bn}$  Poincaré section – Period-one.

With a purely resistive load applied to the stator terminals of the SEIG, the waveforms are sinusoidal (period-one orbit) as shown in the Fast Fourier Transform (FFT) plot of Figure 5.20 with only one dominating frequency.

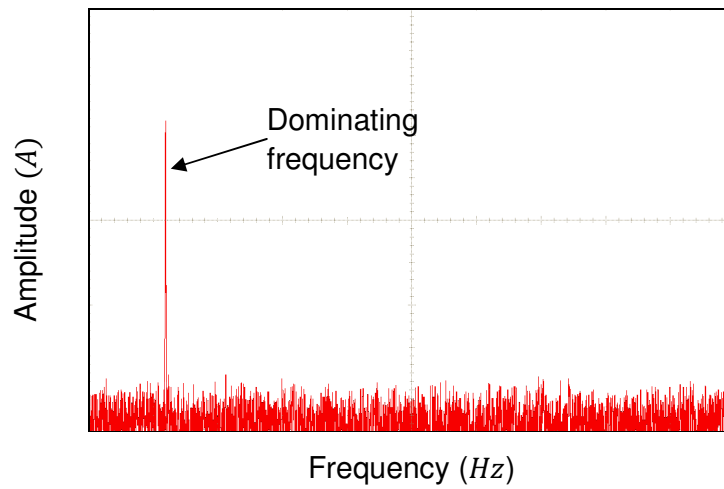


Figure 5.20 SEIG current FFT with resistive load ( $R = 50 \Omega$ ); The frequency and amplitude of the dominating signal are approximately  $60 \text{ Hz}$  and  $5.1 \text{ A}$ .

## 5.5 SEIG INDUCTIVE LOAD TESTS

A variable inductive load ( $RL$ ) is connected across the SEIG stator terminals in parallel with the  $45 \mu F$  per phase self-excitation capacitor bank in this group of three tests. The nonlinear behaviour of the SEIG feeding an inductive load is examined by using the load resistance and inductance as the control parameters. Measured test results are again compared with the results from the Simulink model of the SEIG. For clarity, only one line current is presented in each diagram in this section.

### 5.5.1 TEST 7; $R = 90 \Omega$ ; $L = 1.7 mH$ ; $C = 45 \mu F$ (BASE CASE)

When a three-phase inductive load ( $RL$ ) is applied to the stator terminals of the induction generator, system behaviour changes from a period-one linear orbit to a nonlinear orbit as load parameters are varied. A stable period-one orbit base case is presented first (Test 7) in this section.

With load resistance  $R = 90 \Omega$ , load inductance  $L = 1.7 mH$  and self-excitation capacitance  $C = 45 \mu F$  per phase, the tachometer recorded a steady-state shaft speed of  $3472 rpm$  at the rated stator voltage of  $240 V$ . Experimental and simulated stator steady-state line current waveforms are plotted in Figure 5.21 and Figure 5.22. Both current waveforms are period-one closed orbits with a frequency of around  $56 Hz$ . The rms value of stator line current in both cases is around  $2.5 A$ .

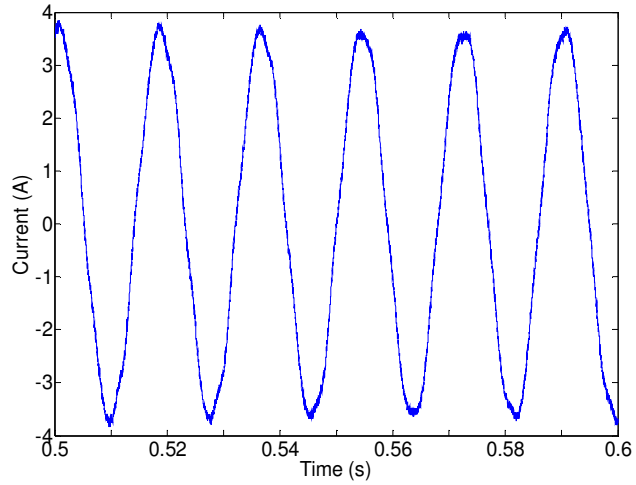


Figure 5.21 Test 7 – Measured stator line current waveform with  $R = 90 \Omega$ ,  $L = 1.7 \text{ mH}$  and  $C = 45 \mu\text{F}$  per phase – Period-one waveform.

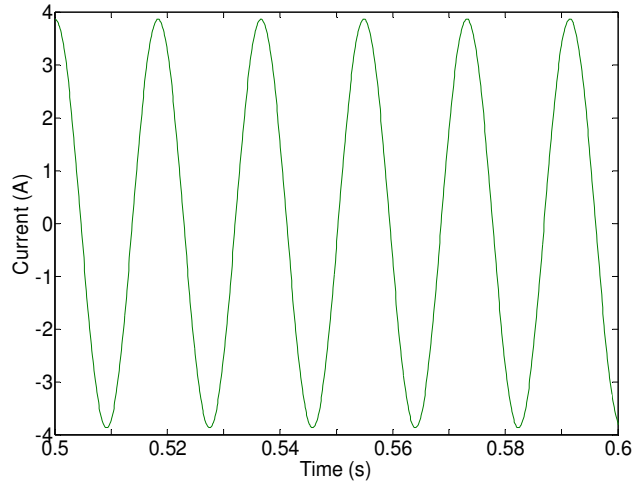


Figure 5.22 Test 7 – Simulated stator line current waveforms with  $R = 90 \Omega$ ,  $L = 1.7 \text{ mH}$  and  $C = 45 \mu\text{F}$  per phase – Period-one waveform.

**5.5.2 TEST 8;  $R = 60 \Omega$ ;  $L = 60 \text{ mH}$ ;  $C = 45 \mu\text{F}$** 

With a value of  $R = 60 \Omega$  per phase and  $L = 60 \text{ mH}$  (decreasing the resistive and increasing the inductive element of the load when compared with the base case), the tachometer recorded a steady-state shaft speed of  $3703 \text{ rpm}$  at the rated stator voltage of  $240 \text{ V}$ . Experimental and simulated stator steady-state line current waveforms of  $59.6 \text{ Hz}$  are plotted in Figure 5.23 and Figure 5.24.

A closer look at these figures reveals that the stator current waveforms are highly distorted. More than one frequency component now appears in the plots as the response of the system changes from a period-one orbit (base case) to a nonlinear orbit.

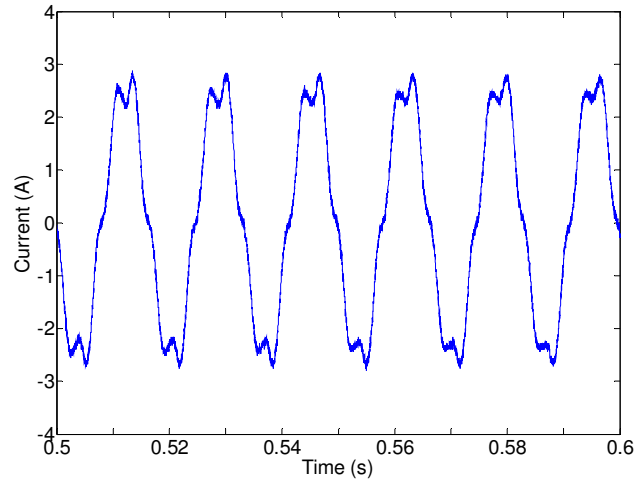


Figure 5.23 Test 8 – Measured stator line current waveform with  $R = 60 \Omega$ ,  $L = 60 \text{ mH}$  and  $C = 45 \mu\text{F}$  per phase – Distorted waveform.

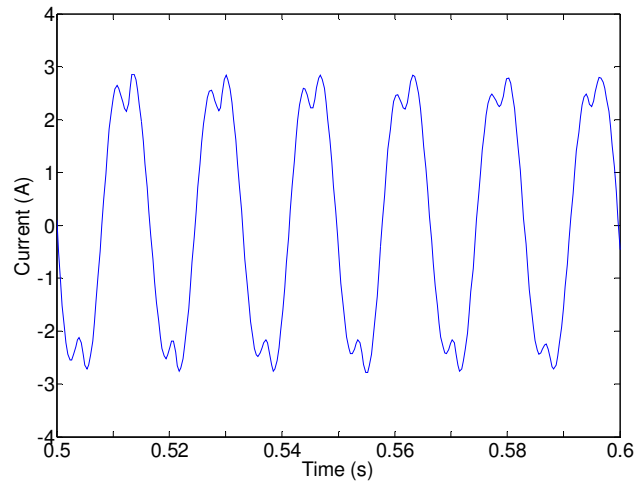


Figure 5.24 Test 8 – Simulated stator line current waveform with  $R = 60 \Omega$ ,  $L = 60 \text{ mH}$  and  $C = 45 \mu\text{F}$  per phase – Distorted waveform.

**5.5.3 TEST 9;  $R = 40 \Omega$ ;  $L = 11 \text{ mH}$ ;  $C = 45 \mu\text{F}$** 

With a value of  $R = 40 \Omega$  and  $L = 11 \text{ mH}$  per phase (further decreasing the resistive and increasing the inductive element of the load when compared with the base case), the tachometer recorded a steady-state shaft speed equal to  $4297 \text{ rpm}$  when the stator voltage reaches its rated value of  $240 \text{ V}$ . The stator steady-state line current waveforms of  $69.1 \text{ Hz}$  acquired from the testing and the Simulink model are plotted in Figure 5.25 and Figure 5.26. In both cases, the stator currents are distorted and the system is entering the nonlinear region.

It is clear from the previous two tests that by increasing the load inductance and decreasing the load resistance (reducing the power factor of the load), the response of the SEIG system is transformed from a linear period-one orbit to a nonlinear orbit in agreement with the system's behaviour which will be further analysed numerically in Chapter Six. Although the shape of the waveforms recorded from nonlinear Simulink model does not match the measured plot completely, the behaviour of the system is the same, moving from a linear period-one response to a highly nonlinear response as the load is changed.

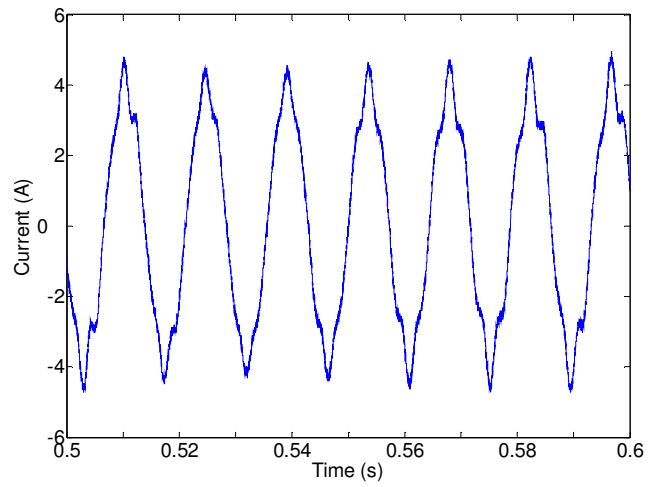


Figure 5.25 Test 9 – Measured stator line current waveform with  $L = 11 \text{ mH}$ ,  $R = 40 \Omega$  and  $C = 45 \mu\text{F}$  per phase – Distorted waveform.

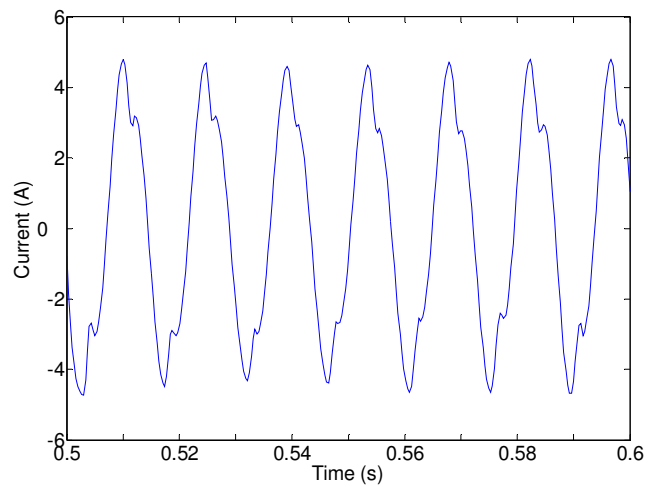


Figure 5.26 Test 9 – Simulated stator line current waveform with  $L = 11 \text{ mH}$ ,  $R = 40 \Omega$  and  $C = 45 \mu\text{F}$  per phase – Distorted waveform.

#### 5.5.4 PHASE PLANE AND HARMONIC EXAMINATION OF THE NONLINEAR ORBIT

The phase plane diagram and harmonic spectrum of the distorted stator current waveform of the SEIG when feeding an inductive ( $RL$ ) load are examined in this section.

Taking the case of SEIG operation at  $R = 40 \Omega$ ,  $L = 11 \text{ mH}$  and  $C = 45 \mu\text{F}$  per phase (Test 9) as an example of a nonlinear operating point. The phase plane diagram and Poincaré section of the stator line current  $i_c/i_{cn}$  versus  $i_b/i_{bn}$  (shown in Figure 5.27 and Figure 5.28, respectively) demonstrate the nonlinear behaviour of the system at this operating point as the phase plane diagram is not a circle and the Poincaré map is not a single dot any more. Hence, the behaviour of the system moves from a linear period-one response to a highly nonlinear response at this operating point.

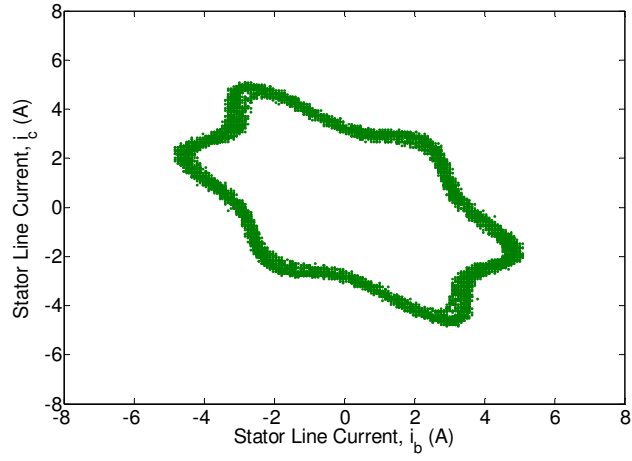


Figure 5.27 Stator line current  $i_c$  versus  $i_b$  phase plane diagram.

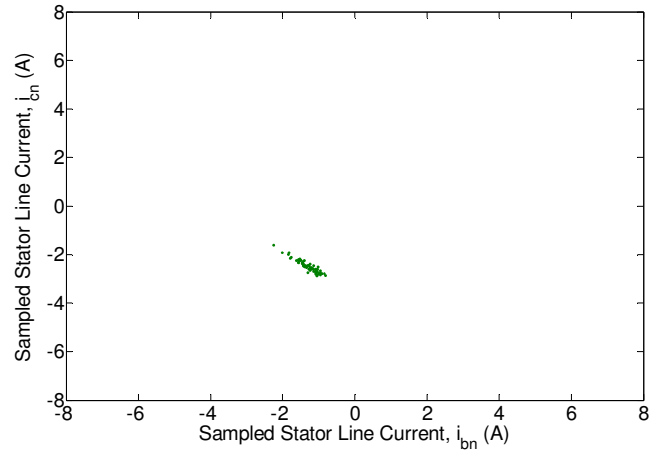


Figure 5.28 Sampled states of stator line current  $i_{cn}$  versus  $i_{bn}$  Poincaré map.

The nonlinear nature of the system's response is further demonstrated by the frequency spectrum of the stator current waveform (Figure 5.29) showing the presence of other frequency components besides the main fundamental component.

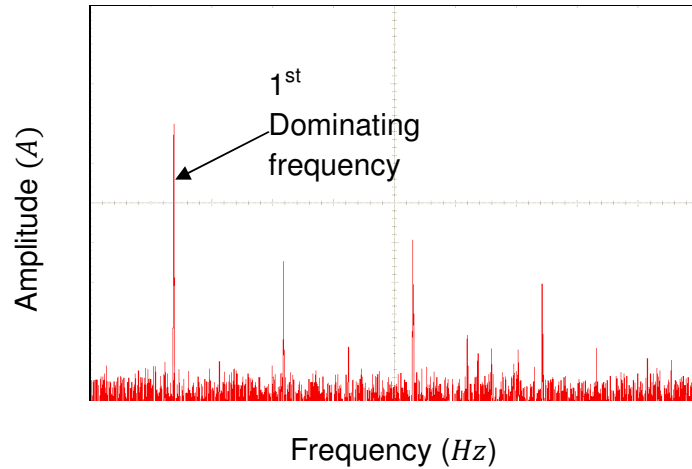


Figure 5.29 SEIG current FFT with an inductive load ( $R = 40 \Omega, L = 11 \text{ mH}$ ); The frequency and amplitude of the 1<sup>st</sup> dominating signal are approximately  $69 \text{ Hz}$  and  $5 \text{ A}$ .

## 5.6 CHAOTIC WAVEFORMS

A number of chaotic waveforms generated from the Simulink model when the SEIG feeding higher inductive load ( $RL$ ) are presented in this section. It was not possible to obtain any chaotic waveforms in the laboratory under practical and safe operating conditions. For chaos to appear, extremely high rotational speeds and/or stator currents/voltages would have been necessary. Therefore, no experimental chaotic waveforms were observed under laboratory conditions.

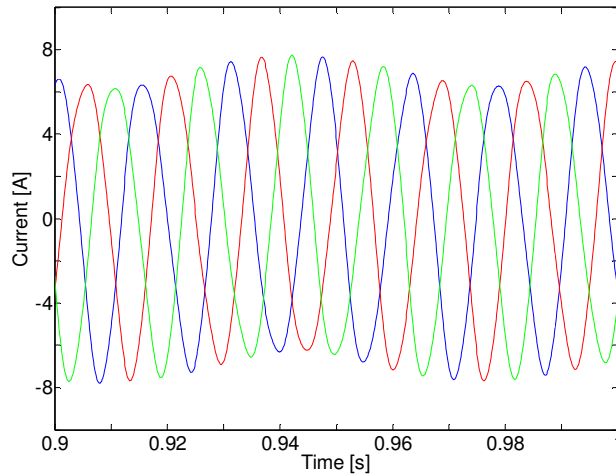


Figure 5.30 Stator three line current waveforms  $R = 60 \Omega$ ,  $L = 70 \text{ mH}$  and  $C = 45 \mu\text{F}$  per phase and the rotor shaft speed at  $4101 \text{ rpm}$  – Chaotic behaviour.

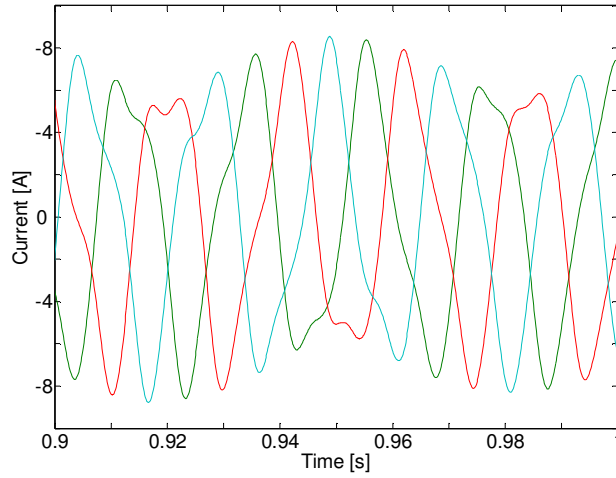


Figure 5.31 Stator three line current waveforms  $R = 90 \Omega$ ,  $L = 90 \text{ mH}$  and  $C = 45 \mu\text{F}$  per phase and the rotor shaft speed at 4126 rpm – Chaotic behaviour.

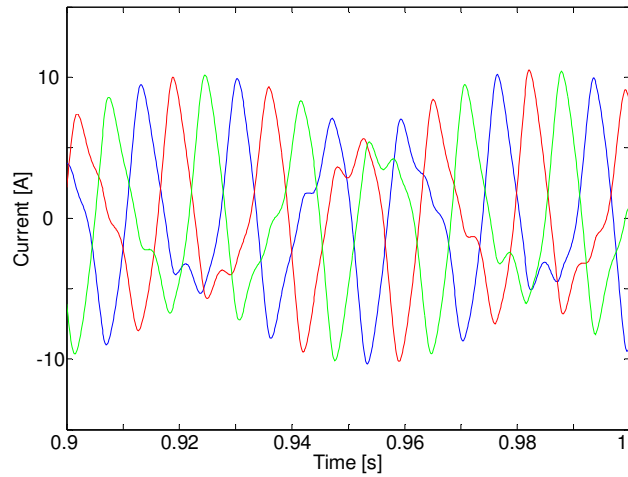


Figure 5.32 Stator three line current waveforms  $R = 60 \Omega$ ,  $L = 73 \text{ mH}$  and  $C = 45 \mu\text{F}$  per phase and the rotor shaft speed at 4177 rpm – Chaotic behaviour.

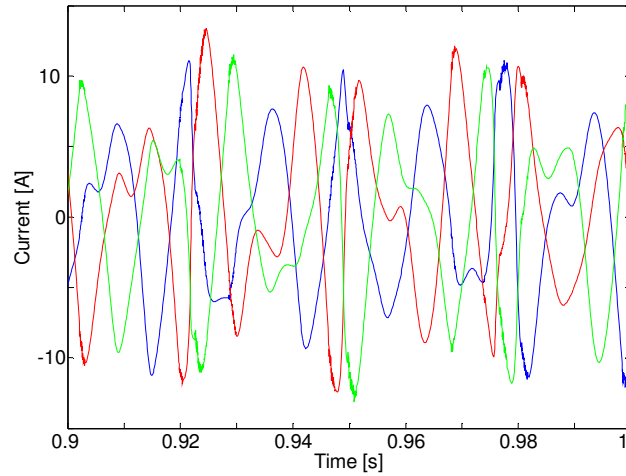


Figure 5.33 Stator three line current waveforms with  $R = 60 \Omega$ ,  $L = 80 \text{ mH}$  and  $C = 45 \mu\text{F}$  per phase and the rotor shaft speed at  $4206 \text{ rpm}$  – Chaotic behaviour.

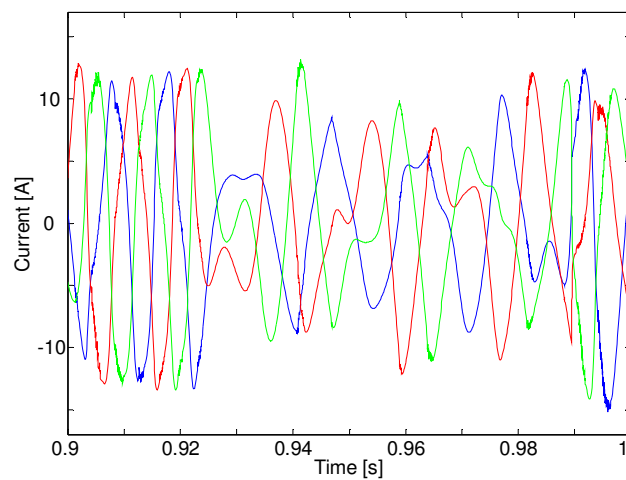


Figure 5.34 Stator three line current waveforms with  $R = 55 \Omega$ ,  $L = 91 \text{ mH}$  and  $C = 45 \mu\text{F}$  per phase and the rotor shaft speed at  $4356 \text{ rpm}$  – Chaotic behaviour.

It is noted from the above figures that the machine exhibits chaotic motion by increasing the inductive load, the rotor shaft speed and decreasing the resistive load.

## 5.7 SUMMARY

In this chapter, laboratory tests were carried out on the SEIG when feeding no-load, a purely resistive load ( $R$ ) and an inductive load ( $RL$ ) and the results were presented to validate the Simulink model developed in Chapter Four.

The magnetising characteristics of the induction machine were measured with the machine running at synchronous speed, as the rotor and load parameters of the equivalent circuit could then be ignored (slip  $s = 0$ ) under this operating condition.

The experimental results confirmed the validity of the proposed SEIG Simulink model. The experimental and simulated waveforms shown in this chapter demonstrated how system's behaviour changes from a stable period-one orbit to a nonlinear orbit as a result of a change in a system parameter such as the resistive and/or the inductive element of the SEIG inductive load ( $RL$ ).

It was observed that there was only one dominating frequency in the linear operating region, whereas a few dominating frequencies were present in the nonlinear operating region.

Only period-one linear responses were obtained with the generator operating at no-load or with a purely resistive load conditions. When feeding an inductive load ( $RL$ ), the period-one behaviour of the system was distorted as the value of load was varied. A number of chaotic waveforms of the SEIG when feeding an inductive load were simulated using the Simulink model under some extreme operating conditions (e.g. high rotational speeds, stator currents and voltages).

# CHAPTER 6

## NUMERICAL ANALYSIS OF THE SEIG NONLINEAR BEHAVIOUR

A model of the SEIG with stator and rotor  $d$ - $q$  axis currents as state variables was presented in Chapter Four. This model is used in the following sections to study the behaviour of the SEIG as a nonlinear dynamic system by using both simulation and numerical analysis tools.

Unfortunately, the behaviour of the 1.1 kW machine used in the experimental investigation described in the previous chapter displayed a very narrow quasi-periodic window, making it extremely difficult to study the transition from stable period-one operation to quasi-periodicity. Therefore, it was decided that the parameters of the induction machine described in Chapter Four should be used in this chapter for further analysis of this characteristic system behaviour. A base case is presented first showing stator current waveform for a stable operating point (period-one orbit) of the SEIG when feeding an inductive load. The behaviour of the SEIG is then examined as one of three parameters of the system is changed: 1) the self-excitation capacitance; 2) the load resistance and 3) the rotor speed. For each scenario, steady-state stator current time domain waveforms, phase plane diagrams, Poincaré maps and bifurcation diagrams are presented. The results show how the behaviour of the system changes from periodic one to quasi-periodic and then a likely chaotic motion as these control parameters are varied.

The stability characteristics of the period-one and quasi-period orbits are then analysed numerically to give an overview of the movement of the eigenvalues of the system following the introduction of a small disturbance into the system.

### 6.1 BASE CASE – PERIOD-ONE ORBIT

A balanced three-phase inductive load ( $RL$ ) comprising a  $30\ \Omega$  resistor in series with a  $15\ mH$  inductor per phase is connected to the stator terminals in parallel with the star connected  $135\ \mu F$  per phase excitation capacitors and the machine driven at a constant speed of  $1500\ rpm$  ( $314\ rad/s$ ).

The time domain stator current waveform and phase plane diagram of the stator  $d$ - $q$  axis currents are plotted in Figure 6.1 and Figure 6.2, respectively. The response of the system is a period-one closed orbit which indicates that the system operates within the desired stable region of operation. Only two representative states ( $i_{sQ}$  and  $i_{sD}$ ) are plotted in Figure 6.2. All other combinations give similar results and are not shown here.

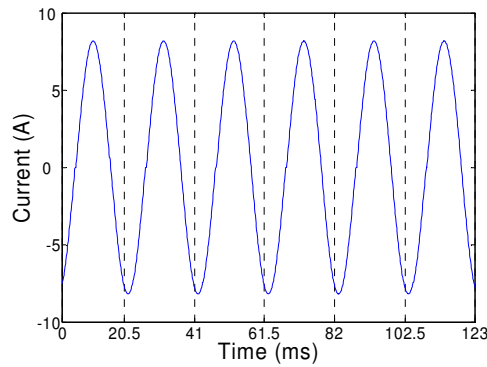


Figure 6.1 Stator line current waveform for  $C = 135\ \mu F$ ,  $R = 30\ \Omega$  and  $\omega_r = 314\ rad/s$ .

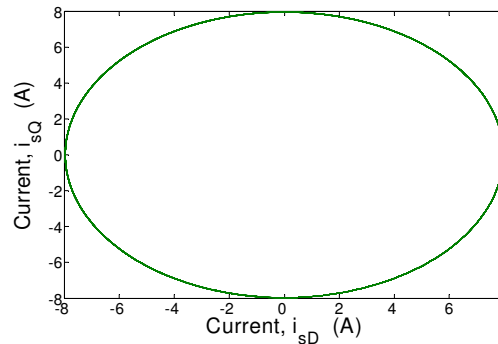


Figure 6.2 Phase plane diagram for  $C = 135\ \mu F$ ,  $R = 30\ \Omega$  and  $\omega_r = 314\ rad/s$ .

## 6.2 SEIG NONLINEAR BEHAVIOUR

The nonlinear behaviour of the SEIG system described above is further investigated in this section by varying the values of three control parameters: the self-excitation capacitance, the load resistance and the rotor speed. It shall be noted that only one control parameter is changed at a time while the other two are maintained at the same values used in the stable period-one base case.

### 6.2.1 CHANGING THE SELF-EXCITATION CAPACITANCE $C$

Using the self-excitation capacitance as the bifurcation parameter, the bifurcation diagram of the system created by sampling the value of the  $q$  axis stator current when the  $d$  axis stator current is zero is shown in Figure 6.3. As the value of  $C$  increases, it can be seen that the system bifurcates from a stable period-one orbit to chaos via a quasi-periodic route. Orbits of periods five, seven, nine and eleven also appear for short windows in the bifurcation diagram. Due to the space limitation, these waveforms are not presented here. This type of steady-state behaviour is referred to as a Neimark bifurcation as described in Chapter Three [67]. Figure 6.4 gives a clearer view of the transition to quasi-periodicity.

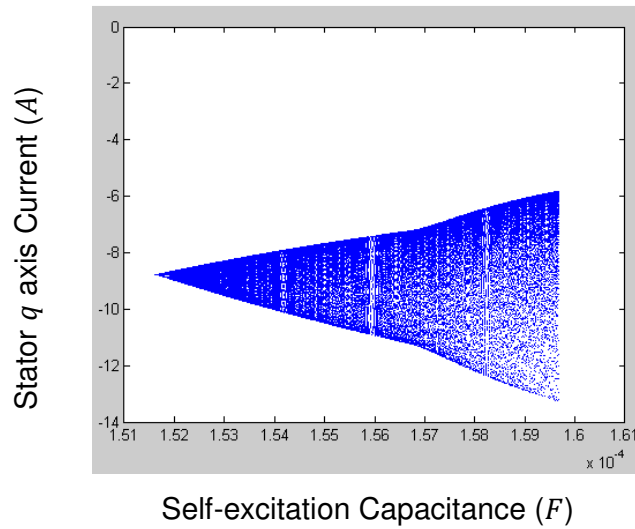


Figure 6.3 Bifurcation diagram with  $C$  as the bifurcation parameter.

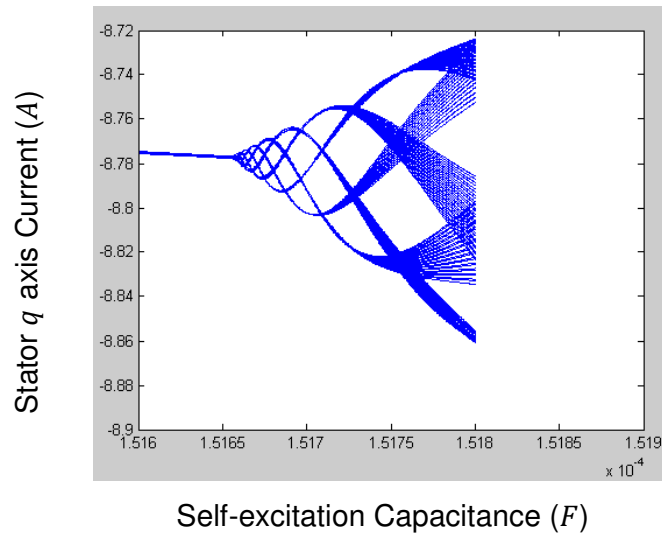


Figure 6.4 Bifurcation diagram with  $C$  as the bifurcation parameter (zoom in).

The system is transferred from a period-one orbit to a quasi-period orbit by increasing the self-excitation capacitance. At  $C = 152 \mu F$  the current waveform is clearly distorted as shown in Figure 6.5. The response is quasi-periodic as demonstrated in the corresponding phase plane diagram given in Figure 6.6.

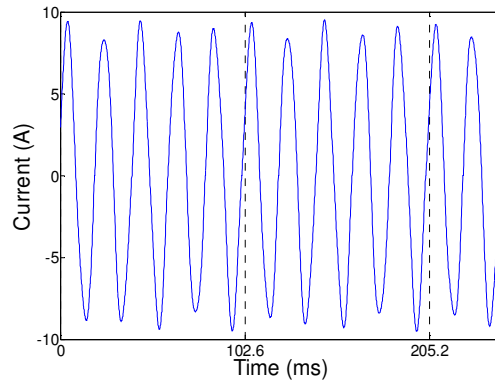


Figure 6.5 Stator line current waveform for  $C = 152 \mu F$  – Quasi-periodic response.

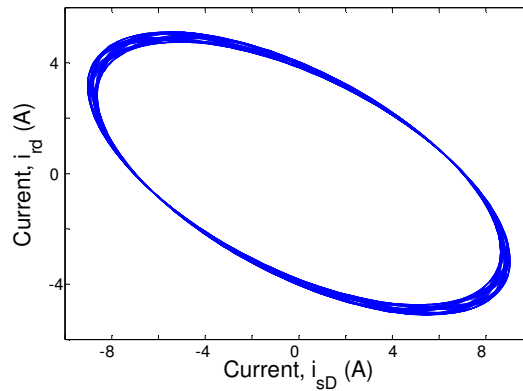


Figure 6.6 Phase plane diagram for  $C = 152 \mu F$  – Quasi-periodic response.

When the control parameter is further increased to  $C = 156 \mu F$ , the response of the system does not follow any specific periodic pattern but is instead quasi-periodic. The resulting stator current waveform and the stator/rotor  $d$ - $q$  axis phase plane diagrams are shown in Figure 6.7 and Figure 6.8, respectively. The phase space diagram is plotted using 5000 data points showing that the locus of the solution lies on a 'toroid typed' manifold.

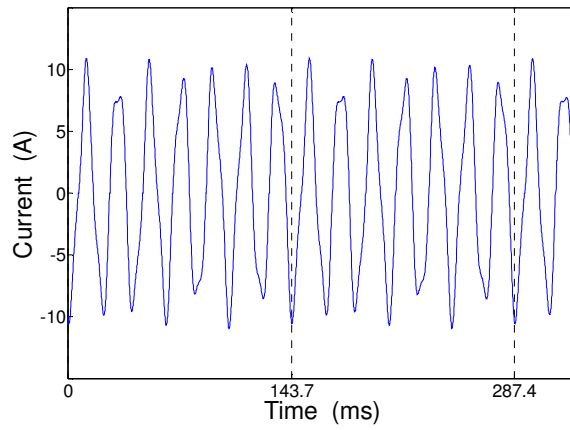
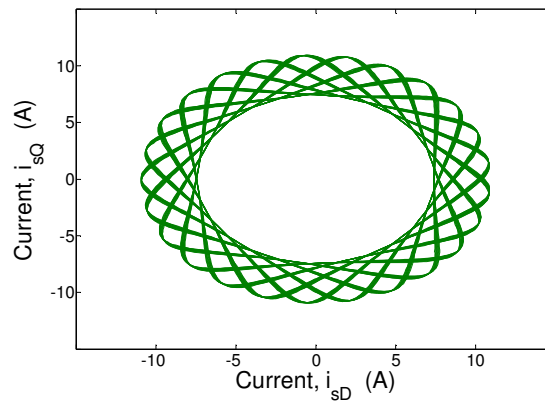
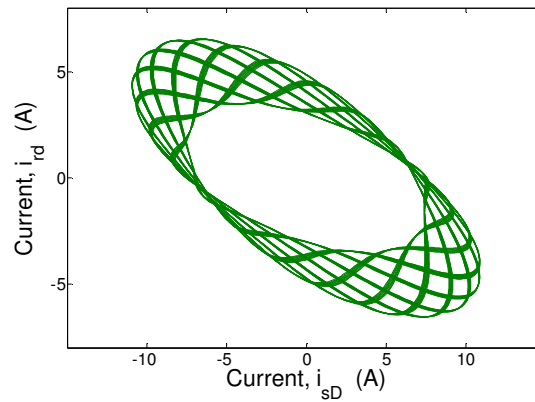


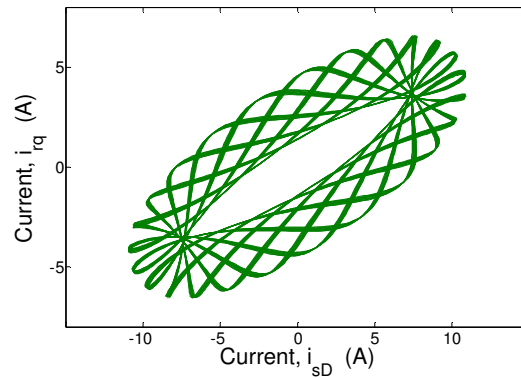
Figure 6.7 Stator line current waveform for  $C = 156 \mu F$  – Quasi-periodic response.



a)  $i_{sQ}$  versus  $i_{sD}$  phase plane diagram.



b)  $i_{rd}$  versus  $i_{sD}$  phase plane diagram.



c)  $i_{rq}$  versus  $i_{sD}$  phase plane diagram.

Figure 6.8 Phase plane diagrams for  $C = 156 \mu F$  (with 5000 data points) - Quasi-periodic response.

Figure 6.9 shows 20,000 data points of the previous tori (Figure 6.8 a)  $i_{sQ}$  versus  $i_{sD}$  phase plane diagram) and is clearly demonstrating that the orbit is dense on the torus and providing further verification of the quasi-periodic nature of the system's response. What's more, by sampling the state vector when the current  $i_{sD}$  is zero, the Poincaré section of the system can be obtained (Figure 6.10) showing a closed orbit which again is a characteristic of quasi-periodic nonlinear dynamic systems.

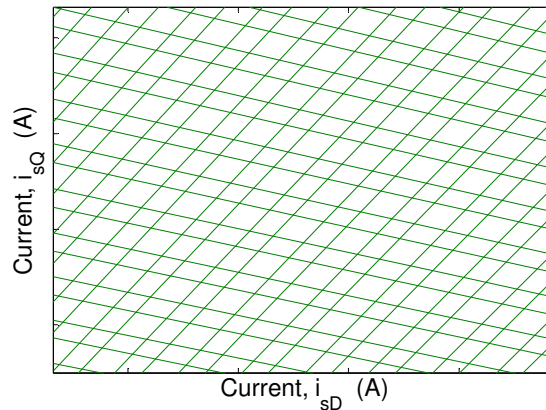
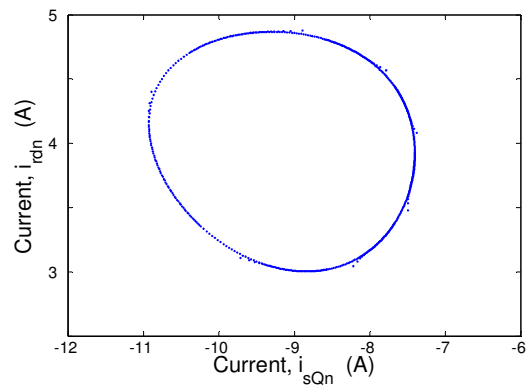
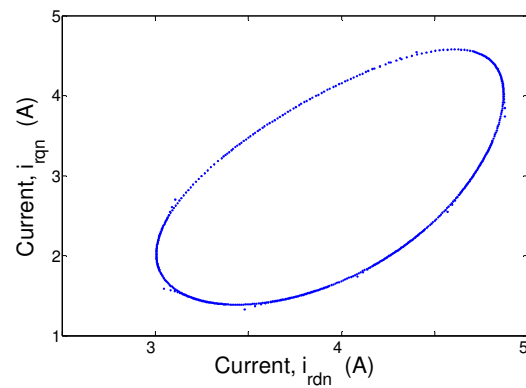


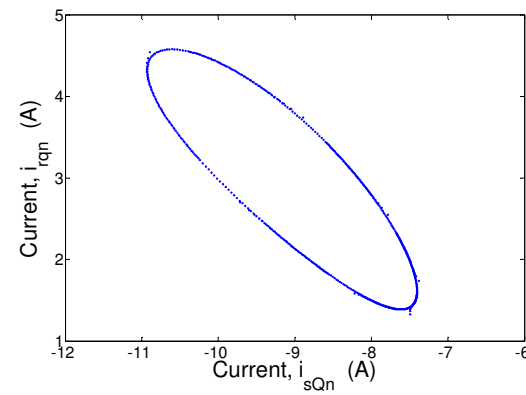
Figure 6.9 Dense orbit in the torus ( $i_{sQ}$  versus  $i_{sD}$  with 20,000 data points).



a)  $i_{rdn}$  versus  $i_{sQn}$  Poincaré map.



b)  $i_{rqn}$  versus  $i_{rdn}$  Poincaré map.



c)  $i_{rqn}$  versus  $i_{sQn}$  Poincaré map.

Figure 6.10 Poincaré sections for  $C = 156 \mu F$  (sample at  $i_{sD} = 0$ ).

### 6.2.2 CHANGING THE LOAD RESISTANCE $R$

The behaviour of the SEIG feeding an inductive load ( $RL$ ) when changing the control parameter  $R$  (load resistance) is examined in this section. Figure 6.11 shows the bifurcation diagram of the system created by sampling the value of the  $q$  axis stator current when the  $d$  axis stator current is zero, using  $R$  as the bifurcation parameter and maintaining other parameters at their base values ( $C = 135 \Omega$  and  $\omega_r = 314 \text{ rad/s}$ ). As the load resistance is reduced from its base value of  $30 \Omega$ , the diagram shows how the system loses its stability at about  $28.5 \Omega$  through a Neimark bifurcation before entering a quasi-periodic region ultimately leading to chaos.

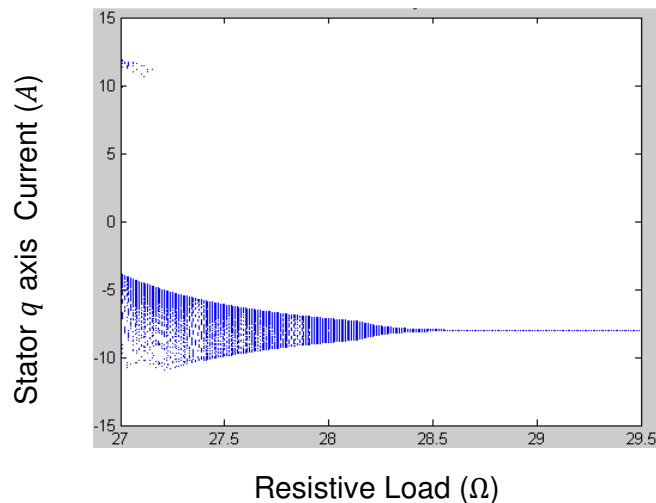


Figure 6.11 Bifurcation diagram with  $R$  as the bifurcation parameter.

Two points on the diagram will now be examined more closely. The stator current waveform and the phase plane diagram (rotor  $d$  axis current versus stator  $d$  axis current) for  $R = 28 \Omega$  are shown in Figure 6.12 and Figure 6.13, respectively. System response does not follow any periodic pattern but is instead quasi-periodic, in agreement with the bifurcation diagram of Figure 6.11.

The resulting stator current waveform and the phase plane diagram when  $R$  is further reduced to  $27 \Omega$  are shown in Figure 6.14 and Figure 6.15. The figures show that the motion of the stator current has no regular pattern indicating that the system behaves chaotically.

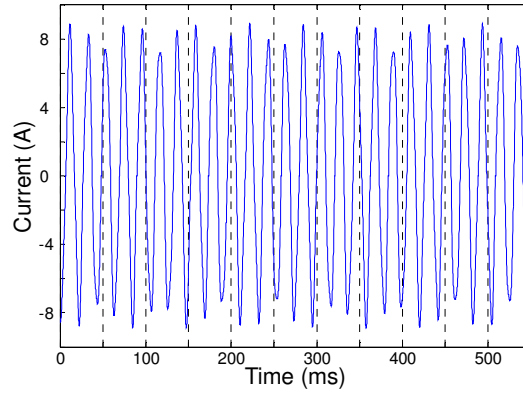


Figure 6.12 Stator line current waveform for  $R = 28 \Omega$  – Quasi-periodic response.

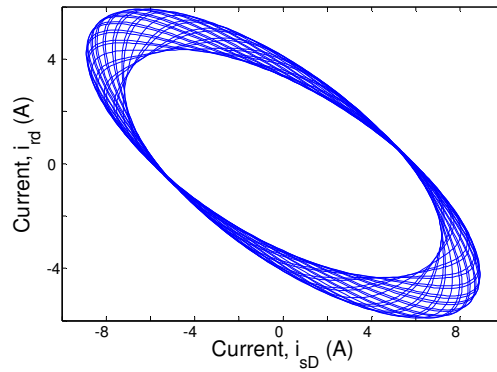


Figure 6.13 Phase plane diagram for  $R = 28 \Omega$  – Quasi-periodic response.

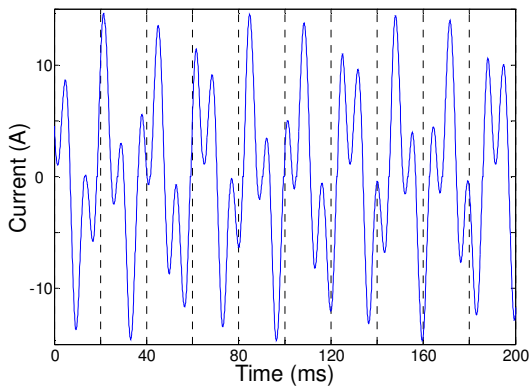


Figure 6.14 Stator line current waveform for  $R = 27 \Omega$  – Chaotic response.

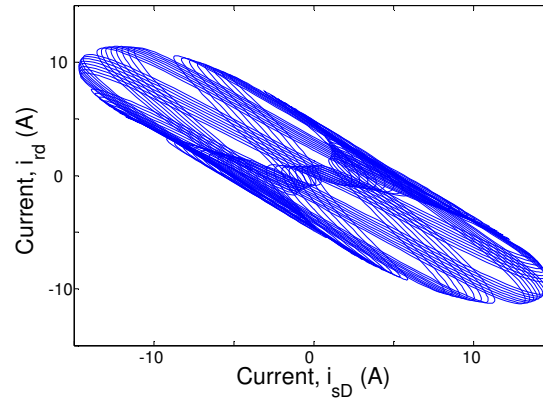


Figure 6.15 Phase plane diagram for  $R = 27 \Omega$  – Chaotic response.

### 6.2.3 CHANGING THE ROTOR SPEED $\omega_r$

The dynamic behaviour of the system when varying the rotational speed of the rotor while maintaining other parameters at their base values ( $C = 135 \mu F$  and  $R = 30 \Omega$ ) is studied in this section.

The bifurcation diagram of the system with rotor speed as the bifurcation parameter (obtained by sampling the  $q$  axis stator current when the  $d$  axis stator current is zero) is shown in Figure 6.16. The diagram captures system's behaviour from the initial base case period-one response to eventual chaotic motions via regions of quasi-periodicity, period seven and period eleven orbits. Other periodic orbits are also presented but are not highlighted here due to space limitations.

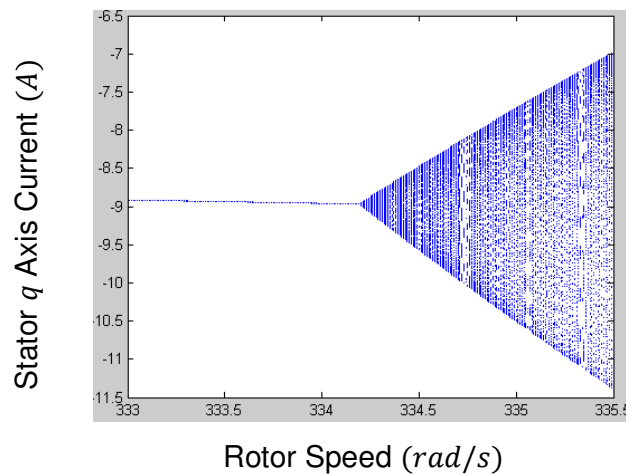


Figure 6.16 Bifurcation diagram with  $\omega_r$  as the bifurcation parameter.

The resulting quasi-periodic stator current waveform and phase plane diagram for  $\omega_r = 334.5 \text{ rad/s}$  are shown in Figure 6.17 and Figure 6.18.

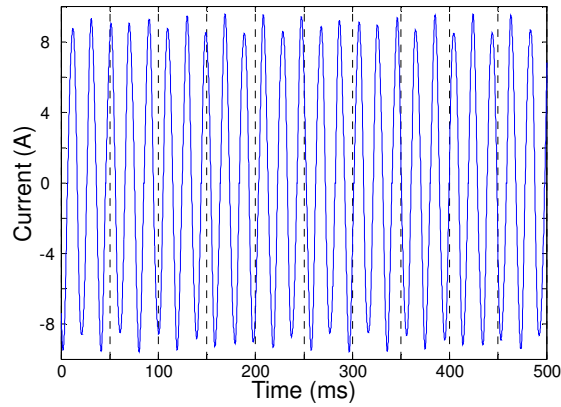


Figure 6.17 Stator line current waveform for  $\omega_r = 334.5 \text{ rad/s}$  – Quasi-periodic response.

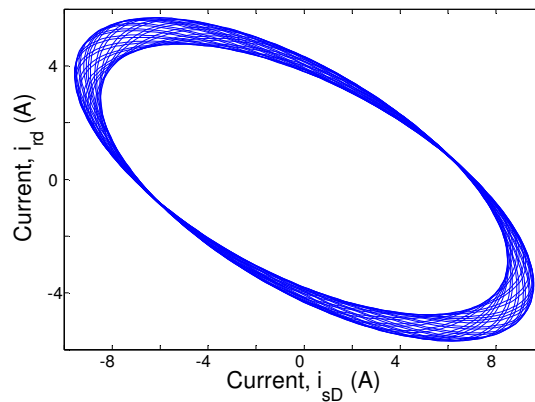


Figure 6.18 Phase plane diagram for  $\omega_r = 334.5 \text{ rad/s}$  – Quasi-periodic response.

By further increasing the control parameter  $\omega_r$  to  $335.1 \text{ rad/s}$ , the stator current waveform is more distorted and the system retains its quasi-periodic behaviour.

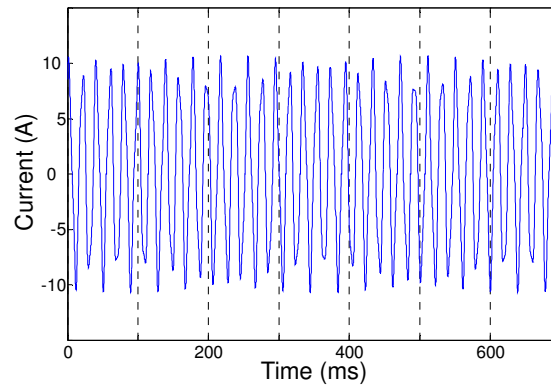


Figure 6.19 Stator line current waveform for  $\omega_r = 335.1 \text{ rad/s}$  – Quasi-periodic response.

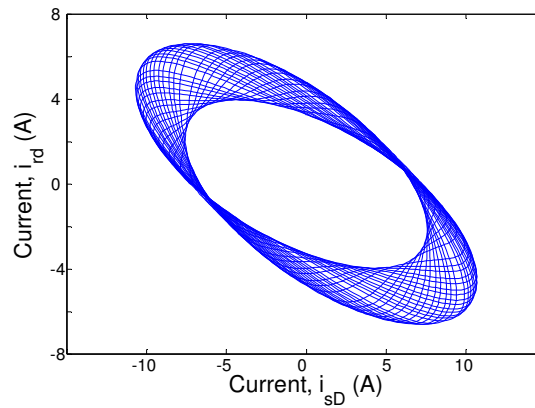


Figure 6.20 Phase plane diagram for  $\omega_r = 335.1 \text{ rad/s}$  – Quasi-periodic response.

### 6.3 STABILITY ANALYSIS

The numerical results presented in the above sections show that as a system parameter is varied, the SEIG undergoes a Neimark bifurcation characterised by the transition from a stable period-one orbit to a quasi-periodic orbit. In this section, both orbits are analysed to establish the stability properties of the system.

A discrete-time nonlinear system can be expressed in the following general form

$$\mathbf{x}_{n+1} = f(\mathbf{x}_n), \quad n = 0, 1, 2, \dots \quad (6.1)$$

As discussed in Chapter Three, three steps are needed to establish the stability of the system's limit sets: locating the fixed points of the system (if  $\mathbf{x}_{n+1} = \mathbf{x}_n = \mathbf{x}^*$ , then  $\mathbf{x}^*$  is a fixed point of the above nonlinear expression), locally linearising the discrete system in the neighbourhood of the fixed point to obtain the Jacobian matrix; and finally calculating the eigenvalues of the Jacobian matrix [70]. A fixed point is stable if all the eigenvalues of the Jacobian matrix have magnitude(s) less than unity and unstable otherwise.

As the SEIG system is simulated as a four-dimensional (stator and rotor  $d$ - $q$  axis currents respectively) continuous-time system, it is essential to transform the fourth order system's equation to a lower order discrete-time form. This is achieved by sampling the state vectors when the stator  $d$  axis current ( $i_{sd}$ ) is zero. The resulting three-dimensional discrete-time system is derived as follows [67]

$$\mathbf{I}_{n+1} = \mathbf{A}\mathbf{I}_n \quad (6.2)$$

$$\mathbf{I}_{n+1} = \begin{bmatrix} i_{sQn+1} \\ i_{rdn+1} \\ i_{rqn+1} \end{bmatrix}, \quad \mathbf{A} = \begin{bmatrix} A_{11} & A_{12} & A_{13} \\ A_{21} & A_{22} & A_{23} \\ A_{31} & A_{32} & A_{33} \end{bmatrix}, \quad \mathbf{I}_n = \begin{bmatrix} i_{sQn} \\ i_{rdn} \\ i_{rqn} \end{bmatrix} \quad (6.3)$$

where  $\mathbf{A}$  is the Jacobian matrix and  $\mathbf{I}_n, \mathbf{I}_{n+1}$  are stator and rotor current state vectors at states  $n$  and  $n + 1$ , respectively.

### 6.3.1 ANALYSIS OF THE PERIOD-ONE ORBIT

Taking our base case ( $R = 30 \Omega$ ,  $C = 135 \mu F$  and  $\omega_r = 314 \text{ rad/s}$ ) as an example of a stable period-one operating point, the phase plane diagram of stator  $d$ - $q$  axis currents in the continuous-time domain is a limit cycle (as shown in Figure 6.2). In discrete time domain, the Poincaré section represented by the sampled rotor  $d$  axis versus stator  $q$  axis current is a single dot (Figure 6.21).

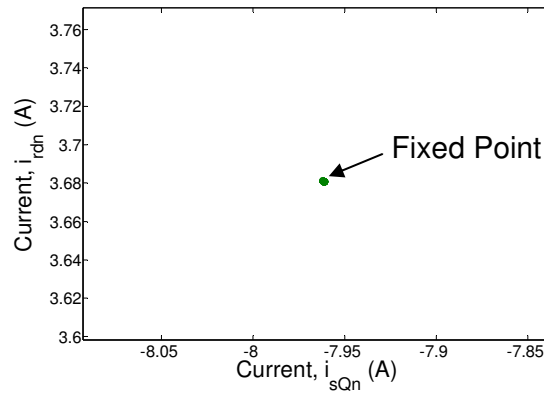


Figure 6.21 Period-one Poincaré section; Base case without disturbance.

Figure 6.22 shows the phase plane diagram of the system when a pulse disturbance is applied to the state vector  $i_{sD}$  at  $3.303 \text{ s}$  (when  $i_{sD}$  is at its maximum positive magnitude). The pulse signal is added to the system while operating in steady-state for a duration of less than one period of the stator current waveform. The resulting Poincaré section is shown in Figure 6.23. From a graphical point of view, Figure 6.23 shows that the fixed point is stable since the system dynamics iterates spirally to it.

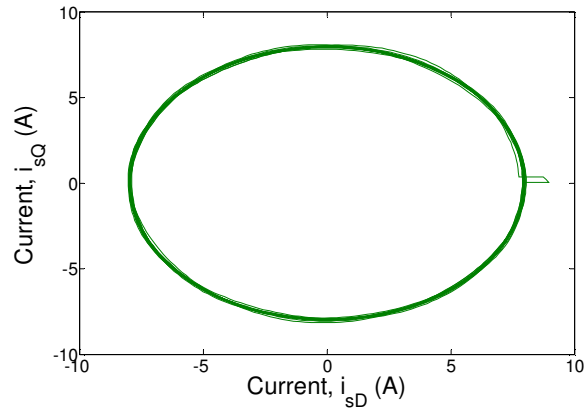


Figure 6.22 Period-one phase plane diagram; Base case with disturbance.

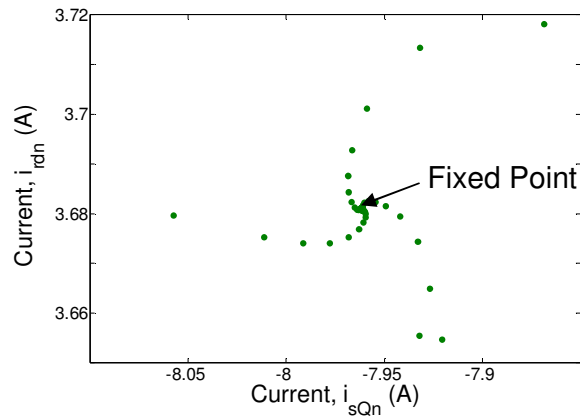


Figure 6.23 Period-one Poincaré section; Base case with disturbance.

Mathematically, the stability analysis of the above fixed point is carried out by sampling the three state variables  $i_{sQ}$ ,  $i_{rd}$  and  $i_{rq}$  when  $i_{sD} = 0$ . Eight sampled points are shown in Table 6.1 with a full list of sampled points given in Appendix E for further details.

Table 6.1 Sampled  $i_{sQ}$ ,  $i_{rd}$  and  $i_{rq}$  state variables when  $i_{sD} = 0$ .

Sampled Currents when $i_{sD} = 0$			
No.	$i_{sQ}$ (A)	$i_{rd}$ (A)	$i_{rq}$ (A)
1	-8.1589	3.728	3.3504
2	-7.9206	3.6547	3.0984
3	-7.8688	3.7182	3.124
4	-8.0576	3.6797	3.2406
5	-7.9323	3.6556	3.1225
6	-7.9322	3.7134	3.1815
7	-8.0115	3.6753	3.2064
8	-7.927	3.6649	3.1307

According to equation (6.2) and (6.3), the first Jacobian matrix  $A_1$  can be calculated from the first four sets of sampled data (samples no. 1, 2, 3 and 4). Followed by matrix  $A_2$  derived from samples no. 2, 3, 4 and 5, and so on for matrices  $A_3$ ,  $A_4$  and  $A_5$

$$\begin{cases} I_2 = A_1 I_1 \\ I_3 = A_1 I_2 \\ I_4 = A_1 I_3 \end{cases}$$

$$\begin{cases} I_3 = A_2 I_2 \\ I_4 = A_2 I_3 \\ I_5 = A_2 I_4 \end{cases}$$

⋮

$$\begin{cases} I_6 = A_5 I_5 \\ I_7 = A_5 I_6 \\ I_8 = A_5 I_7 \end{cases} \quad (6.4)$$

By substituting the sampled data (shown in Table 6.1) into equation (6.4), Jacobian matrices, the eigenvalues of each derived matrix and the magnitude of the complex conjugates can be computed as shown in Table 6.2 (more Jacobian matrices are shown in Appendix E).

Table 6.2 The Jacobian matrix, eigenvalue and magnitude of the complex conjugates derived from the sampled state variables under period-one orbit condition.

	Jacobian Matrix	Eigenvalue	Magnitude of the complex conjugates
A <sub>1</sub>	-0.2045 -2.9971 0.4729	0.9992	0.7816
	-0.6961 0.3722 -1.0185	-0.5902 + j0.5124	
	0.2770 1.7509 -0.3490	-0.5902 - j0.5124	
A <sub>2</sub>	-0.3195 -2.5923 -0.2986	0.9993	0.8722
	-0.7269 0.4806 -1.2250	-0.3990 + j0.7756	
	0.3350 1.5467 0.0403	-0.3990 - j0.7756	
A <sub>3</sub>	0.2384 -2.2622 0.7138	0.9994	0.9099
	-0.8798 0.3901 -1.5024	-0.6842 + j0.5998	
	-0.2369 1.2083 -0.9975	-0.6842 - j0.5998	
A <sub>4</sub>	0.3086 -2.1547 0.7663	0.9997	0.8233
	-0.6682 0.7139 -1.3440	-0.4480 + j0.6907	
	-0.1319 1.3690 -0.9189	-0.4480 - j0.6907	
A <sub>5</sub>	0.3001 -2.2686 0.8779	0.9999	0.91
	-0.6652 0.7537 -1.3830	-0.5121 + j0.7522	
	-0.1197 1.5314 -1.0781	-0.5121 - j0.7522	

The elements of the Jacobian matrices shown in the second column of Table 6.2 are seen to be similar to each other. Within the eigenvalues column, one of the eigenvalues is always less than unity and the other two eigenvalues are complex conjugates. The magnitude of each complex conjugate is given in the last column of Table 6.2 with all values being less than unity. Therefore, the system is stable according to the stability criteria discussed in Chapter Three. The average values of the three eigenvalues are 0.9995,  $-0.5267 + j0.6661$  and  $-0.5267 - j0.6661$ .

### 6.3.2 ANALYSIS OF THE QUASI-PERIOD ORBIT

The stability of the quasi-period orbit when operating at  $R = 30 \Omega$ ,  $C = 156 \mu F$  and  $\omega_r = 314 \text{ rad/s}$  (Figure 6.7 to Figure 6.10) is analysed in this section.

Figure 6.24 shows the phase plane diagram of the system when a pulse disturbance is applied to the stator  $d$  axis vector at  $3.303 \text{ s}$ . The Poincaré section of the quasi-period phase plane diagram with such disturbance is plotted in Figure 6.25. From a graphical point of view, the Poincaré section iterates spirally away from the fixed point (in the middle of the limit cycle) and onto a limit cycle. Therefore, the fixed point is unstable according to the stability criteria discussed in Chapter Three.

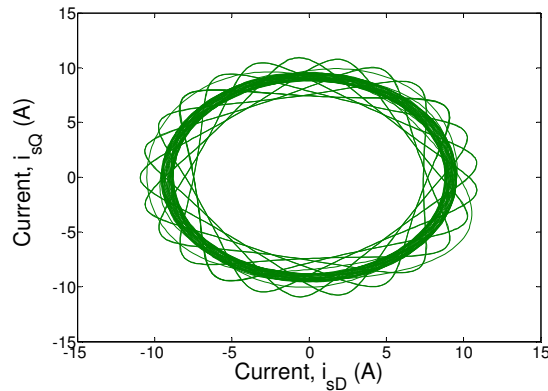


Figure 6.24 Quasi-period phase plane diagram;  $C = 156 \mu F$  with disturbance.

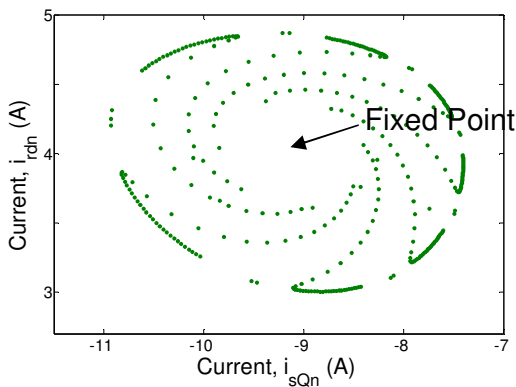


Figure 6.25 Quasi-period Poincaré section;  $C = 156 \mu F$  with disturbance.

A numerical analysis of the stability of the above fixed point is discussed below.

Eight sampled sets of state variables (when  $i_{sD} = 0$ ) are shown in Table 6.3.

Table 6.3 Sampled  $i_{sQ}$ ,  $i_{rd}$  and  $i_{rq}$  state variables when  $i_{sD} = 0$ .

No.	Sampled Currents when $i_{sD} = 0$		
	$i_{sQ}$ (A)	$i_{rd}$ (A)	$i_{rq}$ (A)
1	14.628	0.0897	17.514
2	16.269	3.3017	12.985
3	23.939	4.1968	22.695
4	12.774	2.4027	14.935
5	22.416	0.9226	16.071
6	19.141	2.7468	20.822
7	13.375	3.6334	-13.41
8	27.486	3.2308	21.173

By substituting the sampled data shown in Table 6.3 into equation (6.4), the Jacobian matrices, eigenvalues of each Jacobian matrix and the magnitudes of the complex conjugates derived from the sampled state vectors can be computed as shown in Table 6.4. A full list of the sampled state variables and Jacobian matrices is given in Appendix E.

Table 6.4 The Jacobian matrix, eigenvalue and magnitude of the complex conjugates derived from the sampled state variables under quasi-periodic orbit condition.

	Jacobian Matrix	Eigenvalue	Magnitude of the complex conjugates
$A_1$	0.6162 2.6382 -0.4008 -0.8788 -0.5806 -0.9255 -1.2715 -1.9077 -0.3303	-0.6511 + j0.7495 -0.6511 - j0.7495 1.0074	0.9928
$A_2$	0.1979 2.8269 -0.8769 -0.8263 -0.6043 -0.8658 -1.2378 -1.9229 -0.2920	-0.8532 + j0.7596 -0.8532 - j0.7596 1.008	1.1423
$A_3$	-0.0609 2.6776 -1.1222 -0.5125 -0.4232 -0.5682 -0.7183 -1.6232 0.2006	-0.6387 + j0.6589 -0.6387 - j0.6589 0.9939	0.9177
$A_4$	-0.0125 2.9295 -1.0403 -0.5272 -0.5002 -0.5932 -0.7201 -1.6329 0.1974	-0.6579 + j0.7845 -0.6579 - j0.7845 1.0005	1.0239
$A_5$	-0.2568 3.5431 -1.3458 -0.3422 -0.9648 -0.3618 -0.4837 -2.2268 0.4932	-0.8668 + j0.6264 -0.8668 - j0.6264 1.0051	1.0694

The Jacobian matrices shown in the second column of Table 6.4 are clearly different from each other and not all the eigenvalues have magnitudes of less than unity. The system is clearly unstable according to the stability criteria discussed in Chapter Three. The average values of the three eigenvalues are 1.003,  $-0.7335 + j0.7158$  and  $-0.7335 - j0.7158$ .

### 6.3.3 AN OVERVIEW OF THE MOVEMENT OF EIGENVALUES WHEN CHANGING A CONTROL PARAMETER

A brief overview of the movement of the eigenvalues of the system when changing each of the three control parameters is given in this section. These values were calculated in a similar way to that described above for operating at  $C = 156 \mu F$ ,  $R = 30 \Omega$  and  $\omega_r = 314 \text{ rad/s}$  (Table 6.4).

#### a) Changing the Control Parameter $C$

Figure 6.26 gives an overview of the magnitudes of the eigenvalues of the Jacobian matrices when the self-excitation capacitance is increased from  $151 \mu F$  (blue square) to  $151.7 \mu F$  (purple star) and then to  $160 \mu F$  (green circle) per phase ( $R = 30 \Omega$  and  $\omega_r = 314 \text{ rad/s}$ ). It is noted that the system is stable when the value of  $C$  is smaller than  $151.7 \mu F$  (all eigenvalues are within the unit circle) and unstable for values of  $C$  greater than  $151.7 \mu F$ . In other words, the system transforms from period-one to quasi-period orbit when self-excitation capacitance is around  $151.7 \mu F$  per phase. The following eigenvalue movement map agrees well with the bifurcation diagram shown in Figure 6.3.

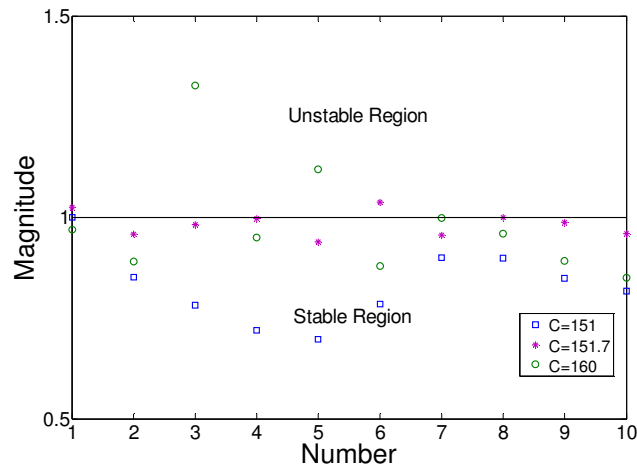


Figure 6.26 Eigenvalue map for changing capacitance.

*b) Changing the Control Parameter R*

Figure 6.27 gives an overview of the magnitudes of the eigenvalues of the Jacobian matrices as the load resistance is reduced from  $30 \Omega$  (blue square) to  $28.8 \Omega$  (purple star) and then  $24 \Omega$  (green circle) per phase ( $C = 135 \mu F$  and  $\omega_r = 314 \text{ rad/s}$ ). The system is stable when the value of  $R$  is greater than  $28.8 \Omega$  (all eigenvalues are within the unit circle) and unstable when  $R$  is smaller than  $28.8 \Omega$ . In other words, the system transforms from period-one to quasi-period orbit when load resistance is around  $28.8 \Omega$  per phase. Again, the following eigenvalue map agrees well with the bifurcation diagram shown in Figure 6.11.

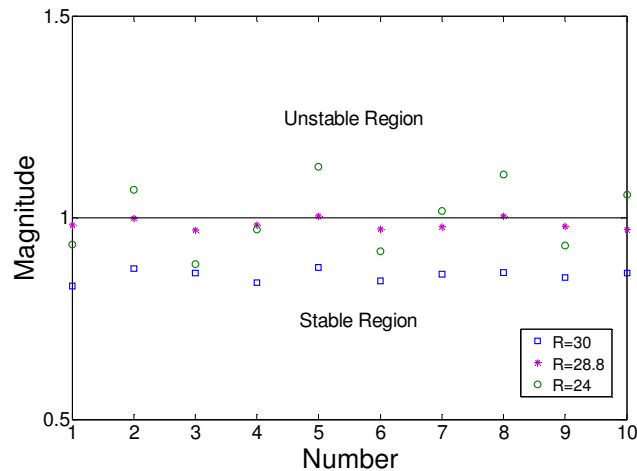


Figure 6.27 Eigenvalue map for changing load resistance.

*c) Changing the Control Parameter  $\omega_r$*

Figure 6.28 gives an overview of the magnitudes of the eigenvalues of the Jacobian matrices as the speed of the rotor is increased from  $314 \text{ rad/s}$  (blue square) to  $334.2 \text{ rad/s}$  (purple star) and then to  $336 \text{ rad/s}$  (green circle) ( $R = 30 \Omega$  and  $C = 135 \mu F$ ). The system is stable when the value of  $\omega_r$  is smaller than  $334.2 \text{ rad/s}$  (all eigenvalues are within the unit circle) and unstable when  $\omega_r$  is greater than  $334.2 \text{ rad/s}$ . In other words, the system transforms from period-one to quasi-period orbit when shaft speed is around  $334.2 \text{ rad/s}$ . The stability analysing results (shown in Figure 6.28) agree well with the bifurcation diagram shown in Figure 6.16.

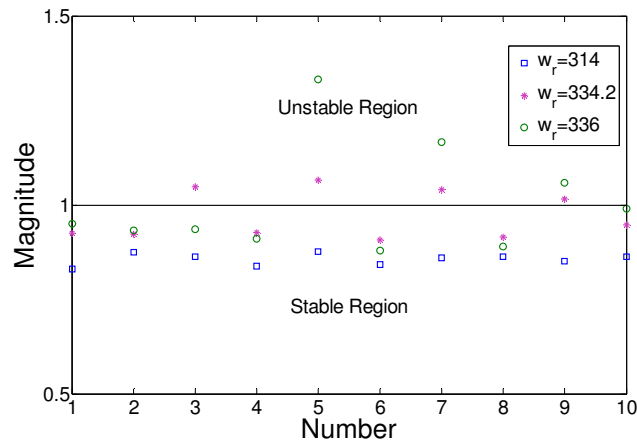


Figure 6.28 Eigenvalue map for changing rotor speed.

## 6.4 SUMMARY

The nonlinear behaviour of the SEIG and its stability characteristic when operating under inductive load ( $RL$ ) conditions was analysed and investigated in detail with the aid of computer simulations and relevant numerical analysis tools in this chapter.

The analysis showed how the SEIG autonomous dynamic system loses its period-one stability to a quasi-periodic orbit and eventual chaotic behaviour as a result of small changes in the system parameters. Three control parameters were used to examine the nonlinear behaviour of the machine: the value of the self-excitation capacitors, shaft speed and load resistance.

The stability of the period-one and quasi-period orbits was analysed by both graphical and numerical means and an overview of the movement of the eigenvalues of the system's Jacobian matrices was presented showing the boundaries between stable and unstable regions of operation. The results of the stability analysing match well with the system bifurcation diagrams drawn with the self-excitation capacitance, load resistance and rotor speed as bifurcation parameters.

# CHAPTER 7

## CONCLUSIONS AND FUTURE WORK

### 7.1 CONCLUSIONS

The thesis carried out a detailed review of the nonlinear computer modelling techniques of induction machines based on the cross-saturation effect, leakage saturation effect, the machine H-G diagram and skin effect. It was proved that the cross-saturation nonlinear effect is the most accurate nonlinear modelling technique of induction machines. Hence, the dynamic behaviour of the SEIG system when feeding variable load conditions is analysed and investigated throughout this thesis with the consideration of cross-saturation nonlinear effect.

The thesis was focused on analysing the steady-state nonlinear behaviour of the SEIG as a nonlinear dynamic system, unlike most of the researchers/scientists carried out the analysis of the steady-state and transient performance of SEIGs from design and operational point of view.

The features of an induction generator in terms of cost and simplicity offer many advantages in today's renewable energy industry. The limitation of an induction generator in needing an external reactive power source to provide the machine magnetisation can be overcome by connecting a three-phase capacitor bank to its stator terminals. This capacitor bank supplies reactive power to both the generator and the load, and the real power demand of the terminal load is supplied by the prime mover.

A brief introduction to nonlinear dynamic systems, Poincaré maps, bifurcation diagrams, limit sets and their stability characteristics was also given in this thesis. This serves as a general mathematical background of nonlinear systems and provides the analytical tools required to investigate the SEIG as a nonlinear dynamic system.

The modelling of the induction generator as a linear electromagnetic device was introduced as the foundation for further study and investigation of the nonlinear behaviour of the SEIG. A model of the machine with consideration of the cross-saturation effect was then derived by modifying the standard machine model. A current based implementation of the machine state space model (with currents as state space variables) was used in this thesis because of its ease of simulation in Simulink.

A mathematical model of the SEIG when operating as a standalone device was then created by including the self-excitation capacitor bank and the load impedance, connection in parallel with the stator terminals. The model was verified by comparison with experimental results presented in a well-known publication and by comparison with laboratory test results obtained for a 1.1 kW induction machine feeding various types of load.

Laboratory testing of the SEIG when feeding no-load, a purely resistive load ( $R$ ) and an inductive load ( $RL$ ) was carried out to validate the SEIG model developed previously. The experimental results showed good agreement with those generated from the Simulink model and demonstrated the linear and nonlinear types of behaviours of the system when feeding various load types.

The magnetising inductance and the dynamic inductance curves of the induction machine play an important role in modelling the SEIG system and allowing for the cross-saturation effect. In this study, these parameters were obtained by measuring the magnetisation characteristics of the machine while operating at synchronous speed with no-load.

The nonlinear behaviour of the SEIG when operating under inductive load ( $RL$ ) conditions was then analysed and investigated with the aid of computer simulations and relevant numerical analysis tools. The results of the analysis show how the SEIG autonomous dynamic system loses its period-one stability to a quasi-periodic orbit leading eventually to chaotic behaviour as a result of small changes in system parameters. Three control parameters were used to examine the nonlinear behaviour of the machine: the value of the self-excitation capacitors, shaft speed and load resistance.

The stability of the period-one and quasi-period orbits was analysed by using both graphical and numerical means and an overview of the movement of the eigenvalues of the system's Jacobian matrices was presented showing the boundaries between stable and unstable regions of operation. The stability analysis results match well with the numerical simulations and system bifurcation diagrams drawn with the self-excitation capacitance, load resistance and rotor speed as bifurcation parameters.

The results showed how the parameter values of the SEIG determine the dynamic behaviours of the system. A small quantitative change in one of the parameters can directly cause a big qualitative change in system's behaviour. This behaviour is typical of nonlinear dynamic systems. As far as I am aware, this thesis presented the first examination of the periodic, quasi-periodic and chaotic behaviour of the SEIG when supplying variable load types. Laboratory testing and the numerical analysis results confirmed that by changing a parameter of the system such as the inductive load, self-excitation capacitance, rotor shaft speed or the power factor of the load, the behaviour of the system can change dramatically, exhibiting characteristics typical of nonlinear systems.

Numerical simulations and analytical analysis showed how the SEIG lost its stability moving from a stable period-one response, to a quasi-periodic response and chaos through a Neimark bifurcation.

Two induction machines were used in this investigation. A 1.1 kW machine utilised in the experimental rig and a second 1.5 kW machine whose parameters were used as the basis for the analytical investigation of system performance. Unfortunately, using the 1.1 kW laboratory machine as the basis for the analytical study proved problematic because of the very narrow window of quasi-periodic behaviour presented by the machine. This explains why it was virtually impossible to capture a clear quasi-periodic response under laboratory conditions. It also made the task of demonstrating the transition in system behaviour from a stable period-one response to quasi-periodicity and chaos through simulation and analysis of the system eigenvalues very difficult. Hence a decision was taken to use the parameters of a bigger 1.5 kW machine as the basis for the analytical investigation.

## 7.2 FUTURE WORK

The analysis and explanations presented in this thesis provide a good foundation for further research in the area of SEIG systems driven by renewable energy source prime movers. Some of the challenging but worthwhile areas in which this research can be used and exploited for future work are

- Implementation of a wind/hydro turbine as the prime mover of the SEIG system by replacing the existing DC motor of the experimental apparatus. As wind/hydro turbines having constant changing nature, the highly dynamic behaviour of the SEIG system shall be further analysed and investigated by adding nonlinear elements into the system.
- Implementation of a parallel connected SEIG system (typical for wind farm applications) by both computer simulations and experimental testing.
- Development of nonlinear control strategies as the basis for implementing a practical nonlinear controller for the SEIG. The purpose of such a controller would be to control the unstable output of the SEIG by adopting nonlinear control techniques based on the placement of system eigenvalues in order to achieve constant voltage and frequency output over a much wider range of parameter values. Such controllers have been proposed for other electrical systems with varying degrees of success.

# APPENDICES

## APPENDIX A

### THE SUB-BLOCKS OF THE STANDARD INDUCTION MACHINE MODEL

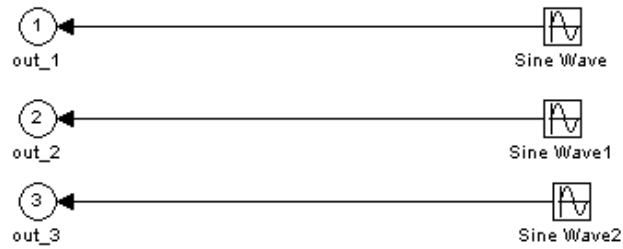


Figure A.1 Stator/Rotor 3-phase Supply sub-block.

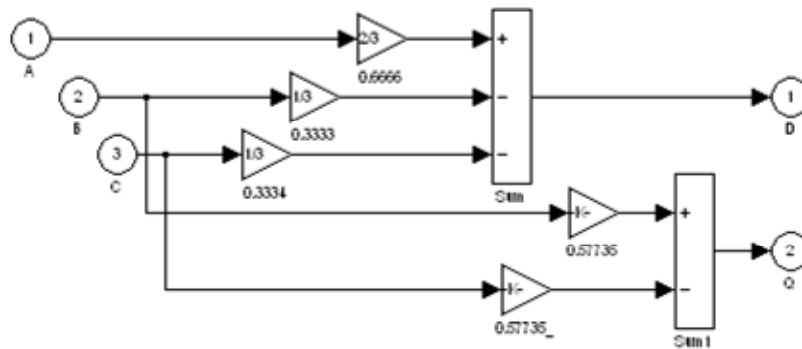


Figure A.2 3-Phase to  $d$ - $q$  sub-block.

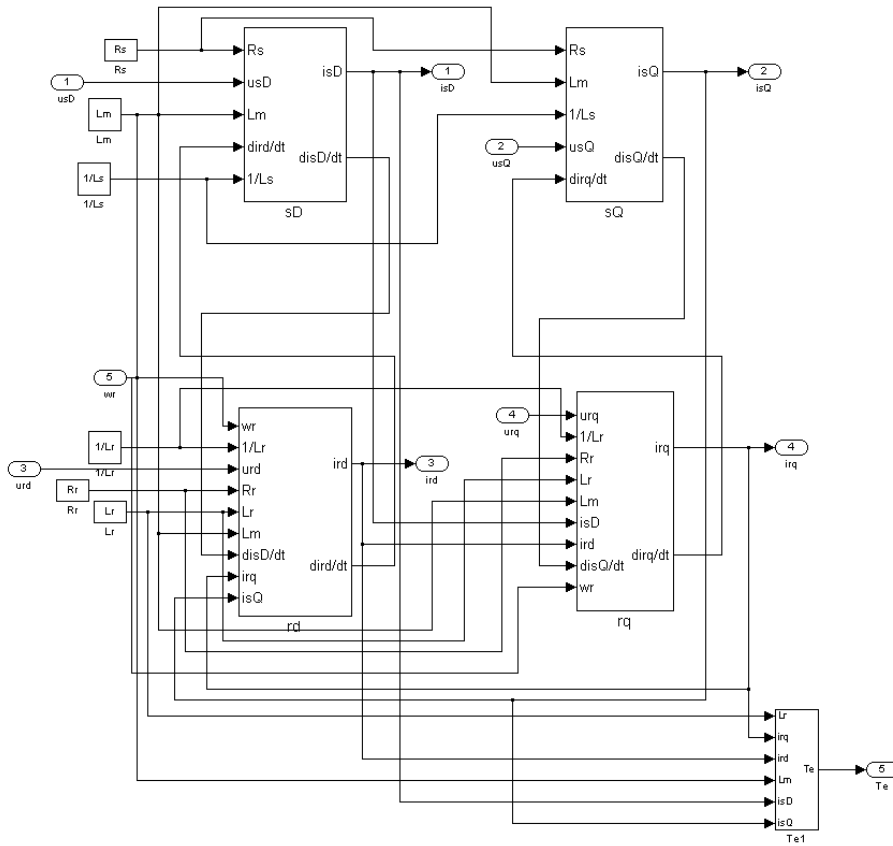
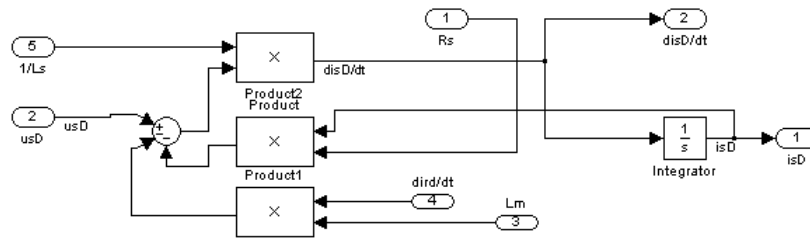
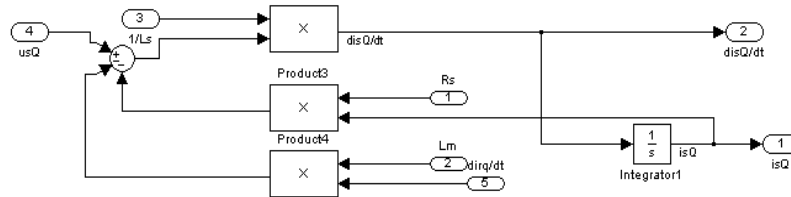


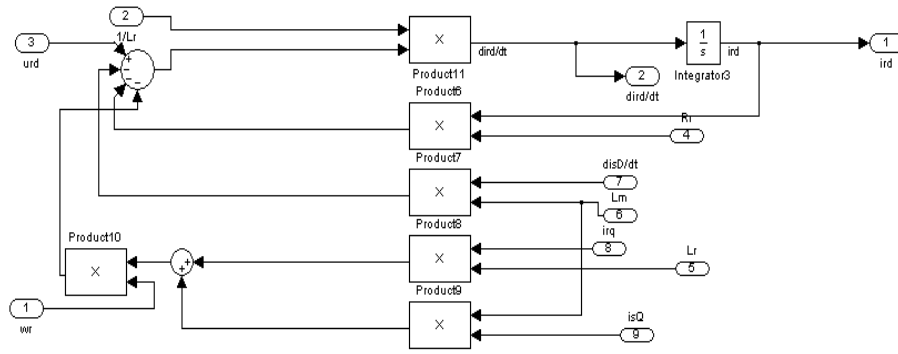
Figure A.3 Induction Machine sub-block.



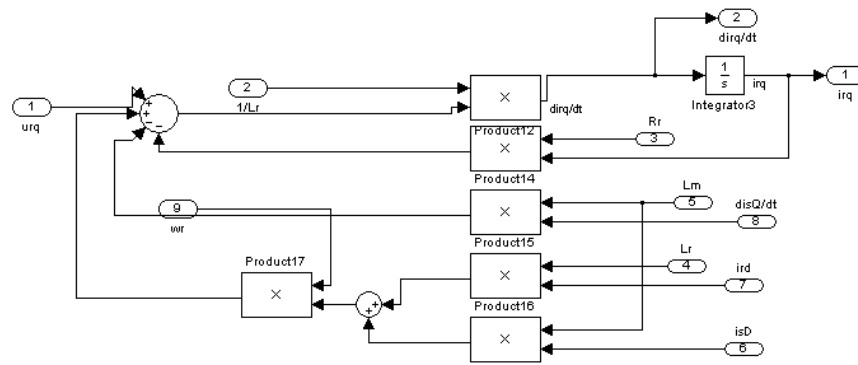
a)  $sD$  Subsystem.



b)  $sQ$  Subsystem.



c)  $rd$  Subsystem.



d)  $rq$  Subsystem.

Figure A.4 Internal view of  $sD$ ,  $sQ$ ,  $rd$  and  $rq$  sub-blocks.

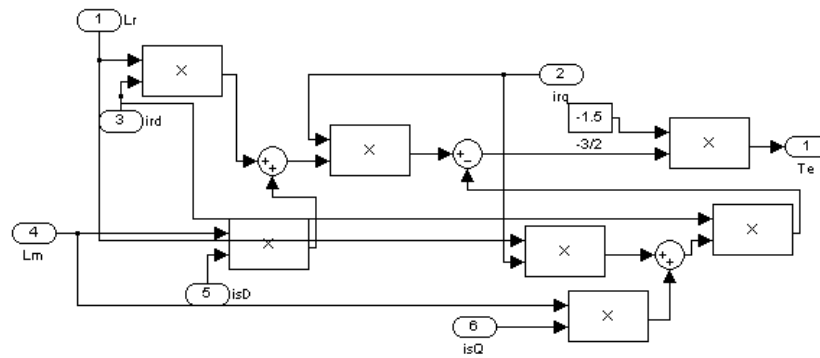


Figure A.5 Internal view of  $T_e$  sub-block.

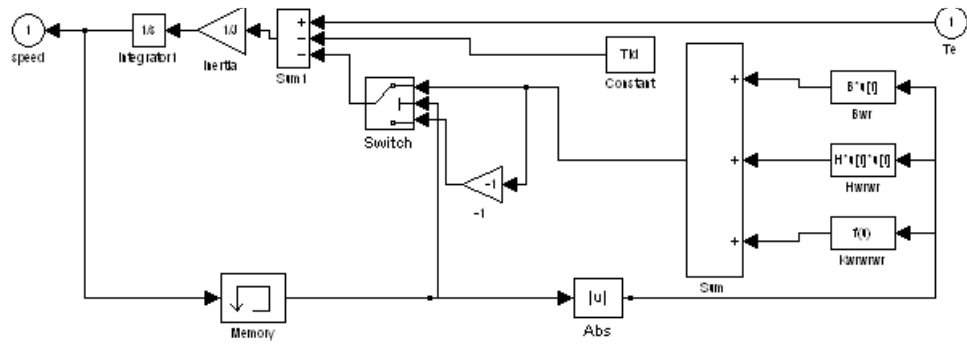


Figure A.6 Mechanical Dynamics sub-block.

## APPENDIX B

### MODELLING OF LEAKAGE SATURATION EFFECTS

This section shows to the reader the process of modelling the IM with consideration of the leakage saturation effects. **Note:** This model is only applicable to large inrush currents. The model is based on the flux linkages as state space variables.

#### B.1 Mathematical Equations of Leakage Saturation Effects

The mathematical equations of a saturable leakage reactance IG are shown as follows (referred to SRF)

Again the general form of IM can be rewritten into equation (B.1)

$$\begin{cases} U_{sd} = R_s i_{sd} + \frac{d\psi_{sd}}{dt} \\ U_{sq} = R_s i_{sq} + \frac{d\psi_{sq}}{dt} \\ U_{rd} = R_r i_{rd} + \frac{d\psi_{rd}}{dt} + \omega_r \psi_{rq} \\ U_{rq} = R_r i_{rq} + \frac{d\psi_{rq}}{dt} - \omega_r \psi_{rd} \end{cases} \quad (\text{B.1})$$

The voltages  $U_{sd}$  and  $U_{sq}$  represent the applied stator voltages in the orthogonal coordinate system. The voltages  $U_{rd}$  and  $U_{rq}$  are the rotor voltages which identically equal to zero when the machine rotor windings are shorted.

$$\begin{cases} \psi_{sd} = L_s i_{sd} + L_m i_{rd} = L_{ls} i_{sd} + L_m (i_{sd} + i_{rd}) \\ \psi_{sq} = L_s i_{sq} + L_m i_{rq} = L_{ls} i_{sq} + L_m (i_{sq} + i_{rq}) \\ \psi_{rd} = L_r i_{rd} + L_m i_{sd} = L_{lr} i_{rd} + L_m (i_{sd} + i_{rd}) \\ \psi_{rq} = L_r i_{rq} + L_m i_{sq} = L_{lr} i_{rq} + L_m (i_{sq} + i_{rq}) \end{cases} \quad (\text{B.2})$$

where  $L_{ls}$ ,  $L_{lr}$  and  $L_m$  are leakage stator/rotor inductances and mutual inductance, respectively.

$$\begin{cases} L_{ls} = L_{lsa} + L_{lsi} \\ L_{lr} = L_{lra} + L_{lri} \end{cases} \quad (\text{B.3})$$

where  $L_{lsa}$ ,  $L_{tra}$  and  $L_{lsi}$ ,  $L_{lri}$  are stator/rotor air and iron leakage inductance, respectively. The stator/rotor leakage inductances are now assumed to be comprised of both iron-dependant slot and air-dependant end winding portions. The former one is saturable and the latter one is constant.

The  $d$ - $q$  axis mutual fluxes which link both stator and rotor are given by

$$\begin{cases} \psi_{md} = L_m (i_{sd} + i_{rd}) \\ \psi_{mq} = L_m (i_{sq} + i_{rq}) \end{cases} \quad (\text{B.4})$$

Since

$$\begin{cases} \psi_{lds} = L_{lsa} i_{sd} \\ \psi_{lqs} = L_{lsa} i_{sq} \\ \psi_{ldr} = L_{tra} i_{rd} \\ \psi_{lqr} = L_{tra} i_{rq} \end{cases} \quad (\text{B.5})$$

where  $\psi_{lds}$ ,  $\psi_{lqs}$ ,  $\psi_{ldr}$  and  $\psi_{lqr}$  are stator/rotor  $d$ - $q$  axis air dependant leakage flux linkages, respectively.

Substitute equations (B.3), (B.4) and (B.5) into (B.2) and solve for the four machine currents, it is possible to write the result as

$$\begin{cases} i_{sd} = (\psi_{sd} - \psi_{md\_sat} - \psi_{ldsi\_sat}) / L_{lsa} \\ i_{sq} = (\psi_{sq} - \psi_{mq\_sat} - \psi_{lqsi\_sat}) / L_{lsa} \\ i_{rd} = (\psi_{rd} - \psi_{md\_sat} - \psi_{ldri\_sat}) / L_{tra} \\ i_{rq} = (\psi_{rq} - \psi_{mq\_sat} - \psi_{lqri\_sat}) / L_{tra} \end{cases} \quad (\text{B.6})$$

where  $\psi_{md\_sat}$  and  $\psi_{mq\_sat}$  are saturated  $d$ - $q$  axis mutual flux linkages;  $\psi_{ldsi\_sat}$ ,  $\psi_{lqsi\_sat}$ ,  $\psi_{ldri\_sat}$  and  $\psi_{lqri\_sat}$  are saturated stator/rotor  $d$ - $q$  axis iron dependant leakage flux linkages, respectively.

Substitute equation (B.6) into (B.1)

$$\begin{cases} \frac{d\psi_{sd}}{dt} = U_{sd} - \frac{R_s}{L_{lsa}}(\psi_{sd} - \psi_{md\_sat} - \psi_{ldsi\_sat}) \\ \frac{d\psi_{sq}}{dt} = U_{sq} - \frac{R_s}{L_{lsa}}(\psi_{sq} - \psi_{md\_sat} - \psi_{lqsi\_sat}) \\ \frac{d\psi_{rd}}{dt} = U_{rd} - \frac{R_r}{L_{lra}}(\psi_{rd} - \psi_{md\_sat} - \psi_{ldri\_sat}) - \omega_r \psi_{rq} \\ \frac{d\psi_{rq}}{dt} = U_{rq} - \frac{R_r}{L_{lra}}(\psi_{rq} - \psi_{md\_sat} - \psi_{lqri\_sat}) + \omega_r \psi_{rd} \end{cases} \quad (B.7)$$

In order to solve these equations completely, independent expressions for the saturated values of the magnetising and iron-dependent leakage fluxes must be developed. That is to substitute equation (B.6) into (B.4) using the unsaturated values of mutual flux linkages, equation (B.8) is derived by

$$\begin{cases} \psi_{md\_unsat} = L_m^* \psi_{sd} / L_{lsa} + L_m^* \psi_{rd} / L_{lra} + L_m^* \left( \frac{1}{L_{lsa}} + \frac{1}{L_{lra}} \right) \Delta \psi_{md} - L_m^* \psi_{ldsi\_sat} / L_{lsa} - L_m^* \psi_{ldri\_sat} / L_{lra} \\ \psi_{mq\_unsat} = L_m^* \psi_{sq} / L_{lsa} + L_m^* \psi_{rq} / L_{lra} + L_m^* \left( \frac{1}{L_{lsa}} + \frac{1}{L_{lra}} \right) \Delta \psi_{mq} - L_m^* \psi_{lqsi\_sat} / L_{lsa} - L_m^* \psi_{lqri\_sat} / L_{lra} \end{cases} \quad (B.8)$$

where  $\psi_{md\_unsat}$  and  $\psi_{mq\_unsat}$  are unsaturated  $d$ - $q$  axis mutual flux linkages

$$L_m^* = \frac{1}{[1/L_{m\_unsat} + 1/L_{lsa} + 1/L_{lra}]} \quad (B.9)$$

When unsaturated, the stator/rotor  $d$  -  $q$  axis iron-dependant leakage flux linkages  $\psi_{ldsi\_unsat}$ ,  $\psi_{lqsi\_unsat}$ ,  $\psi_{ldri\_unsat}$  and  $\psi_{lqri\_unsat}$  are

$$\begin{cases} \psi_{ldsi\_unsat} = L_{lsi\_unsat} i_{sd} \\ \psi_{lqsi\_unsat} = L_{lsi\_unsat} i_{sq} \\ \psi_{ldri\_unsat} = L_{lri\_unsat} i_{rd} \\ \psi_{lqri\_unsat} = L_{lri\_unsat} i_{rq} \end{cases} \quad (B.10)$$

By substituting equation (B.6) into (B.10) and using unsaturated values of flux linkages, the iron-dependant leakage flux is computed by

$$\left\{ \begin{array}{l} \psi_{ldsi\_unsat} = \frac{L_{ls}^*}{L_{lsa}} [\psi_{sd} + \Delta\psi_{ldsi\_sat} - \psi_{md\_sat}] \\ \psi_{lqsi\_unsat} = \frac{L_{ls}^*}{L_{lsa}} [\psi_{sq} + \Delta\psi_{lqsi\_sat} - \psi_{mq\_sat}] \\ \psi_{ldri\_unsat} = \frac{L_{lr}^*}{L_{lra}} [\psi_{rd} + \Delta\psi_{ldri\_sat} - \psi_{md\_sat}] \\ \psi_{lqri\_unsat} = \frac{L_{lr}^*}{L_{lra}} [\psi_{rq} + \Delta\psi_{lqri\_sat} - \psi_{mq\_sat}] \end{array} \right. \quad (B.11)$$

$$\text{where, } \left\{ \begin{array}{l} L_{ls}^* = \frac{1}{[1/L_{lsa} + 1/L_{lsi\_unsat}]} \\ L_{lr}^* = \frac{1}{[1/L_{lra} + 1/L_{lri\_unsat}]} \end{array} \right. \quad (B.12)$$

The saturated values of magnetising and iron-dependent leakage flux linkages can now be determined by means of saturation factors.

**Note:**

$$\psi_{m\_unsat} = \sqrt{\psi_{md\_unsat}^2 + \psi_{mq\_unsat}^2}$$

$$\Delta\psi_{m\_sat} = K_m \psi_{m\_unsat}$$

$$\Delta\psi_{md\_sat} = K_m \psi_{md\_unsat}$$

$$\Delta\psi_{mq\_sat} = K_m \psi_{mq\_unsat}$$

$$\psi_{md\_sat} = \psi_{md\_unsat} - \Delta\psi_{md\_sat}$$

$$\psi_{mq\_sat} = \psi_{mq\_unsat} - \Delta\psi_{mq\_sat}$$

$$\psi_{lsi\_unsat} = \sqrt{\psi_{lqsi\_unsat}^2 + \psi_{ldsi\_unsat}^2}$$

### B.2 Simulation Results of Leakage Saturation Effects

The machine parameters are: stator and rotor resistance  $R_s = 0.4122 \Omega$ ,  $R_r = 0.4976 \Omega$ , magnetising reactance  $X_{m\_unsat} = 15.7 \Omega$ , stator and rotor air dependant leakage reactance  $X_{lsa}, X_{lra} = 0.15 \Omega$ , stator and rotor iron dependant leakage reactance  $X_{lsi\_unsat}, X_{lri\_unsat} = 0.95 \Omega$  and Rotor inertia  $J = 0.11 \text{ kgm}^2$  [58].

Block functions defined in the program

$$L_{mz} = \frac{1}{1/L_{m\_unsat} + 1/L_{lsa} + 1/L_{lra}} \quad (\text{B.13})$$

$$L_{laz} = \frac{1}{1/L_{lsa} + 1/L_{lra}} \quad (\text{B.14})$$

$$L_{lsz} = \frac{1}{[1/L_{lsa} + 1/L_{lsi\_unsat}]} \quad (\text{B.15})$$

$$L_{lrz} = \frac{1}{[1/L_{lra} + 1/L_{lri\_unsat}]} \quad (\text{B.16})$$

where  $a = L_{mz} / L_{laz}$ ,  $b = L_{mz} / L_{lsa}$ ,  $c = L_{mz} / L_{lra}$ ,  $d = L_{lsz} / L_{lsa}$ ,  $g = R_s / L_{lsa}$ ,  $k = L_{lrz} / L_{lra}$ ,  $n = R_r / L_{lra}$ ,  $p = 1 / L_{lsa}$ ,  $q = 1 / L_{lra}$ ,  $r = 3pp / 4$  and  $s = 1 / J$ .

**Note:**  $pp$  is pole pair of the machine.

The leakage saturation induction machine Simulink model uses 'data store write', 'data store read' and 'data store memory' blocks to store and transfer data.

The simulation results of the IG when feeding no-load are shown as follows

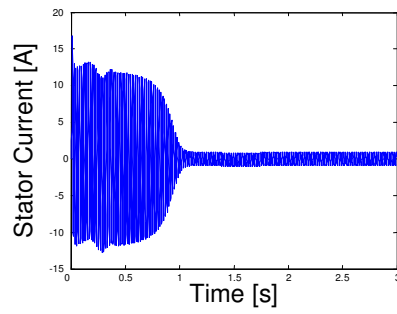


Figure B.1 Induction machine stator current at no-load.

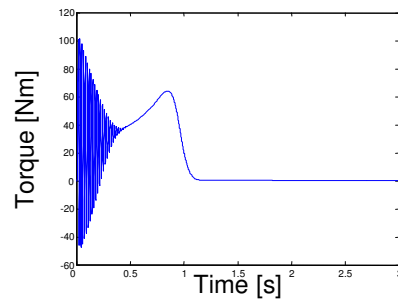


Figure B.2 Induction machine torque response at no-load.

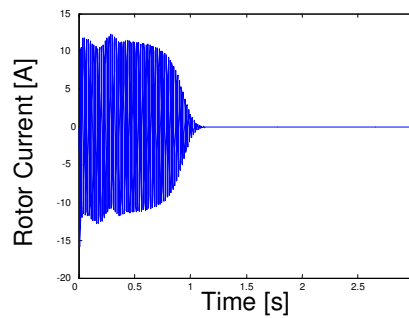


Figure B.3 Induction machine rotor current at no-load.

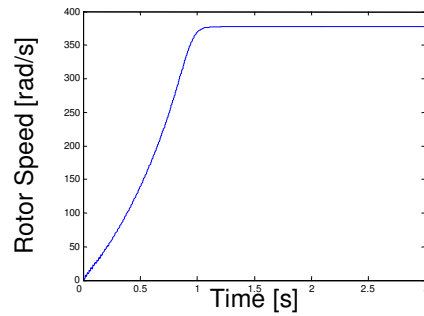


Figure B.4 Induction machine rotor speed at no-load.

The stator and rotor current waveforms as well as the torque and the rotor speed response curves are in good agreement with the general characteristics of an induction machine. The leakage saturable technique is only suitable for when large inrush current occurs in the machine. The cross-saturation nonlinear effect shall be included in this leakage saturation induction machine Simulink model if it is necessary to be investigated further for high power machine applications.

## APPENDIX C

### THE ELECTRICAL EQUIVALENT CIRCUIT TESTS OF THE INDUCTION MACHINE

The parameters of the EC for the IM are crucial for running the simulation models. The most common way to manually determine the IM parameters are to use the No-load test and Blocked rotor test. The data gained from these two tests are then transformed to EC parameters through a series of mathematical equations shown in the following section.

The induction machine used for testing is an ABB 2-pole, squirrel cage, Class A induction machine with 1.1 kW rated power, 220~240/380~420 V rated voltage, 4.4/2.5 A rated current and 50 Hz rated frequency.

**Note:** Class A Squirrel-Cage Induction Motor characterised by normal starting torque, high starting current, low operating slip, low rotor impedance, good operating characteristics at the expense of high starting current, common applications include fans, blowers and pumps.

#### *C.1 No-load Test (50 Hz)*

No-load test of the IM is introduced to the reader in this section. The No-load test is just like the open circuit test of a transformer, it gives information on excitation current and rotational losses. The procedures of the No-load test are: three-phase balanced supply voltages are firstly applied to the stator terminals at the rated frequency with the rotor uncoupled from any mechanical load; then the values of current, voltage and power are measured at the machine's input channels, the machine rotates at almost synchronous speed with slip near zero. The measured values are shown in Table C.1.

Table C.1 Measured data during No-load test.

No-load Test	
$I_{nl}$	1.39 A
$V_{nl}$	417.67 V
$P_{nl}$	150 W
$f_s$	50 Hz

### C.2 Blocked Rotor Test (12.5 Hz)

The blocked rotor test is just like the short circuit test of a transformer. It provides information on leakage impedances and the rotor resistance. The procedures of the Blocked rotor test are: Firstly, the rotor needs to be blocked to prevent rotation; secondly, when the rotor is at the stand still, the balanced supply voltages are applied to the stator terminals at a frequency of 25% of the rated value at a voltage when the rated current is achieved; finally, the values of current, voltage and power are measured at the machine's input channels. The measured values are shown in Table C.2.

Table C.2 Measured data during Locked rotor test.

Locked Rotor Test	
$I_{br}$	2.54 A
$V_{br}$	90.65 V
$P_{br}$	276.67 W
$f_s$	12.5 Hz

### C.3 The Equivalent Circuit Calculation

From the no-load measurement data  $I_{nl}, V_{nl}, P_{nl}$ , the value of the core resistance is determined.

The single phase values of the no-load power and voltage

$$P_{nl-1} = \frac{P_{nl}}{3} = \frac{150}{3} = 50 \text{ W}$$

$$V_{nl-In} = \frac{V_{nl}}{\sqrt{3}} = \frac{417.67}{\sqrt{3}} = 241.14 \text{ V}$$

The value of the core resistance is

$$R_c = \frac{P_{nl-1}}{I_{nl}^2} = \frac{50}{1.39^2} = 25.88 \Omega$$

The ratio of the no-load phase voltage to current represents the no-load impedance, which is

$$Z_{nl} = \frac{V_{nl-In}}{I_{nl}} = \frac{241.14}{1.39} = 173.48 \Omega$$

The value of the magnetising reactance can be determined as follows

$$X_m = j\sqrt{Z_{nl}^2 - R_c^2} = j\sqrt{173.48^2 - 25.88^2} = j171.54 \Omega$$

The following equation is the characteristic of the blocked rotor test

$$X_{br} = X_{sta} + X_{rot}R_{br} = R_{sta} + R_{rot}$$

where  $X_{sta}, X_{rot}, R_{sta}$  and  $R_{rot}$  are stator and rotor reactance and resistance, respectively.

Single phase values of blocked rotor power and voltage are

$$P_{br-1} = \frac{P_{br}}{3} = \frac{276.67}{3} = 92.22 \text{ W}$$

$$V_{br-In} = \frac{V_{br}}{\sqrt{3}} = \frac{90.65}{\sqrt{3}} = 52.34 \text{ V}$$

The blocked rotor resistance and impedance values are

$$R_{br} = \frac{P_{br-1}}{I_{br}^2} = \frac{92.22}{2.54^2} = 14.29 \Omega$$

$$Z_{br} = \frac{V_{br-In}}{I_{br}} = \frac{52.34}{2.54} = 20.61 \Omega$$

The value of the blocked rotor reactance is

$$X_{br} = j\sqrt{Z_{br}^2 - R_{br}^2} = j\sqrt{20.61^2 - 14.29^2} = j14.85 \Omega$$

Therefore the following equation is applied

$$X_{sta} = \frac{X_{br}}{2} = j\frac{14.85}{2} = j7.425 \Omega$$

The rotor reactance is derived by

$$X_{rot} = X_{sta} = j7.425 \Omega$$

The stator phase resistance is measured by a simple DC test shown as follows

$$R_{sta} = \frac{4 V}{0.3 A \times 2} = 6.65 \Omega$$

The rotor resistance is

$$R_{rot} = R_{br} - R_{sta} = 14.29 - 6.65 = 7.64 \Omega$$

The stator, magnetic and rotor impedances are

$$Z_{sta} = R_{sta} + jX_{sta} = 6.65 + j7.425$$

$$Z_m = R_c + jX_m = 25.88 + j171.54$$

$$Z_{rot} = \frac{R_{rot}}{s} + jX_{rot} = \frac{7.64}{s} + j7.425$$

The equation of the airgap impedance with regards to the magnetising and rotor impedances is shown as follows

$$\frac{1}{Z_{airgap}} = \frac{1}{Z_m} + \frac{1}{Z_{rot}}$$

As it is mentioned in the no-load test, the slip is almost zero,  $s \rightarrow 0$

Therefore, the rotor impedance tends to infinity

$$Z_{rot} \rightarrow \infty$$

The value of the airgap impedance is equal to the magnetising impedance as shown by

$$Z_{airgap} = Z_m = 25.88 + j171.54$$

Therefore, the total impedance is

$$z_{total} = Z_{sta} + Z_{airgap} = 32.53 + j178.965$$

$$|Z_{total}| = 181.9 \Omega$$

From the above calculation, the stator line current is

$$I_{sta} = \frac{V_{nl\_In}}{|Z_{total}|} = \frac{241.14}{181.9} = 1.3 A$$

Hence, the EC drawing of the IM can be represented as follows

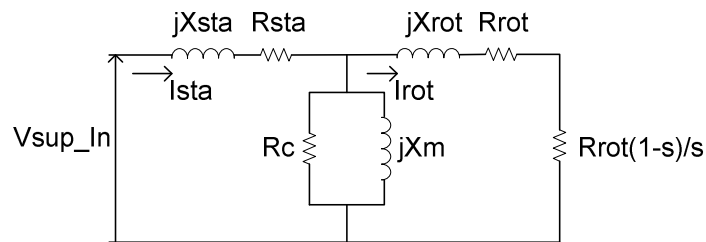


Figure C.1 Equivalent circuit of the induction machine.

The parameters of the above EC calculated from the No-load test and the Blocked rotor test are

$$X_{sta} = j7.425 \Omega; R_{sta} = 6.65 \Omega; X_{rot} = j7.425 \Omega; R_{rot} = 7.64 \Omega; X_m = j171.54 \Omega$$

and  $R_c = 25.88 \Omega$

The above values of the EC parameters shall be used as the input parameters of the SEIG Simulink model.

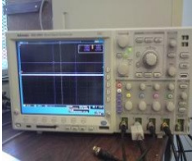
**APPENDIX D****TEST EQUIPMENT**

The following equipment was used in the experimental investigation

Table D.1 Experimental equipment.

Item	Description	Purpose	Photo
Three-phase AC sources	ET system variable voltage, variable frequency three-phase AC power supply, $3 \times 2000 \text{ VA}$ , $3 \times 0 \sim 270 \text{ V}$ , $3 \times 15 \text{ A}$ Type: EAC/3P2000/cc/ATI-10/LT Serial No.: 07.13.2389.	Used when calculating the equivalent circuit parameters to carry out the locked rotor and no-load tests and also for the machine magnetic characteristics tests.	
Capacitor bank	Three-phase self-excitation capacitor bank assembled in-house into a metal enclosure ( $440 \text{ V}$ , $15 \mu\text{F}$ capacitors, 10% tolerance).	Connected to the stator terminals of the induction generator to supply the reactive power of the system.	
Current probe	HP 1146 A AC/DC current probe.	Measure and record the generator, load and capacitor currents.	

DC Drive	1.5 kW Mentor II Digital DC Drive manufactured by Control Techniques.	Control and rotate the prime mover (DC motor).	
DC Motor	3 kW Mawdsley's DC motor, maximum RPM 4000, armature: 240 V, 15 A, fields: 240 V, 0.6/0.16 A.	To act as the prime mover of the induction generator.	
Induction Machine	ABB 1.1 kW, (380~420)/(220~240) V, 2.5/4.4 A, 50 Hz and 2-pole induction machine Model No.: M2VA80B-2 Serial No.: 3GVA081002-ASB.	The machine operates as a generator during these tests. The generator's current waveforms are recorded for further analysis and investigation.	
Three-phase auto-transformer	Three-phase auto-transformer used as a variable inductive load, maximum winding current: 20 A, maximum winding voltage: 270 V.	To provide the generator with a three-phase variable inductive load.	
Multi-meter	Fluke 87 V.	Measurement of rms currents and voltages.	

Oscilloscope	Tektronix MSO 4034 mixed signal oscilloscope, 350 MHz, 2.5 Gs/s, voltage 110~240 V, frequency 50~60 Hz, maximum P power 250 W Serial No. – MSO4034 C000029.	To capture data and export to an external device for further processing.	
Photo sensor tachometer	CEN-TECH Photo sensor tachometer, taking RPM measurements detected by light beam.	Measurement of the rotor shaft speed.	
Variable resistive load	Three Curtis variable resistors, 5 A, 300 V, 2 × 60 Ω.	To provide the generator with a three-phase variable resistive load.	
Voltage probe	SI-9000 differential probe.	Measurement and recording of the generator terminal voltages.	
Wattmeter	Weston Wattmeter, Model S.67, maximum current: 5 A, maximum voltage: 300 V.	Active power and reactive power measurements for the no-load and locked rotor tests carried out to determine the machine equivalent circuit parameters.	

**APPENDIX E****MORE SAMPLED STATE VARIABLES AND JACOBIAN MATRICES**Table E.1 Sampled state variables when  $i_{sD} = 0$  under period-one orbit.

	Sampled Currents when $i_{sD} = 0$		
No.	$i_{sQ}$ (A)	$i_{rd}$ (A)	$i_{rq}$ (A)
1 (fixed point)	-7.9611	3.6808	3.1752
2	-8.1589	3.728	3.3504
3	-7.9206	3.6547	3.0984
4	-7.8688	3.7182	3.124
5	-8.0576	3.6797	3.2406
6	-7.9323	3.6556	3.1225
7	-7.9322	3.7134	3.1815
8	-8.0115	3.6753	3.2064
9	-7.927	3.6649	3.1307
10	-7.9591	3.7011	3.1925
11	-7.9915	3.6741	3.1915
12	-7.9329	3.6744	3.146
13	-7.9666	3.6928	3.1908
14	-7.9778	3.6741	3.1808
15	-7.9421	3.6794	3.1587
16	-7.9685	3.6877	3.1877
17	-7.9683	3.6753	3.1748
18	-7.9494	3.6816	3.1666
19	-7.9682	3.6844	3.1843
20	-7.9631	3.6769	3.1726
21	-7.9547	3.6824	3.1713
22	-7.9668	3.6823	3.1813
23	-7.9607	3.6783	3.1722
24	-7.9583	3.6825	3.174

25	-7.9652	3.6813	3.1789
26	-7.9598	3.6793	3.1726
27	-7.9602	3.6823	3.1754
28	-7.964	3.6809	3.1773
29	-7.9597	3.6799	3.1733
30	-7.961	3.6818	3.1758

Table E.2 The Jacobian matrix, eigenvalue and magnitude of the complex conjugates derived from the sampled state variables under period-one orbit condition.

	Jacobian Matrix	Eigenvalue	Magnitude of the complex conjugates
A <sub>1</sub>	-0.2045 -2.9971 0.4729	0.9992	0.7816
	-0.6961 0.3722 -1.0185	-0.5902 + j0.5124	
	0.2770 1.7509 -0.3490	-0.5902 - j0.5124	
A <sub>2</sub>	-0.3195 -2.5923 -0.2986	0.9993	0.8722
	-0.7269 0.4806 -1.2250	-0.3990 + j0.7756	
	0.3350 1.5467 0.0403	-0.3990 - j0.7756	
A <sub>3</sub>	0.2384 -2.2622 0.7138	0.9994	0.9099
	-0.8798 0.3901 -1.5024	-0.6842 + j0.5998	
	-0.2369 1.2083 -0.9975	-0.6842 - j0.5998	
A <sub>4</sub>	0.3086 -2.1547 0.7663	0.9997	0.8233
	-0.6682 0.7139 -1.3440	-0.4480 + j0.6907	
	-0.1319 1.3690 -0.9189	-0.4480 - j0.6907	
A <sub>5</sub>	0.3001 -2.2686 0.8779	0.9999	0.91
	-0.6652 0.7537 -1.3830	-0.5121 + j0.7522	
	-0.1197 1.5314 -1.0781	-0.5121 - j0.7522	
A <sub>6</sub>	0.4175 -2.2988 1.2059	0.9999	0.831
	-0.6294 0.7445 -1.2831	-0.5280 + j0.6417	
	-0.1699 1.5443 -1.2181	-0.5280 - j0.6417	
A <sub>7</sub>	0.2798 -2.4875 1.0781	0.9999	0.8744
	-0.5608 0.8386 -1.2194	-0.4697 + j0.7375	

	0.0028	1.7809	-1.0579	-0.4697 - j0.7375	
A <sub>8</sub>	0.2670	-2.5314	1.0973	0.9999	0.8629
	-0.5895	0.7398	-1.1764	-0.5157 + j0.6919	
	-0.0102	1.7359	-1.0383	-0.5157 - j0.6919	
A <sub>9</sub>	0.2565	-2.5172	1.0544	1.0000	0.8386
	-0.5831	0.7312	-1.1506	-0.4874 + j0.6824	
	0.0085	1.7107	-0.9624	-0.4874 - j0.6824	
A <sub>10</sub>	0.1768	-2.6009	0.9512	1.0000	0.8766
	-0.5891	0.7250	-1.1583	-0.5018 + j0.7188	
	0.0526	1.7570	-0.9053	-0.5018 - j0.7188	
A <sub>11</sub>	0.2041	-2.5370	0.9455	1.0000	0.843
	-0.6019	0.6950	-1.1556	-0.4986 + j0.6798	
	0.0092	1.6556	-0.8963	-0.4986 - j0.6798	
A <sub>12</sub>	0.2004	-2.5181	0.9144	1.0000	0.8599
	-0.6051	0.7113	-1.1824	-0.4944 + j0.7035	
	0.0087	1.6582	-0.9005	-0.4944 - j0.7035	
A <sub>13</sub>	0.1962	-2.5208	0.9070	1.0000	0.8635
	-0.6047	0.7115	-1.1817	-0.5057 + j0.6999	
	-0.0019	1.6514	-0.9192	-0.5057 - j0.6999	
A <sub>14</sub>	0.2216	-2.4744	0.9168	1.0000	0.8511
	-0.6047	0.7115	-1.1817	-0.4960 + j0.6916	
	-0.0172	1.6234	-0.9251	-0.4960 - j0.6916	
A <sub>15</sub>	0.2222	-2.4669	0.9096	1.0000	0.8626
	-0.6044	0.7151	-1.1851	-0.5004 + j0.7026	
	-0.0161	1.6369	-0.9381	-0.5004 - j0.7026	
A <sub>16</sub>	0.2258	-2.4665	0.9182	1.0000	0.8554
	-0.5997	0.7156	-1.1739	-0.4975 + j0.6959	
	-0.0154	1.6370	-0.9363	-0.4975 - j0.6959	
A <sub>17</sub>	0.2586	-2.4192	0.9455	1.0000	0.8559
	-0.6120	0.6978	-1.1842	-0.4927 + j0.6999	
	-0.0219	1.6276	-0.9418	-0.4927 - j0.6999	
A <sub>18</sub>	0.2665	-2.3875	0.9287	1.0000	0.8668
	-0.6222	0.6572	-1.1626	-0.5093 + j0.7014	

	-0.0217	1.6286	-0.9423	-0.5093 - j0.7014	
A <sub>19</sub>	0.2572	-2.3807	0.8974	1.0000	0.8554
	-0.6146	0.6517	-1.1371	-0.4993 + j0.6946	
	-0.0113	1.6210	-0.9075	-0.4993 - j0.6946	
A <sub>20</sub>	0.3128	-2.3191	0.9653	1.0000	0.8541
	-0.6366	0.6273	-1.1640	-0.4898 + j0.6997	
	-0.0214	1.6099	-0.9198	-0.4898 - j0.6997	
A <sub>21</sub>	0.3414	-2.2461	0.9524	1.0000	0.8552
	-0.6538	0.5834	-1.1562	-0.4947 + j0.6976	
	-0.0339	1.5778	-0.9141	-0.4947 - j0.6976	
A <sub>22</sub>	0.3555	-2.2922	1.0412	1.0000	0.8537
	-0.6590	0.6004	-1.1891	-0.4973 + j0.6939	
	-0.0397	1.5968	-0.9506	-0.4973 - j0.6939	
A <sub>23</sub>	0.4106	-2.2491	1.1294	1.0000	0.8705
	-0.7019	0.5668	-1.2578	-0.5147 + j0.7020	
	-0.0748	1.5693	-1.0068	-0.5147 - j0.7020	
A <sub>24</sub>	0.4023	-2.2654	1.1275	1.0000	0.8516
	-0.6790	0.6117	-1.2524	-0.4967 + j0.6918	
	-0.0779	1.5633	-1.0075	-0.4967 - j0.6918	
A <sub>25</sub>	0.3969	-2.4097	1.2814	1.0000	0.8518
	-0.6754	0.7082	-1.3553	-0.4800 + j0.7037	
	-0.0759	1.6174	-1.0652	-0.4800 - j0.7037	
A <sub>26</sub>	0.4581	-2.3934	1.4158	1.0000	0.849
	-0.6946	0.7031	-1.3975	-0.4942 + j0.6903	
	-0.1143	1.6072	-1.1497	-0.4942 - j0.6903	

Table E.3 Sampled state variables when  $i_{sD} = 0$  under quasi-periodic orbit.

No.	Sampled Currents when $i_{sD} = 0$		
	$i_{sQ}$ (A)	$i_{rd}$ (A)	$i_{rq}$ (A)
1	14.628	0.0897	17.514
2	16.269	3.3017	12.985
3	23.939	4.1968	22.695
4	12.774	2.4027	14.935
5	22.416	0.9226	16.071
6	19.141	2.7468	20.822
7	13.375	3.6334	-13.41
8	27.486	3.2308	21.173
9	15.314	0.3444	18.226
10	16.027	3.4148	13.319
11	25.294	4.1969	23.337
12	13.495	2.005	15.843
13	21.526	1.4724	15.835
14	20.463	3.0531	21.665
15	13.572	3.4476	14.008
16	27.375	2.5293	20.705
17	16.171	0.7905	18.938
18	15.697	3.5053	13.496
19	26.152	-4.169	23.512
20	13.885	1.6245	16.399
21	20.562	1.9169	15.445
22	21.434	3.3113	22.173
23	13.568	3.2589	14.375
24	26.833	1.8177	20.007
25	16.806	1.2005	19.412
26	15.283	3.569	13.546
27	26.727	-4.109	23.416
28	14.141	1.257	16.789
29	19.609	2.2791	15.009

Table E.4 The Jacobian matrix, eigenvalue and magnitude of the complex conjugates derived from the sampled state variables under quasi-periodic orbit condition.

	Jacobian Matrix	Eigenvalue	Magnitude of the complex conjugates
A <sub>1</sub>	0.6162 2.6382 -0.4008 -0.8788 -0.5806 -0.9255 -1.2715 -1.9077 -0.3303	-0.6511 + j0.7495 -0.6511 - j0.7495 1.0074	0.9928
A <sub>2</sub>	0.1979 2.8269 -0.8769 -0.8263 -0.6043 -0.8658 -1.2378 -1.9229 -0.2920	-0.8532 + j0.7596 -0.8532 - j0.7596 1.008	1.1423
A <sub>3</sub>	-0.0609 2.6776 -1.1222 -0.5125 -0.4232 -0.5682 -0.7183 -1.6232 0.2006	-0.6387 + j0.6589 -0.6387 - j0.6589 0.9939	0.9177
A <sub>4</sub>	-0.0125 2.9295 -1.0403 -0.5272 -0.5002 -0.5932 -0.7201 -1.6329 0.1974	-0.6579 + j0.7845 -0.6579 - j0.7845 1.0005	1.0239
A <sub>5</sub>	-0.2568 3.5431 -1.3458 -0.3422 -0.9648 -0.3618 -0.4837 -2.2268 0.4932	-0.8668 + j0.6264 -0.8668 - j0.6264 1.0051	1.0694
A <sub>6</sub>	0.4000 3.4157 -0.7253 -0.5539 -0.9238 -0.5618 -0.6914 -2.1865 0.2968	-0.6148 + j0.7015 -0.6148 - j0.7015 1.0027	0.9328
A <sub>7</sub>	0.7235 3.6455 -0.3404 -0.7563 -1.0675 -0.8027 -0.9827 -2.3933 -0.0497	-0.6951 + j0.8054 -0.6951 - j0.8054 0.9965	1.0688
A <sub>8</sub>	0.5348 2.9990 -0.4867 -0.7058 -0.8944 -0.7635 -0.9871 -2.4084 -0.0531	-0.7128 + j0.5236 -0.7128 - j0.5236 1.0128	0.8844
A <sub>9</sub>	0.6473 2.8506 -0.3893 -0.8669 -0.6819 -0.9028 -1.1960 -2.1329 -0.2338	-0.6404 + j0.7300 -0.6404 - j0.7300 1.0123	0.9711
A <sub>10</sub>	0.4661 2.9002 -0.5946	-0.8204 + j0.7709	1.1258

	-0.9137	-0.6691	-0.9559	-0.8204 - j0.7709	
	-1.3711	-2.0849	-0.4323	1.0055	
A <sub>11</sub>	0.0395	2.5771	-0.9989	-0.6516 + j0.6452	0.917
	-0.5910	-0.4247	-0.6501	-0.6516 - j0.6452	
	-0.8375	-1.6807	0.0734	0.9914	
A <sub>12</sub>	0.0513	2.7554	-0.9663	-0.6575 + j0.7746	1.016
	-0.5929	-0.4530	-0.6553	-0.6575 - j0.7746	
	-0.8327	-1.6081	0.0867	1	
A <sub>13</sub>	-0.3415	3.4521	-1.4354	-0.8862 + j0.6634	1.107
	-0.3665	-0.8546	-0.3848	-0.8862 - j0.6634	
	-0.5475	-2.1139	0.4274	1.0038	
A <sub>14</sub>	0.2396	3.4156	-0.8815	-0.6164 + j0.6974	0.9308
	-0.4804	-0.8474	-0.4935	-0.6164 - j0.6974	
	-0.6051	-2.1103	0.3725	0.9975	
A <sub>15</sub>	0.5327	3.6967	-0.5283	-0.6858 + j0.8044	1.0571
	-0.6504	-1.0105	-0.6982	-0.6858 - j0.8044	
	-0.8311	-2.3271	0.1001	0.9939	
A <sub>16</sub>	0.4502	3.2165	-0.5787	-0.7296 + j0.5274	0.9003
	-0.6447	-0.9774	-0.6948	-0.7296 - j0.5274	
	-0.8655	-2.5273	0.0791	1.0111	
A <sub>17</sub>	0.6551	3.0064	-0.3950	-0.6382 + j0.7234	0.9647
	-0.8508	-0.7660	-0.8796	-0.6382 - j0.7234	
	-1.1267	-2.2594	-0.1551	1.0104	
A <sub>18</sub>	0.6336	3.0089	-0.4193	-0.7920 + j0.7790	1.1109
	-0.9635	-0.7529	-1.0072	-0.7920 - j0.7790	
	-1.3982	-2.2278	-0.4627	1.002	
A <sub>19</sub>	0.1451	2.5394	-0.8795	-0.6634 + j0.6281	0.9136
	-0.6598	-0.4611	-0.7212	-0.6634 - j0.6281	
	-0.9272	-1.7751	-0.0191	0.9917	
A <sub>20</sub>	0.1393	2.6516	-0.8733	-0.6567 + j0.7656	1.0087
	-0.6609	-0.4403	-0.7201	-0.6567 - j0.7656	
	-0.9345	-1.6330	-0.0112	1.0011	
A <sub>21</sub>	-0.3582	3.3149	-1.4532	-0.8955 + j0.6913	1.1313

	-0.4264	-0.7530	-0.4467	-0.8955 - j0.6913	
	-0.6470	-2.0164	0.3240	1.0037	
$A_{22}$	0.0871	3.3419	-1.0268	-0.6196 + j0.6930	0.9296
	-0.4350	-0.7535	-0.4550	-0.6196 - j0.6930	
	-0.5457	-2.0102	0.4210	0.9938	
$A_{23}$	0.3336	3.6503	-0.7242	-0.6794 + j0.8019	1.051
	-0.5691	-0.9213	-0.6196	-0.6794 - j0.8019	
	-0.7081	-2.2134	0.2216	0.9927	
$A_{24}$	0.3176	3.3887	-0.7219	-0.7499 + j0.5399	0.924
	-0.5760	-1.0329	-0.6186	-0.7499 - j0.5399	
	-0.7304	-2.5793	0.2249	1.0094	
$A_{25}$	0.6283	3.1380	-0.4374	-0.6350 + j0.7176	0.9582
	-0.8177	-0.8379	-0.8399	-0.6350 - j0.7176	
	-1.0324	-2.3357	-0.0516	1.0089	
$A_{26}$	0.7435	3.1415	-0.3065	-0.7677 + j0.7853	1.0982
	-0.9797	-0.8427	-1.0240	-0.7677 - j0.7853	
	-1.3716	-2.3458	-0.4370	0.9993	

## REFERENCES

- [1] E. Muljadi, J. Sallan, M. Sanz and C. P. Butterfield, "Investigation of Self-excited Induction Generators for Wind Turbine Applications," in *Thirty-Fourth Industry Applications Conference Annual Meeting*, Phoenix, October 1999.
- [2] P. K. Sen and J. P. Nelson, "Application Guidelines for Induction Generators," in *IEEE International Conference on Electric Machines and Drives*, Milwaukee, May 1997.
- [3] B. Palle, M. G. Simoes and F. A. Farret, "Dynamic Simulation and Analysis of Parallel Self-excited Induction Generators for Islanded Wind Farm Systems," *IEEE Transactions on Industry Applications*, vol. 41, no. 4, pp. 1099 - 1106 , July 2005.
- [4] R. C. Bansal, T. S. Bhatti and D. P. Kothari, "Bibliography on the Application of Induction Generators in Nonconventional Energy Systems," *IEEE Transactions on Energy Conversions*, vol. 18, no. 3, pp. 433-439, September 2003.
- [5] E. D. Basset and F. M. Potter, "Capacitive Excitation for Induction Generators," *Transactions of the American Institute of Electrical Engineers*, vol. 54, no. 5, pp. 540-545, May 1935.
- [6] P. K. Shadhu Khan and J. K. Chatterjee, "Three-Phase Induction Generators: A Discussion on Performance," *Taylor & Francis on Electric Machines and Power Systems*, vol. 27, no. 8, pp. 813-832, 1999.
- [7] J. M. Elder, J. T. Boys and J. L. Woodward, "Self-excited Induction Machine as a Small Low-cost Generator," *IEE Proceedings C on Generation, Transmission and Distribution*, vol. 131, no. 2, pp. 33-41, March 1984.
- [8] H. S. Timorabadi , "Voltage Source Inverter for Voltage and Frequency Control of a Stand-alone Self-excited Induction Generator," in *Canadian Conference on Electrical and Computer Engineering*, Ottawa, May 2006.
- [9] R. Bonert and S. Rajakaruna, "Self-excited Induction Generator with Excellent Voltage and Frequency Control," *IEE Proceedings on Generation, Transmission and Distribution*, vol. 145, no. 1, pp. 33-39, January 1998.

- [10] Y. Uctug and M. Demirekler, "Modelling, Analysis and Control of a Wind-turbine Driven Self-excited Induction Generator," *IEE Proceedings C on Generation, Transmission and Distribution*, vol. 135, no. 4, pp. 268-275, June 1988.
- [11] K.-E. Hallenius, P. Vas and J. E. Brown, "The Analysis of a Saturated Self-excited Asynchronous Generator," *IEEE Transactions on Energy Conversion*, vol. 6, no. 2, pp. 336-345, June 1991.
- [12] M. G. Simoes and F. A. Farret, *Renewable Energy Systems: Design and Analysis with Induction Generators*, London: CRC Press, May 2004.
- [13] R. Wamkeue, D. Aguglia, M. Lakehal and P. Viarouge, "Two-step Method for Identification of Nonlinear Model of Induction Machine," *IEEE Transactions on Energy Conversion*, vol. 22, no. 4, pp. 801 - 809, December 2007.
- [14] P. Vas, *Electrical Machines and Drives - A Space-vector Theory Approach*, Oxford: Clarendon Press, 1992.
- [15] Committee, House of Lords - European Union, "The EU's Target for Renewable Energy: 20% by 2020," TSO (The Stationery Office), London, October 2008.
- [16] M. G. Simões and F. A. Farret, *Alternative Energy Systems: Design and Analysis with Induction Generators*, Bosa Roca: Taylor & Francis, December 2007.
- [17] A. F. Zobaa and R. Bansal, *Handbook of Renewable Energy Technology*, Singapore: World Scientific Publishing, 2011.
- [18] R. C. Bansal, "Three-Phase Self-Excited Induction Generators: An Overview," *IEEE Transactions on Energy Conversion*, vol. 20, no. 2, pp. 292-299, June 2005.
- [19] G. K. Singh, "Self-excited Induction Generator Research - a Survey," *Electric Power Systems Research*, vol. 69, no. 2-3, pp. 107-114, May 2004.
- [20] M. S. El-Moursi, "Fault Ride Through Capability Enhancement for Self-excited Induction Generator-based Wind Parks by Installing Fault Current Limiters," *IET on Renewable Power Generation*, vol. 5, no. 4, pp. 269 - 280, July 2011.
- [21] S. S. Murthy, G. Bhuvanewari, S. Gao and R. K. Ahuja, "Self Excited Induction Generator for Renewable Energy Applications to Supply Single-phase Loads in Remote Locations," in *IEEE International Conference on*

- [22] S. S. Murthy, O. P. Malik and A. K. Tandon, "Analysis of Self-excited Induction Generators," *IEE Proceedings C on Generation, Transmission and Distribution*, vol. 129, no. 6, pp. 260-265, November 1982.
- [23] L. Quazene and G. McPherson, "Analysis of the Isolated Induction Generator," *IEEE Transactions on Power Apparatus and Systems*, Vols. PAS-102, no. 8, pp. 2793-2798, August 1983.
- [24] A. K. Tandon, S. S. Murthy and G. J. Berg, "Steady State Analysis of Capacitor Self-excited Induction Generators," *IEEE Transactions on Power Application Systems*, Vols. PAS-103, no. 3, pp. 612-618, March 1984.
- [25] S. Rajakaruna and R. Bonert, "A Technique for the Steady-state Analysis of a Self-excited Induction Generator with Variable Speed," *IEEE Transactions on Energy Conversion*, vol. 8, no. 4, pp. 757-761, December 1993.
- [26] T. F. Chan, "Analysis of Self-excited Induction Generators Using an Iterative Method," *IEEE Transactions on Energy Conversion*, vol. 10, no. 3, pp. 502-507, September 1995.
- [27] S. C. Agarwal and M. Singh, "An Analysis of Self-excited Pole Changing Induction Generators," in *Proceedings 8th National Power System Conference*, Delhi, India, December 14-17, 1994.
- [28] J. K. Chatterjee and P. K. S. Khan, "Excitation Capacitor Requirement and Performance of Pole Changing Self-excited Induction Generator Operating with Unregulated Prime Mover," in *Proceedings 9th National Power System Conference*, Kanpur, India, December 19-21, 1996.
- [29] L. Wang and C. H. Lee, "A Novel Analysis of the Performance of an Isolated Self-excited Induction Generator," *IEEE Transactions on Energy Conversion*, vol. 12, no. 2, pp. 109-115, June 1997.
- [30] T. F. Chan, "Self-excited Induction Generators Driven by Regulated and Unregulated Turbines," *IEEE Transactions on Energy Conversion*, vol. 11, no. 2, pp. 338-343, June 1996.
- [31] S. M. Alghuwainem, "Steady State Analysis of an Isolated Self-excited Induction Generator Driven by Regulated and Unregulated Turbine," *IEEE Transactions on Energy Conversion*, vol. 14, no. 3, pp. 718-723, September 1999.

- [32] S. M. Alghuwainem, "Steady State Analysis of a Self-excited Induction Generator Including Transformer Saturation," *IEEE Transactions on Energy Conversion*, vol. 14, no. 3, pp. 667-672, September 1999.
- [33] T. F. Chan and L. L. Lai, "Steady State Analysis and Performance of a Stand-alone Three-phase Induction Generator with Asymmetrically Connected Load Impedances and Excitation Capacitances," *IEEE Transactions on Energy Conversion*, vol. 16, no. 4, pp. 327-333, December 2001.
- [34] L. Shridhar, B. Singh and C. S. Jha, "Transient Performance of the Self Regulated Short-shunt Self-excited Induction Generator," *IEEE Transactions on Energy Conversion*, vol. 10, no. 2, pp. 261-267, June 1995.
- [35] L. Wang and J. Y. Su, "Dynamic Performances of an Isolated Self-excited Induction Generator under Various Loading Conditions," *IEEE Transactions on Energy Conversion*, vol. 14, no. 1, pp. 93-100, March 1999.
- [36] D. Seyoum, C. Grantham and M. F. Rahman, "The Dynamic Characteristics of an Isolated Self-excited Induction Generator Driven by a Wind Turbine," *IEEE Transactions on Industry Applications*, vol. 39, no. 4, pp. 936-944, July 2003.
- [37] I. R. Smith and S. Sriharan, "Transients in Induction Machines with Terminal Capacitors," *Proceedings of the Institution of Electrical Engineers*, vol. 115, no. 4, pp. 519 - 527 , April 1968.
- [38] L. Wang and R. Y. Deng, "Transient Performance of an Isolated Induction Generator under Unbalanced Excitation Capacitors," *IEEE Transactions on Energy Conversion*, vol. 14, no. 4, pp. 887-893, December 1999.
- [39] L. Wang and C. H. Lee, "Long Shunt and Short Shunt Connections on a Dynamic Performance of a SEIG Feeding an Induction Motor Load," *IEEE Transactions on Energy Conversion*, vol. 15, no. 1, pp. 1-7, March 2000.
- [40] D. Levy, "Stand Alone Induction Generators," *Electric Power Systems Research*, vol. 41, no. 3, pp. 191-201, June 1997.
- [41] S. K. Jain, J. D. Sharma and S. P. Singh, "Transient Performance of Three-phase Self-excited Induction Generator during Balanced and Unbalanced Faults," *IEE Proceedings on Generation, Transmission and Distribution*, vol. 149, no. 1, pp. 50-57, January 2002.
- [42] F. A. Farret, B. Palle and M. G. Simoes, "Full Expandable Model of Parallel

Self-excited Induction Generators," *IEE Proceedings on Power Applications*, vol. 152, no. 1, pp. 96-102, January 2005.

- [43] N. B. Tufillaro, T. Abbott and J. Reilly, *An Experimental Approach to Nonlinear Dynamics and Chaos*, the University of Michigan: Addison-Wesley, March 1992.
- [44] C. F. Wagner, "Self-excitation of Induction Motors," *Transactions of the American Institute of Electrical Engineers*, vol. 58, no. 2, pp. 47-51, February 1939.
- [45] D. W. Novotny, D. J. Gritter and G. H. Studtmann, "Self-excitation in Inverter Driven Induction Machines," *IEEE Transactions on Power Apparatus and Systems*, vol. 96, no. 4, pp. 1117 - 1125 , July 1977.
- [46] E. Levy and Y. W. Liao, "An Experimental Investigation of Self-excitation in Capacitor Excited Induction Generators," *Electric Power System Research*, vol. 53, no. 1, pp. 59-65, January 2000.
- [47] M. B. Brennen and A. Abbondanti, "Static Exciters for Induction Generators," *IEEE Transactions on Industry Applications*, Vols. IA-13, no. 5, pp. 422-428, September 1977.
- [48] J. Arrillaga and D. B. Watson, "Static Power Conversion from Self-excited Induction Generator," *Proceedings of the Institution of Electrical Engineers*, vol. 125, no. 8, pp. 743-746, August 1978.
- [49] E. Suarez and G. Bortolotto, "Voltage-frequency Control of a Self-excited Induction Generator," *IEEE Transactions on Energy Conversion*, vol. 14, no. 3, pp. 394-401, September 1999.
- [50] O. Chtchetinine, "Voltage Stabilization System for Induction Generator in Stand Alone Mode," *IEEE Transactions on Energy Conversion*, vol. 14, no. 4, pp. 298-303, December 1999.
- [51] N. H. Malik and A. H. Al-Bahrani, "Influence of the Terminal Capacitor on the Performance Characteristics of a Self Excited Induction Generator," *IEE Proceedings C on Generation, Transmission and Distribution*, vol. 137, no. 2, pp. 168-173, March 1990.
- [52] B. Singh, S. S. Murthy, Madhusudan, M. Goel and A. K. Tandon, "A Steady State Analysis on Voltage and Frequency Control of Self-Excited Induction Generator in Micro-hydro System," in *International Conference on Power Electronics, Drives and Energy Systems*, New Delhi, December 2006.

- [53] K. H. Youssef, M. A. Wahba, H. A. Yousef and O. A. Sebakhy, "A New Method for Voltage and Frequency Control of Stand-alone Self-excited Induction Generator Using PWM Converter with Variable DC Link Voltage," in *American Control Conference*, Seattle, June 2008.
- [54] P. Vas, K. E. Hallenius and J. E. Brown, "Cross-saturation in Smooth-air-gap Electrical Machines," *IEEE Transactions on Energy Conversion*, Vols. EC-1, no. 1, pp. 103-112, March 1986.
- [55] J. E. Brown, K. P. Kovacs and P. Vas, "A Method of Including the Effects of Main Flux Path Saturation in the Generalised Equations of A.C. Machines," *IEEE Transactions on Power Apparatus and Systems*, Vols. PAS-102, no. 1, pp. 96-103, January 1983.
- [56] A. F. Almarshoud, M. A. Abdel-halim and A. I. Alolah, "Including Effects of Cross-saturation and Leakage Path Saturation together in the Generalized Model of Three Phase Induction Machine," in *Canadian Conference on Electrical and Computer Engineering*, Toronto, May 2001.
- [57] E. Levi, "Impact of Cross-saturation on Accuracy of Saturated Induction Machine Models," *IEEE Transactions on Energy Conversion*, vol. 12, no. 3, pp. 211-216, September 1997.
- [58] T. A. Lipo and A. Consoli, "Modeling and Simulation of Induction Motors with Saturable Leakage Reactances," *IEEE Transactions on Industry Applications*, Vols. IA-20, no. 1, pp. 180-189, January 1984.
- [59] R. Lin and A. Arkkio, "Calculation and Analysis of Stator End-winding Leakage Inductance of an Induction Machine," *IEEE Transactions on Magnetics*, vol. 45, no. 4, pp. 2009-2014, April 2009.
- [60] M. S. N. Said and M. E. H. Benbouzid, "H-G Diagram Based Rotor Parameters Identification for Induction Motors Thermal Monitoring," *IEEE Transactions on Energy Conversion*, vol. 15, no. 1, pp. 14-18, March 2000.
- [61] M. E. H. Benbouzid, M. Zerikat and M. S. N. Said, "A Practical Approach to Modelling Induction Machine Saturation," *European Transactions on Electrical Power*, vol. 14, no. 2, pp. 119-130, March 2004.
- [62] N. Nait-Said, F. Z. Louai and M. S. Nait-Said, "Induction Machine Parameters Identification Using Modified H-G Diagram," in *10th IEEE International Conference on Electronics, Circuits and Systems*, Sharjah, December 2003.
- [63] K. Hafiz, G. Nanda and N. C. Kar, "Skin Effect Modeling of Self Excited

Induction Generator in Wind Power Application,” in *Canadian Conference on Electrical and Computer Engineering*, Niagara Falls, May 2008.

- [64] K. Hafiz, G. Nanda and N. C. Kar, “Comparative Performance Analysis of Aluminum-rotor and Copper-rotor SEIG Considering Skin Effect,” in *18th International Conference on Electrical Machines*, Vilamoura, September 2008.
- [65] O. I. Okoro, “Transient State Modelling of Asynchronous Generator with Skin-effect,” *The Pacific Journal of Science and Technology*, vol. 5, no. 2, pp. 63-71, October 2004.
- [66] Y. A. Kuznetsov, *Elements of Applied Bifurcation Theory*, New York: Springer-Verlag, 2004.
- [67] S. Banerjee and G. C. Verghese, *Nonlinear Phenomena in Power Electronics*, New York: IEEE Press, July 2001.
- [68] W. M. Haddad and V. Chellaboina, *Nonlinear Dynamical Systems and Control: A Lyapunov-based Approach*, Princeton, USA: Princeton University Press, 2008.
- [69] T. S. Parker and L. O. Chua, *Practical Numerical Algorithms for Chaotic Systems*, New York: Springer-Verlag, 1989.
- [70] S. H. Strogatz, *Nonlinear Dynamics and Chaos - with Applications to Physics, Biology, Chemistry, and Engineering*, Cambridge: Westview Press, January 2001.
- [71] J. M. T. Thompson and H. B. Stewart, *Nonlinear Dynamics and Chaos*, West Sussex, England: John Wiley & Sons, 2002.
- [72] S.-C. Kuo and L. Wang, “Steady-state Performance and Dynamic Stability of a Self-excited Induction Generator Feeding an Induction Motor,” in *IEEE Power Engineering Society Winter Meeting*, Singapore, January 2000.
- [73] M. H. Haque, “A Novel Method of Evaluating Performance Characteristics of a Self-excited Induction Generator,” *IEEE Transactions on Energy Conversion*, vol. 24, no. 2, pp. 358-365, June 2009.
- [74] I. Boldea and S. A. Nasar, *The Induction Machine Handbook*, Florida: CRC Press, 2002.
- [75] N. K. Sinha, *Control Systems*, New Delhi, India: New Age International, 2008.

- [76] A. Veltman, D. W. G. Pulle and R. W. D. Doncker, *Fundamentals of Electrical Drives*, Edindoven, Netherlands: Springer, 2007.
- [77] Z. Emin, B. A. T. Al Zahawi, D. W. Auckland and Y. K. Tong, "Ferroresonance in Electromagnetic Voltage Transformers: a Study Based on Nonlinear Dynamics," *IEE Proceedings on Generation, Transmission and Distribution*, vol. 144, no. 4, pp. 383-387, July 1997.
- [78] F. Khorrami, P. Krishnamurthy and H. Melkote, *Modelling and Adaptive Nonlinear Control of Electrical Motors*, Berlin: Springer-Verlag, 2003.